

WL-TR-96-2117



## NONEQUILIBRIUM PLASMAS

DEVELOPMENT AND APPLICATION OF BULK AND NEAR SURFACE LASER DIAGNOSTICS FOR PLASMA PROCESSING

A. TSEREPI, B.L. PREPPERNAU, and T. A. MILLER

DEPARTMENT OF CHEMISTRY  
OHIO STATE UNIVERSITY  
COLUMBUS OHIO 43210

OCTOBER 1996

FINAL THE FOR PERIOD JUNE 1992 -- JUNE 196

Approved for public release; distribution unlimited

19970128 042

DTIC QUALITY INSPECTED 4

AERO PROPULSION AND POWER DIRECTORATE  
WRIGHT LABORATORY  
AIR FORCE MATERIEL COMMAND  
WRIGHT-PATTERSON AIR FORCE BASE, OH 45433-7251

NOTICE

When Government drawings, specifications, or other data are used for any purpose other than in connection with a definitely Government-related procurement, the United States Government incurs no responsibility or any obligation whatsoever. The fact that the government may have formulated or in any way supplied the said drawings, specifications, or other data, is not to be regarded by implication, or otherwise in any manner construed, as licensing the holder, or any other person or corporation; or as conveying any rights or permission to manufacture, use, or sell any patented invention that may in any way be related thereto.

This report is releasable to the National Technical Information Service (NTIS). At NTIS, it will be available to the general public, including foreign nations.

This technical report has been reviewed and is approved for publication.

  
\_\_\_\_\_  
BISWA N. GANGULY  
Power Electronic Sciences Branch  
Aerospace Power Division  
Aero Propulsion and Power Directorate

  
\_\_\_\_\_  
CHARLES W. ANDERSON

Chief, Semiconductor Sciences Branch  
Aerospace Power Division  
Aero Propulsion & Power Directorate

  
\_\_\_\_\_  
MICHAEL A. MARCINIAK, Maj, USAF  
Deputy Chief  
Aerospace Power Division  
Aero Propulsion & Power Directorate

If your address has changed, if you wish to be removed from our mailing list, or if the addressee is no longer employed by your organization please notify WL/POOD, WPAFB, OH 45433-7919 to help us maintain a current mailing list.

Copies of this report should not be returned unless return is required by security considerations, contractual obligations, or notice on a specific document.

# REPORT DOCUMENTATION PAGE

Form Approved  
OMB No. 0704-0188

Public reporting burden for this collection of information is estimated to average 1 hour per response, including the time for reviewing instructions, searching existing data sources, gathering and maintaining the data needed, and completing and reviewing the collection of information. Send comments regarding this burden estimate or any other aspect of this collection of information, including suggestions for reducing this burden, to Washington Headquarters Services, Directorate for Information Operations and Reports, 1215 Jefferson Davis Highway, Suite 1204, Arlington, VA 22202-4302, and to the Office of Management and Budget, Paperwork Reduction Project (0704-0188), Washington, DC 20503.

1. AGENCY USE ONLY (Leave blank)	2. REPORT DATE	3. REPORT TYPE AND DATES COVERED	
	Oct 96	Final 6/15/92-6/30/96	
4. TITLE AND SUBTITLE Nonequilibrium Plasmas Development and Application of Bulk and Near-Surface Laser Diagnostics for Plasma Processing			5. FUNDING NUMBERS C-F33615-92-C-2244 PE 61102 PR 2301 TA P1 WU 00
6. AUTHOR(S) A. Tserepi, B. L. Preppernau, and T.A. Miller			
7. PERFORMING ORGANIZATION NAME(S) AND ADDRESS(ES)  Department of Chemistry The Ohio State University Columbus Ohio 43210		8. PERFORMING ORGANIZATION REPORT NUMBER	
9. SPONSORING/MONITORING AGENCY NAME(S) AND ADDRESS(ES)  Aeropropulsion & Power Directorate Wright Laboratory Air Force Materiel Command Wright Patterson AFB, OH 45433-7251 POC: Ganguly, WL/POOD, (937)255-2923		10. SPONSORING/MONITORING AGENCY REPORT NUMBER WL-TR-96-2117	
11. SUPPLEMENTARY NOTES			
12a. DISTRIBUTION/AVAILABILITY STATEMENT  approved for public release; distribution is unlimited		12b. DISTRIBUTION CODE	
13. ABSTRACT (Maximum 200 words)  The two-photon laser induced fluorescence (TALIF) diagnostic has been developed and/or applied to plasma processing systems involving H, O, and N atoms. Based upon TALIF data, models have been developed for the spatial and temporal variation of the absolute atomic concentrations in H <sub>2</sub> , O <sub>2</sub> , and N <sub>2</sub> plasmas. The portability of the TALIF diagnostic has been demonstrated. Limitations of the technique due to stimulated emission and fluorescence quenching have been investigated and procedures developed to minimize their effects.			
14. SUBJECT TERMS Atomic H, N, O, plasma processing, laser diagnostics			15. NUMBER OF PAGES 145
			16. PRICE CODE
17. SECURITY CLASSIFICATION OF REPORT unclass	18. SECURITY CLASSIFICATION OF THIS PAGE unclass	19. SECURITY CLASSIFICATION OF ABSTRACT unclass	20. LIMITATION OF ABSTRACT SAR

## Table of Contents

1.	Introduction .....	1
2.	TALIF as a probe for heterogeneous processes in hydrogen plasmas .....	3
A.	Experiment .....	4
B.	Results and discussion .....	6
1.	Model .....	6
2.	Loaded H <sub>2</sub> discharges .....	21
3.	Modification of the surface loss coefficient by the plasma .....	27
a.	Permanent modification .....	27
b.	Temporary modification .....	30
3.	O atom TALIF diagnostic in plasmas .....	34
A.	Experiment .....	35
B.	Results and Discussion .....	36
1.	Concentration measurements in space and time .....	36
2.	Model .....	40
3.	Early discharge behavior .....	50
4.	Etching plasmas .....	53
C.	Conclusion .....	55
4.	Effect on TALIF diagnostics of stimulated emission in O plasmas .....	57
A.	Experiment .....	58
B.	Results and Discussion .....	59
5.	Angular Momentum State Mixing and Quenching of n=3 Atomic Hydrogen Fluorescence .....	70
A.	Experiment .....	71
B.	Results and Analysis of Excited State Fluorescence Quenching Measurements .....	72
C.	Discussion .....	87
D.	Conclusion .....	90
6.	Application of TALIF Diagnostics to GEC Reference Reactor .....	93
A.	Review of the GEC Reference Cell .....	94
B.	Experiment .....	99
C.	H-Atom Concentration Calibration Procedure .....	101

D.	Results and Discussion .....	103
7.	TALIF Diagnostics of Nitrogen Atoms .....	119
A.	Experiment .....	120
1.	N atom TALIF Schemes .....	120
2.	Absolute Concentration Measurement of Atomic Nitrogen .....	124
3.	RF Plasma Source .....	125
4.	TALIF Laser Source and Detection .....	125
B.	Results and Discussion .....	127
	References .....	131
	Bibliography .....	136

## List of Illustrations

1.	Spatial profiles of H-atom concentration at steady-state discharge conditions with the indicated materials (Al, Si, Ni) loaded on the ground electrode (at 0 mm) .....	7
2.	Temporal profiles of H atoms taken in the discharge afterglow ( $t > 2$ ms) and fits with parameters the loss coefficient $\gamma$ of the surfaces .....	8
3.	Typical H-atom concentration profiles as a function of the distance from the ground electrode (at 0 mm), in a 10-MHz continuous $H_2$ discharge .....	12
4.	Temporal evolution of H-atom spatial profiles after the onset of a pulsed discharge; experimental data points and simulated results at $t = 0.25, 1.0$ , and $2.5$ ms .....	13
5.	Decay of H-atom spatial profiles in the afterglow of a pulsed discharge (turned off at $t_0 = 2$ ms); data points and simulated results at $0.25, 0.5$ , and $1.0$ ms after $t_0$ .....	14
6.	The steady-state concentration gradients for H and D atoms at small distances from the SS electrode surface determine a loss coefficient $\gamma_{ss} = 5\%$ .....	16
7.	Temporal profile of H-concentration in a pulsed discharge (turned off at $t_0 = 2$ ms). A single exponential fits well the H-atom decay in the afterglow ( $t > 2$ ms) .....	17
8.	Simulations of the variation of H-atom concentration over a small distance from a surface characterized by a loss coefficient $\gamma$ varied from $0.1\%$ to $100\%$ .....	19
9.	Simulations of H-atom concentration decay rates in the discharge afterglow as a function of the loss coefficient $\gamma$ of the electrode surface .....	20
10.	Comparison of H-atom radial profiles probed 1 mm above a (a) stainless-steel, (b) GaAs, and (c) gold-coated (10x10 mm) substrate, placed on the ground electrode .....	23
11.	Evolution of H-atom spatial profiles after the onset of a pulsed discharge loaded with a GaAs wafer on the ground electrode; data points at $t = 0.15, 0.50$ , and $2.50$ ms .....	25
12.	(a) Temporal decay of H atoms near an Si surface exposed to a low pressure $H_2/Ar$ discharge for $T = 0, 1.5, 3.0$ , and $16.5$ min. (b) Decay rates of H atoms as a function of exposure time $T$ .....	28

13.	Variation of the decay rate (and the loss coefficient) of H atoms over an Al surface as a function of the discharge pressure .....	32
14.	Calibration curve for O-TALIF intensities. Each data point is determined by titrating <i>in situ</i> an O-TALIF signal with a known concentration of NO <sub>2</sub> (inset) .....	37
15.	Spatial profiles of O-atom concentration in a 3 Torr discharge, after initial discharge turn-on ( $t=0.25$ ms, $t=1.8$ ms). They demonstrate a uniform production of atomic oxygen at a region (in the interelectrode gap) extended from a distance $x_0=1.2$ mm from either electrode surface, and a small loss on the electrode surfaces (SS) with a coefficient $\gamma=0.5\pm0.1$ % .....	39
16.	Temporal profile in a 3 Torr pulsed discharge. The decay of the atomic oxygen ( $t>2$ ms) is much slower than the rise ( $0< t < 2$ ms) as shown by the dotted curve shown in the afterglow obtained with a decay rate equal to that in the rise. The data in the decay are fit to Eq. (11) with $\gamma=0.6\%$ , while even a loss coefficient as high as 100% cannot accommodate the high rate constant for the rise of the O-concentration (dotted line) .....	41
17.	Dependence of temporal profiles on the discharge pressure. (a) The data in a 3 Torr/50 W discharge were fit with $\gamma=0.6\%$ and $R_i/R_0=8$ . (b) The data in a 0.1 Torr/50 W discharge were fit with $\gamma=1.3\%$ and $R_i/R_0=2$ .....	44
18.	Dependence of temporal profiles on the discharge power. (a) The data in a 90 W/0.2 Torr discharge were fit with $\gamma=1.3\%$ and $R_i/R_0=3$ . (b) The data in a 55 W/0.2 Torr discharge were fit with $\gamma=0.75\%$ and $R_i/R_0=2$ .....	45
19.	Variation of the decay rates in a pulsed discharge as a function of the discharge power. The observed increase of the decay rate with power corresponds to an increase of the loss coefficient of O atoms on an SS surface from 0.8 to 4.0 % .....	47
20.	Spatial profiles for O atoms as a function of pressure. Fits to the data indicate a reduction of the loss coefficient of the SS surface from 1.1 % to 0.3 % as pressure increases from 0.25 to 3 Torr .....	48
21.	Decay rates for O-atoms in the afterglow of a pulsed discharge as a function of inverse pressure. The solid curves are the predictions of the diffusion model (discussed in the text) for the variation of the decay rate with pressure, and indicate an increase of the loss coefficient $\gamma$ from 0.3 % to 1.6 % as the pressure decreases from 1 to 0.1 Torr .....	49

22.	Variation of the decay rate of O atoms upon addition of CF <sub>4</sub> in a O <sub>2</sub> discharge. The decay rates were measured in the afterglow of a pulsed CF <sub>4</sub> /O <sub>2</sub> discharge kept at a constant total pressure (0.2 Torr). The solid curve is a guide to the eye.	54
23.	Titration curves for TALIF (open squares) and SE (open triangles) signals at a constant initial O-atom concentration. The laser power was (a) 185 μJ/pulse, (b) 57 μJ/pulse, and (c) 44 μJ/pulse. Every data point is an average of 128 laser pulses.	60
24.	Intensity dependence of the TALIF signal in the flow reactor. The laser power P is measured in μJ/pulse. The solid line is a fit to the low laser power (<60 μJ/pulse) data with a slope of 2.	62
25.	Titration curves taken at different initial O-atom concentrations but otherwise at identical conditions. The TALIF and SE signals are noted with open squares and triangles, respectively. The x-intercepts of the solid lines fitted to the data indicate the end-point of the titration and the threshold of SE, respectively.	63
26.	Titration curve showing a strong deviation of the TALIF signal from linearity due to significant SE. The observed reduction in TALIF due to SE is about 30%, the highest we have observed in our experiments.	66
27.	Pressure dependence of TALIF and SE signals in an RF parallel plate reactor. The raw TALIF data (open squares) have been corrected for the quenching of the laser-excited state by O <sub>2</sub> and a linear fit (solid line) is done to the corrected data (solid triangles). The O concentration at SE threshold is [O] <sub>thr</sub> = 3.6×10 <sup>14</sup> cm <sup>-3</sup> .	67
28.	Measured Versus Calculated Photodissociated Acetylene H-Atom TALIF Signal.	73
29.	Measured versus Calculated H-Atom TALIF Lifetime from Photodissociation of C <sub>2</sub> H <sub>2</sub> . Curved line is predicted from model calculations.	75
30.	Radiative Decay of n=3 Component Levels for 10 Torr Quenching by H <sub>2</sub> . Also shown is the Normalized Radiative Rate, R*.	78
31.	Comparison of Calculated and Experimental H-Atom TALIF Quenching by Acetylene.	81
32.	Comparison of Data with Calculated Quenching Curves fitted both with and without L-State Mixing and Translational Cooling for Quenching of H-Atom TALIF by H <sub>2</sub> Gas.	83

33.	Quenching of H-Atom TALIF by Helium. Solid curve is calculated from represented model. The upper curve is calculated based on data from Reference 51.....	85
34.	H-Atom TALIF Quenching by O <sub>2</sub> (top) and Argon (bottom). . . . .	88
35.	The GEC Reference Cell . . . . .	95
36.	Experiment Layout Schematic for H-Atom TALIF . . . . .	100
37.	TALIF H-Atom Signal Profiles in GEC Reference Cell for Different H <sub>2</sub> Pressures. Power deposited in plasma is 30 watts. . . . .	104
38.	Quenching Corrected TALIF Signal Profiles from Fig. 37 . . . . .	106
39.	TALIF Signals Observed at Points Near the Driven and Grounded Electrodes . . . . .	107
40.	TALIF Signals, Corrected for Quenching, Near the Driven and Grounded Electrodes . . . . .	108
41.	H-Atom Balmer- $\alpha$ Emission Profiles in GEC Reference Cell as a Function of H <sub>2</sub> Pressure .....	111
42.	Quenching Corrected H-Atom Balmer- $\alpha$ Emission Profiles . . . . .	113
43.	Plasma Current as a Function of H <sub>2</sub> Pressure in GEC Reference Cell. . . . .	114
44.	Total Plasma Voltage and DC Bias as a Function of H <sub>2</sub> Pressure in GEC Reference Cell. . . . .	116
45.	Comparison of Maximum H-Atom Density and the Product of Current and Pressure as a Function of Pressure . . . . .	117
46.	Energy Level Diagram Illustrating TALIF Schemes for Ground State Atomic Nitrogen . . . . .	121
47.	Diagram of N Atom TALIF Experimental Apparatus . . . . .	126
48.	Spatial Profile of N Atom Concentration in 3 Torr RF Discharge . . . . .	128

## 1. Introduction

The active and downstream plasma processing of semiconductor devices and surface property modifications of aerospace materials are widely used in DOD industries. The design and the operations of the present generation of the plasma processing reactors are optimized by mostly empirical parameterizations. The scale-up of the reactor design and/or modification of the processing requirement cannot be readily achieved by using only such an empirical approach. Rather a quantitative understanding of the physics and chemistry of the processes which occur in reactive RF glow discharges is necessary to alleviate this problem.

In recent years, a variety of plasma processing techniques are finding ever widening applications in both the research into, and production techniques for, the processing of electronic materials and surface modification. It has been the main thrust of this effort to develop laser plasma diagnostics, specifically within the traditional planar electrode RF design, but which are transferable between reactors. The diagnostics can be used to probe reactive species both in bulk and near-surface plasma regions, and ultimately yield reactor independent information on key reactive species. Such diagnostics once developed and proven can be applied directly to a variety of reactors at various locations.

The present work rests on the foundation of work performed under an earlier contract (F33615-89-C-2921). In this earlier work we demonstrated our ability to make high resolution 4-dimensional (space-time) maps of reactive ground state H-atom concentrations in an RF plasma reactor using two-photon allowed laser induced fluorescence (TALIF) techniques. During the period of the present contract we have extended this early work in a variety of ways including:

- Studies of the plasma surface interface using the H-atom TALIF diagnostic
- The extension of the technique to map reactive O-atom densities
- Studies of the effect on the TALIF diagnostic of stimulated emission from O atoms in plasmas
- Studies of fluorescence quantum yields to extend this diagnostic to higher pressures
- Demonstration of the portability of the technique by its application to a standard reference cell reactor
- Preliminary studies of the extension of the TALIF diagnostic to N atoms

Each of the above topics is described in detail in separate sections of this report. The Bibliography lists publications and presentations based upon work supported by this contract.

2. TALIF as a probe for heterogeneous processes in hydrogen plasmas

A complete understanding of the complex gas-surface chemistry occurring in semiconductor processing environments requires detailed knowledge of the concentration profiles of reactive species in the plasma (especially near surfaces) and their temporal evolution during both the discharge and the afterglow. Among optical diagnostics, laser-induced fluorescence (LIF) and particularly multiphoton techniques have been used most extensively for the detection of atomic species<sup>1</sup> (the most abundant reactive species in the plasma), because of their generally nonintrusive nature and characteristic high degree of spatial and temporal resolution. These advantages have been explored in the detection of atomic oxygen<sup>2,3</sup> and hydrogen,<sup>4</sup> and CF and CF<sub>2</sub> radicals.<sup>5,6,7</sup>

Quantitative analysis of the spatial and temporal distribution of a species leads to an estimation of the reactivity between the species and the surface, in terms of the fraction of the flux of species that are removed by the surface. Concentration gradients adjacent to surfaces have been used to approximately estimate the reaction coefficient of CF<sub>2</sub> and CF radicals on various surfaces.<sup>5,8</sup> Temporal profiles in the afterglow of a pulsed discharge have been also used to determine the reaction probability of CF, CF<sub>2</sub>, and CF<sub>3</sub> radicals,<sup>9,10</sup> as well as that of O atoms<sup>11</sup> on the reactor surfaces. Recently, we reported spatially and temporally resolved atomic concentrations of hydrogen, detected by two-photon absorption laser-induced fluorescence (TALIF), in a pure H<sub>2</sub> discharge.<sup>12,13</sup> We showed that neutral diffusion dominates the evolution of the H-atom concentration across the interelectrode space, from the production regions to the electrode surfaces where H atoms are significantly absorbed on metallic, e.g., stainless-steel surfaces,<sup>12</sup> whereas they are nearly reflected on Si or GaAs surfaces.<sup>13</sup>

In the present section we describe work in which we obtain both the temporal and spatial profiles of H atoms across the entire interelectrode distance to use as independent but complementary means in the estimation of the loss coefficients  $\gamma$  of H atoms on a variety of surfaces that confine the  $H_2$  plasma. We generalize the simple model presented in the past<sup>12</sup> to account for the loss of H atoms on two electrode surfaces, characterized by different loss coefficients. As we will show, spatial profiles are particularly sensitive in determining high  $\gamma$ 's, characteristic of most metallic surfaces, while temporal profiles are more sensitive in determining low  $\gamma$ 's, characteristic of oxidized surfaces.

#### A. Experiment

The experimental apparatus has been described in detail elsewhere.<sup>11,12,13</sup> Briefly, the glass reactor, fitted with quartz windows for laser excitation of the plasma in the ultraviolet, bears two parallel plate electrodes of 50 mm in diameter separated by 18 mm. An electrical discharge driven at 10 MHz by a signal generator was produced between the electrodes by an ENI Model 3200L power amplifier connected to the top electrode. The power was usually maintained at low values, around 10 W, except in cases where higher values were desirable.

The discharge was operated in both the continuous mode and the pulsed mode with a repetition rate of 20 Hz. To achieve a pulsed discharge the output of the RF signal generator was amplitude modulated before it was amplified. Pulse widths were varied by an adjustable gate between 0 and 2 ms and the delay between the onset of the discharge and the firing of the laser beam was varied by means of a computer controlled delay generator to allow detection of the temporal decay of the atomic H population after the discharge was extinguished.

The  $1s^2S$  ground state H atoms produced in the 3 Torr pure  $H_2$  discharge were excited to

the  $3s^2S$  and  $3d^2D$  states by absorbing two 205-nm photons. The light in the UV was produced through a series of nonlinear techniques as follows. The 615-nm output of the DCR-2 dye laser, which was pumped by an Nd-YAG laser and operating on SR-640 dye, was doubled by a KDP crystal in a Quanta-Ray WEX to produce 307-nm light. Collimated 307 nm and 615 nm light were then mixed in a CSK Barium Borate (BBO) crystal to routinely produce 0.5 mJ/pulse of 205-nm light. Separated from the other wavelengths by means of a Pellin-Broca prism, the 205-nm light was focused by a quartz lens on the vertical axis connecting the centers of the electrodes. Ground state H atoms were detected by their subsequent emission of Balmer alpha 656 nm light. The fluorescence was collected at right angles by a system of lenses and it was directed through a 10 nm filter centered at 656 nm on an ITT photomultiplier tube (PMT). The PMT signal processed on a Tektronix DSA 601 digital analyzer was then transferred to a personal computer.

The reactor was mounted on *X-Y* translation stage that was computer controlled. Spatial information was obtained in these experiments by translating the RF reactor perpendicularly with respect to both the laser beam and the collection optics. That allowed us to probe the atomic concentration across the interelectrode distance with a resolution determined by the size of the laser beam at focus, estimated at  $100 \mu\text{m}$ . Calibration of the collection efficiency was necessary for probing the regions  $\leq$  mm away from each electrode surface (regions of the plasma that are of high interest) because of the occultation of the viewing solid angle by the electrode surfaces. The collection efficiency was measured in an experiment where, in the absence of a plasma,  $\text{C}_2\text{H}_2$  was photolysed by 205-nm light and the H fragment was subsequently detected by TALIF.

The surface of the bottom electrode was varied by placing on it Si wafers covered with

different metal depositions ( $\approx 0.2 \mu\text{m}$ ). The wafer was  $\approx 0.5$  mm thick and its diameter was 50 mm, completely covering the electrode surface. This way we eliminated any effects caused by the nonhomogeneity of electrode surfaces on the axial profiles of H atoms.

#### B. Results and discussion

Spatial variations in the steady-state concentration of H atoms in a 10 W, 3 Torr  $\text{H}_2$  plasma are shown in Fig. 1. Data points were taken every 0.5 mm along the interelectrode distance, and the intensities were converted to absolute concentrations by means of a titration technique described in detail elsewhere.<sup>12</sup> The concentrations have been also corrected for the quenching of the laser-excited state by  $\text{H}_2$  at 3 Torr.<sup>14,15</sup> It appears that the presence of various materials that cover the bottom electrode (with a stainless-steel top electrode) alters the spatial distribution of atomic hydrogen in the interelectrode space, and results in concentration gradients varying from nearly zero adjacent to Si and Al surfaces to much higher values near stainless-steel (SS) and Ni surfaces.

The temporal behavior of the H concentration in the afterglow of the plasma for 40 W input power in 3 Torr  $\text{H}_2$  is shown in Fig. 2, with the measurements taken at 2 mm from the bottom electrode surface of the indicated material. The H concentration decays much faster near the Ni and SS surfaces than near the Al or Si surfaces. The decays are single exponential, as shown by the linearity of the semi-logarithmic plots, for all the materials present on the electrode surface with the exception of data points taken at very short time ( $t-t_0 < 0.3$  ms) in the case of SS and Ni.

#### 1. Model

The observation of the first-order decay for H atoms in the afterglow, as well as the

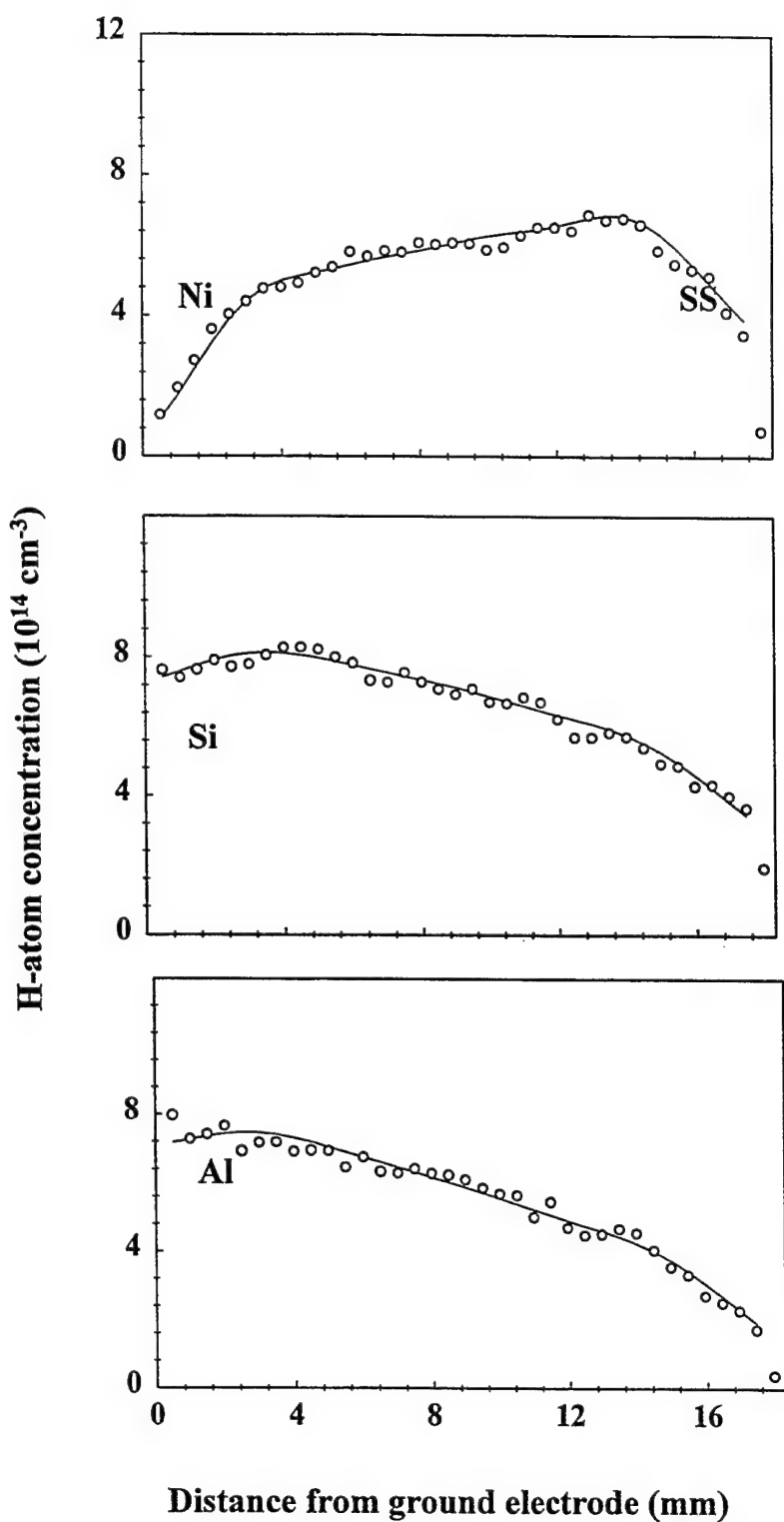


Figure 1. Spatial profiles of H-atom concentration at steady-state discharge conditions with the indicated materials (Al, Si, Ni) loaded on the ground electrode (at 0 mm).

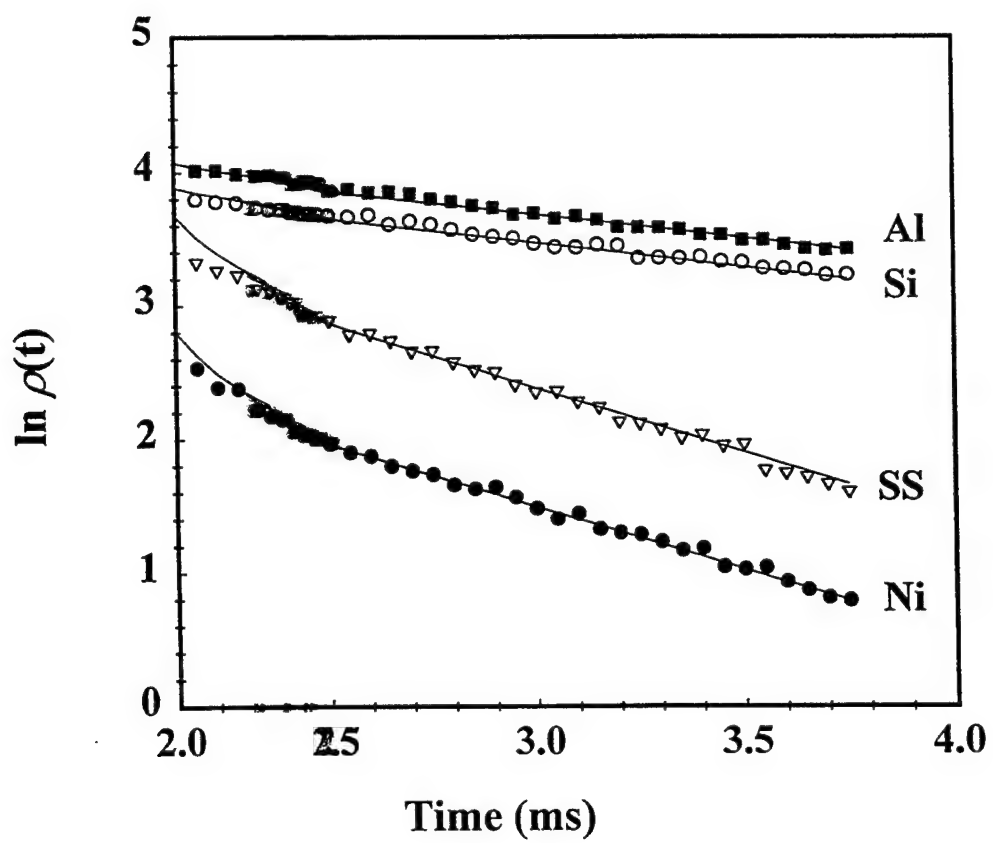


Figure 2. Temperature profiles of H atoms taken in the discharge afterglow ( $t > 2$  ms) and fits with parameter the loss coefficient  $\gamma$  of the surfaces.

existence of significant concentration gradients adjacent to electrode surfaces suggest that surface removal is the dominant process for H atom destruction in the 3 Torr H<sub>2</sub> discharge. Also the m<sup>1/2</sup> dependence of the decay rates suggests that diffusion is the dominant mechanism governing the evolution of the atomic concentrations in the discharge we study. Therefore, a simple model for the mass transport by diffusion from the production regions towards the boundaries, where heterogeneous processes for the H atom removal exist, may describe the spatial and temporal measurements presented above. The model incorporates the following assumptions: First, the *gas phase* recombination is negligible as indicated by the simple exponential decay of the atomic hydrogen population. Second, the H atoms are destroyed only on the metallic electrode surfaces which induce catalytic recombination and therefore represent sinks for H atoms. Third, *neutral* diffusion governs the movement of the H atoms towards regions of reduced atomic concentration in both the discharge and the afterglow. Finally, the production of H atoms takes place in narrow regions in the discharge. These regions roughly coincide with the visibly brightest portion of the plasma, indicative of regions of high excitation and dissociation. The production of energetic species at regions located several millimeters away from the surfaces, has been indicated previously for species such as F\* metastables,<sup>16</sup> O atoms,<sup>17</sup> and BCl radicals<sup>18</sup> at high frequencies.

Since our detection point is usually centered above the electrode surfaces, the diameter of which (50 mm) is a lot bigger than the distance between them (19 mm), a one-dimensional model would be sufficient for the description of our data in the RF cell. The general case of two boundary surfaces with loss coefficients  $\gamma_1$  and  $\gamma_2$  is considered, so the model provides a way to quantify the gas-surface interactions. Let the production of H atoms take place at point sources near the sheaths (as the experimental evidence presented in section A supports) localized at

distances  $x=x_0$  and  $x=a-x_0$  from the electrode surfaces separated by a distance  $a$ . Although the production of H atoms takes place over the time scale of the period of the discharge (100 ns), we are mostly interested in a time-averaged production over a millisecond time-scale, given the fact that the temporal behavior shown in Fig. 2 exhibits a characteristic time of  $\sim 1$  ms. A time-averaged production (at a constant rate  $R_0$ ) can be represented by two equally-weighted delta functions,  $R_0[\delta(x-x_0)+\delta(x-a+x_0)]$ , centered at the sources (*i.e.* at  $x_0$ ,  $a-x_0$ ). The surface removal of H atoms gives rise to gradients in the concentration  $\rho$  which depend on the reactivity between the atomic species and the surface and can be expressed in terms of a loss coefficients  $\gamma$ , defined as the ratio of the flux of particles lost to the total flux of particles impinging on a surface. The flux,  $J_\ell$ , of particles lost on a surface located at  $x=0$  is<sup>19</sup>

$$J_\ell = D(\partial \rho / \partial x)_{x=0} \quad (1)$$

(according to Fick's law), while the flux,  $J_r$ , of particles that impinge on the surface and recoil is

$$J_r = (v\rho/4)_{x=0} \quad (2)$$

where  $D$  is the diffusion coefficient,  $v$  is the mean thermal velocity of H atoms, and  $\rho_{x=0}$  is the gas-phase atomic concentration at the surface. A definition of  $\gamma$ ,

$$\gamma = J_\ell / (J_\ell + J_r) = \{D(\partial \rho / \partial x) / [D(\partial \rho / \partial x) + (v\rho/4)]\}_{x=0} \quad (3)$$

exhibits reasonable behavior in the limits  $\rho=0$  and  $\partial \rho / \partial x=0$ , corresponding to totally absorbing ( $\gamma=1$ ) and totally reflecting surfaces ( $\gamma=0$ ) respectively. Equation (3), written for two surfaces located at  $x=0$  and  $x=a$  with loss-coefficients  $\gamma_1$  and  $\gamma_2$  respectively, can be rearranged to give the following expressions for the boundary conditions of our problem:

$$(\partial \rho / \partial x)_{x=0} = [v\rho \gamma_1 / (4D(1-\gamma_1))]_{x=0} \quad (4a)$$

$$(\partial \rho / \partial x)_{x=a} = [-v\rho\gamma_2/[4D(1-\gamma_2)]]_{x=a} \quad (4b)$$

Thus, the one-dimensional diffusion equation that includes production of H atoms at a rate  $R_0$  is

$$\partial \rho / \partial t = D \partial^2 \rho / \partial x^2 + R_0 [\delta(x-x_0) + \delta(x-a+x_0)] \quad (5)$$

The general solution of Eq. (5), subject to the boundary conditions given in Eqs. (4a) and (4b), can be expressed as a series

$$\rho(x,t) = \sum \rho_n(x) [1 - \exp(-D\lambda_n^2 t)] \quad n=1,2,3,\dots \quad (6)$$

where

$$\rho_n(x) = (2R_0/aD\lambda_n^2) \cos(\lambda_n x - \delta_n) [\cos(\lambda_n x_0 - \delta_n) + \cos(\lambda_n(a-x_0) - \delta_n)], \quad (7)$$

$\lambda_n$  is the  $n$  root of the equation,

$$\lambda_n a = \tan^{-1}[\gamma_1 v/(4(1-\gamma_1)D\lambda_n)] + \tan^{-1}[\gamma_2 v/(4(1-\gamma_2)D\lambda_n)] + n\pi, \quad (8)$$

and the phase  $\delta_n$  is given by

$$\delta_n = \tan^{-1}[\gamma_1 v/(4(1-\gamma_1)D\lambda_n)] \quad (9)$$

For simplicity, we tried first to fit Eqs. (6) and (7) to the experimentally determined spatial profiles shown in Figs. 3, 4, and 5 with  $\gamma=1$  (totally absorbing surfaces). These equations fit well the steady-state ( $t \rightarrow \infty$ ) spatial distribution (Fig. 3), as well as the spatial profiles at various times after turning the discharge on (Fig. 4) or off (Fig. 5), as it is demonstrated by the best fit

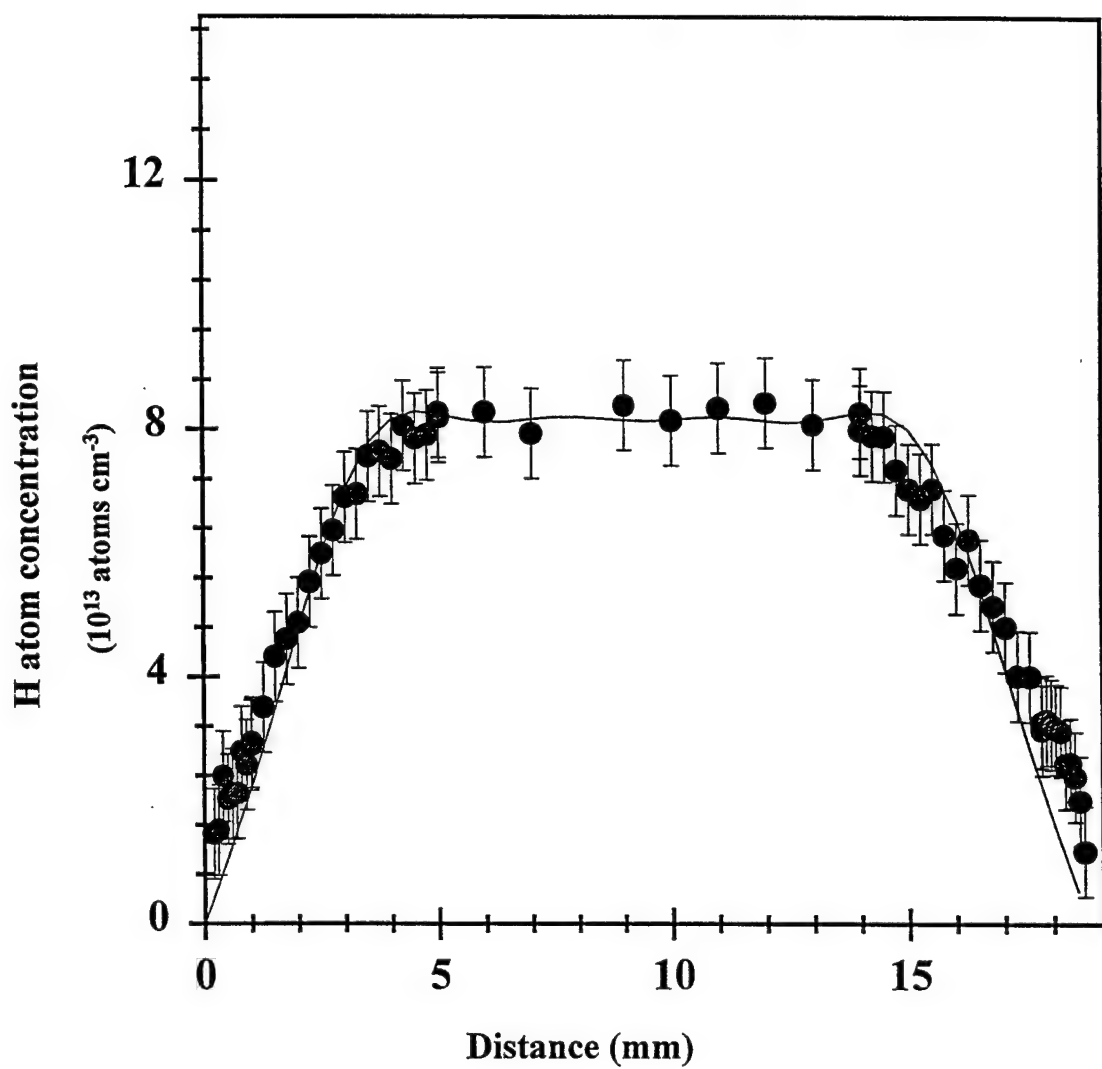


Figure 3. Typical H-atom concentration profile as a function of the distance from the ground electrode (at 0 mm) in a 10-MHz continuous  $\text{H}_2$  discharge.

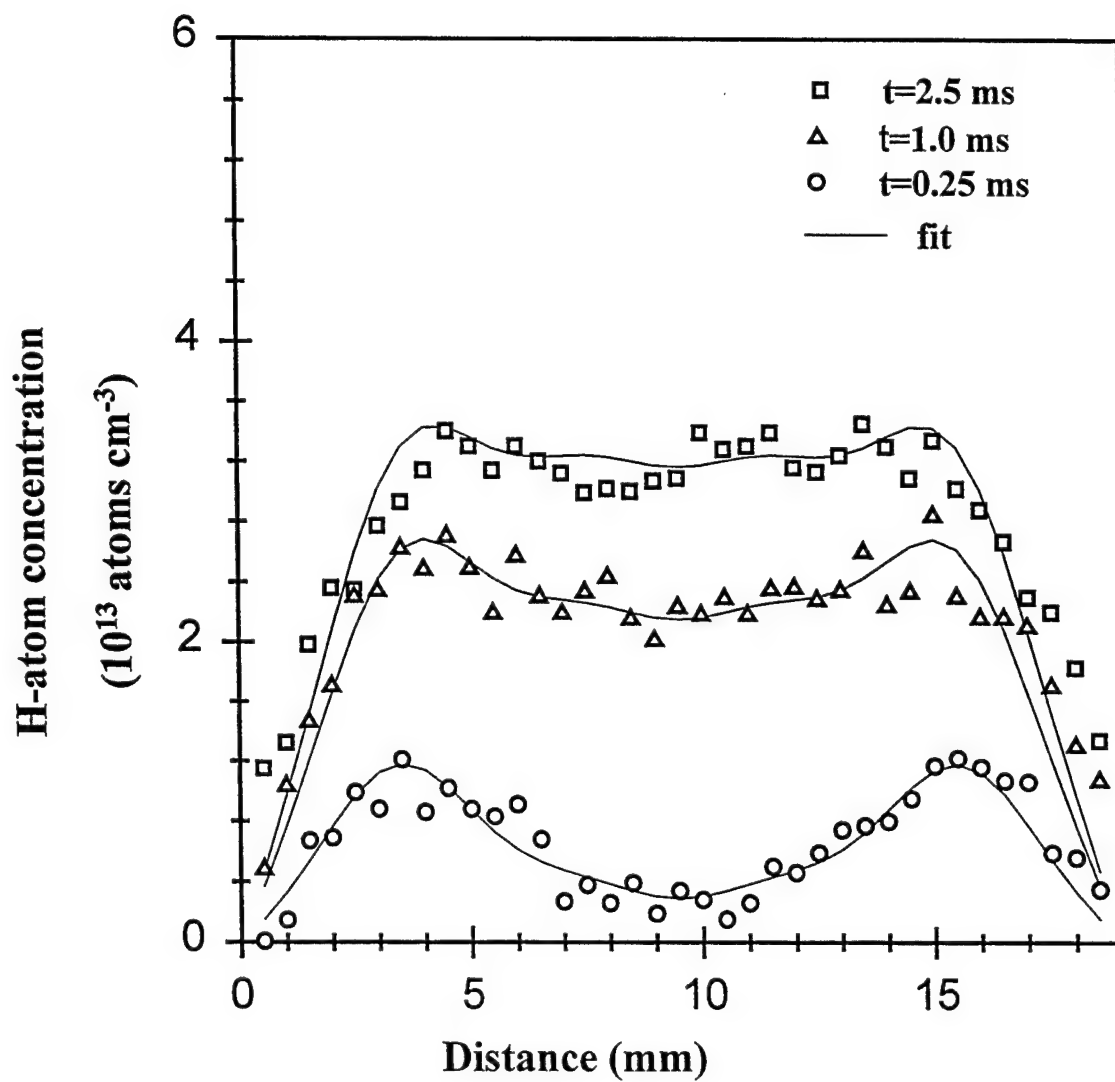


Figure 4. Temporal evolution of H-atom spatial profiles after the onset of a pulsed discharge; experimental data and simulated results at  $t=0.25$ ,  $1.0$ , and  $2.5$  ms.

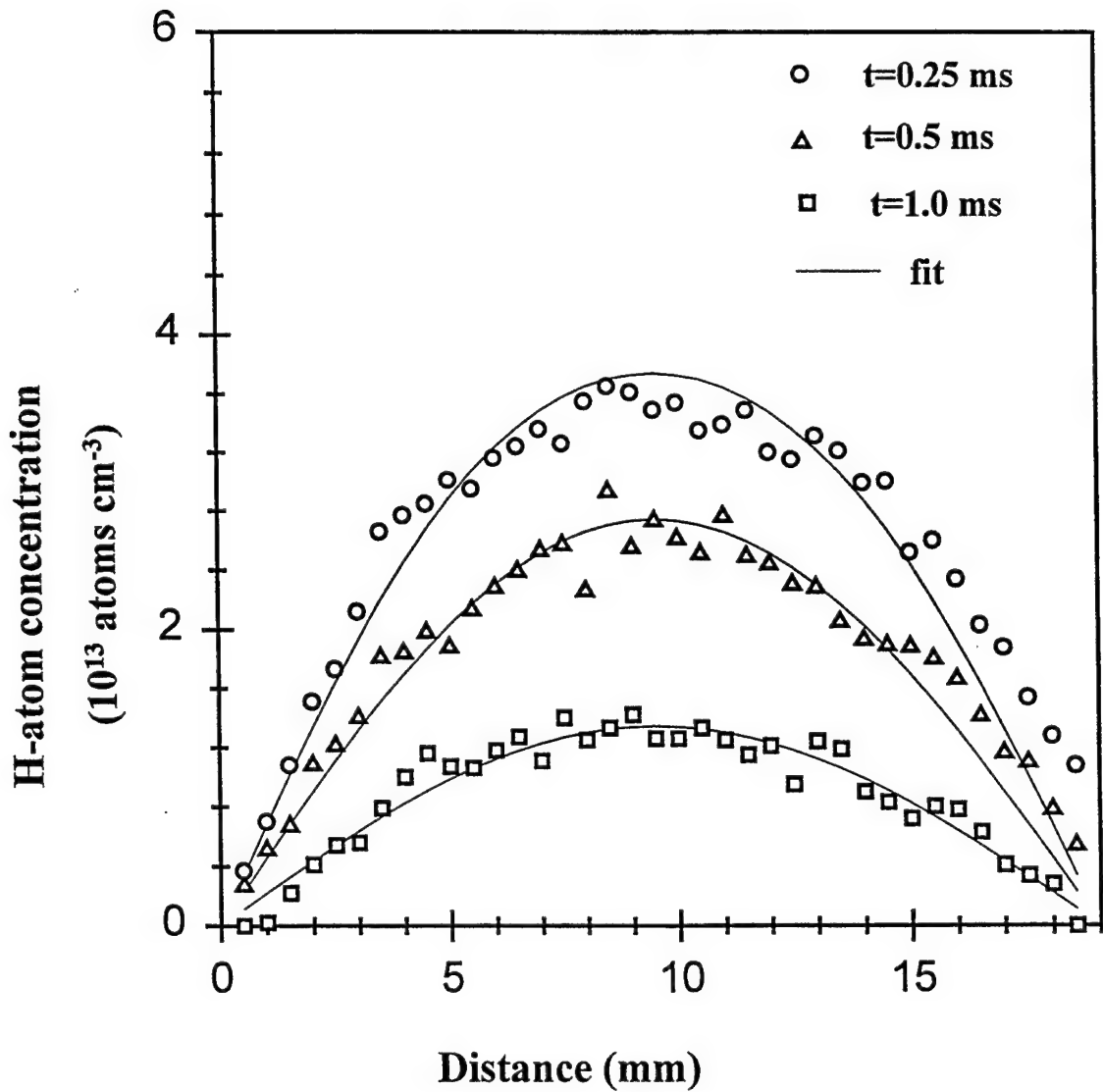


Figure 5. Decay of H-atom spatial profiles in the afterglow of a discharge (turned off at  $t_0 = 2 \text{ ms}$ ); data and simulated results at 0.25, 0.5, and 1.0 ms after  $t_0$

curves (obtained by a least square fit program) shown with solid lines in these figures. Thus, we estimated the position of the sources to be at  $3.4 \pm 0.2$  mm away from the electrode surfaces, the production rate  $R_o$  to be  $(16 \pm 2) \times 10^{16}$  atoms/cm<sup>2</sup>sec and  $31 \times 10^{16}$  atoms/cm<sup>2</sup>sec in the pulsed and the cw discharge respectively (operated at 5 W and 10 W), and the value of the diffusion coefficient D to be  $380 \pm 60$  cm<sup>2</sup>/s. This value agrees well (within the uncertainty) with that of 440 cm<sup>2</sup>/s as calculated from Gilliland's semiempirical equation.<sup>20</sup> This equation based on kinetic theory assumes a  $T^{3/2}$  dependence for the diffusion coefficient and it is evaluated at 300 K (we assume thermally equilibrated H atoms at room temperature).

However, the experimental concentration gradient near the electrode surfaces (Fig. 4) is smaller than that calculated from Eqs. (6) and (7), an indication that the electrode surfaces are partially absorbing with a loss coefficient  $\gamma_{ss}$  for H atoms. A better fit was obtained by solving the diffusion equation for boundary surfaces with a loss coefficient  $\gamma_{ss}=5 \pm 1\%$  for hydrogen and deuterium atoms, as shown in Fig. 6. The loss coefficients for hydrogen and deuterium are equal, as one would expect from Eq. (3) since the mean thermal velocity and the diffusion coefficient both vary as  $m^{-1/2}$ . This result further verifies the fact that the balance between diffusion and atom removal at the surface establishes the observed concentration gradient close to the electrode surfaces.

In the afterglow of the discharge (turned off at  $t=t_0$ ), the solution of Eq. (5) becomes:

$$\rho(x,t) = \sum \rho_n(x)[1 - \exp(-D\lambda_n^2 t_0)] \exp[-D\lambda_n^2 (t-t_0)] \quad n=1,2,3,\dots \quad (10)$$

As it is obvious from the linearity of the semilogarithmic plots (Fig. 7) for times  $t-t_0 > 0.3$  ms, only the first term of Eq. 10 is significant and this fact dictates a predominant decay of the H

## H-atom Decay After Plasma Extinction

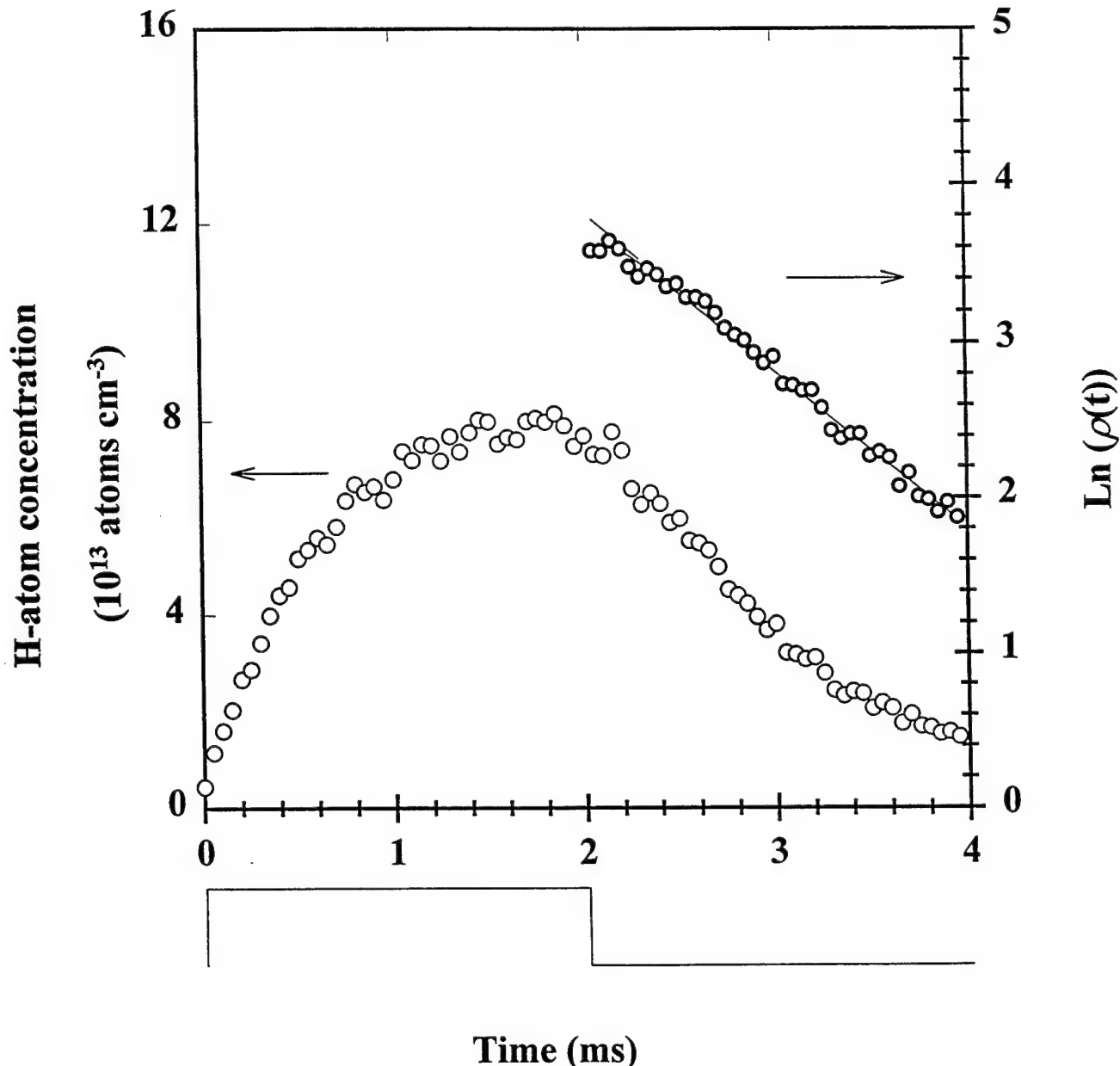


Figure 6. Temporal profile of H-atom concentration in a pulsed discharge (turned off at  $t_0 = 2 \text{ ms}$ ). A single exponential fits well the H-atom decay in the afterglow ( $t > 2 \text{ ms}$ ).

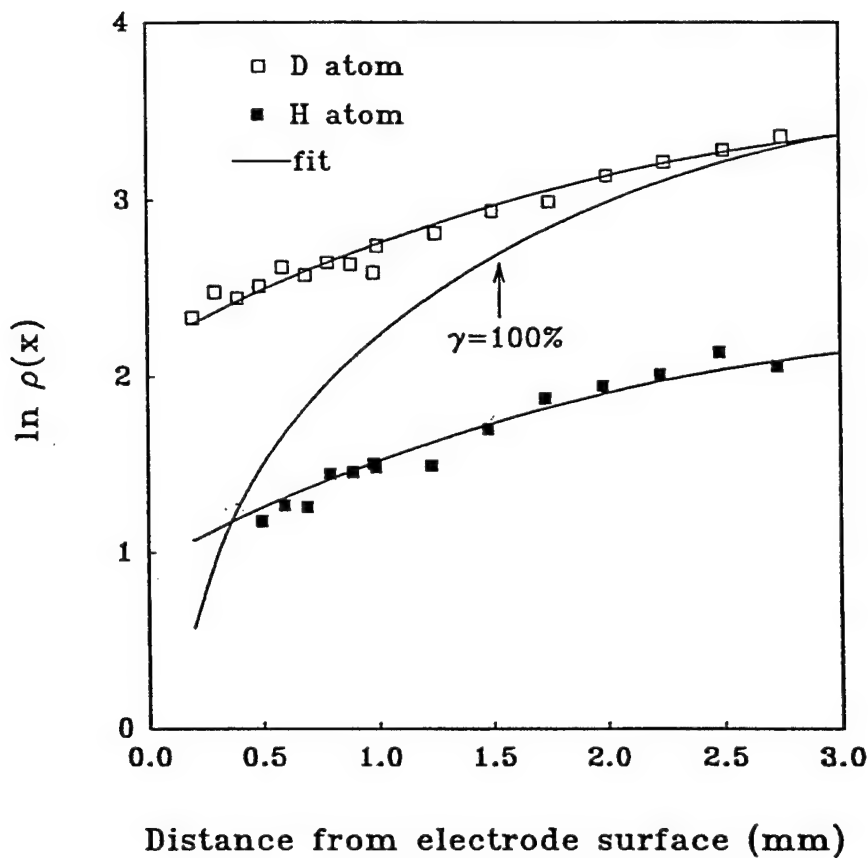


Figure 7. Temporal profile of H-concentration in a pulsed discharge (turned off at  $t_0=2$  ms). A single exponential fits well the H-atom decay in the afterglow ( $t>2$  ms)

population with a rate  $k_d = -D\lambda_1^2$ , where  $\lambda_1$  is the first root of Eq. (8). Higher order terms in Eq. 10 are important only for times  $t-t_0 \leq 0.2$  ms, while they contribute less than 5% in the decaying concentration at times  $\geq 0.2$  ms after the discharge is turned off. The first term of the series relates the time constant  $\tau$  of the exponentially decaying H concentration to the diffusion coefficient D :  $1/\tau = D\lambda_1^2$ . We thus calculate the diffusion coefficients for H and D atoms to be  $355 \pm 30$  cm<sup>2</sup>/s and  $220 \pm 15$  cm<sup>2</sup>/s respectively. Actually, the comparison of the diffusion coefficients of these atoms provides a test for the model discussed above, since the diffusion coefficient depends inversely on the square root of the mass of the diffusing particle. The estimated values essentially agree with the expected  $2^{1/2}$  ratio within the experimental uncertainty.

In Fig. 8 we have plotted the variation of the steady-state concentration of H atoms (normalized to its value at  $x=3$  mm) over a small distance from the electrode surface that bears the surfaces of various  $\gamma$ 's in a 3 Torr H<sub>2</sub> discharge, as calculated from Eq. (6) with  $t \rightarrow \infty$ . As one expects, surfaces with small  $\gamma$  result in almost flat concentration profiles, while surfaces with larger  $\gamma$ 's result in significant concentration gradients adjacent to them. From the figure, we also observe that although the concentration gradients do not change significantly for  $\gamma$  in the range 0.1%-1%, they do vary sharply at higher values of  $\gamma$ : 1%-50%.

In Figs. 9 (a) and (b) we have plotted the calculated decay rates as a function of the loss coefficient of H atoms on the boundary surfaces. The expected decay rates vary monotonically as a function of the loss coefficient of a surface. At the pressure of 3 Torr, used throughout the experiments presented above, Fig. 9 (a) shows that the decay rates increase by a factor of 5 with  $\gamma$  varying from 0.1%-1%, and by a factor of 2 only in the next range  $1\% \leq \gamma \leq 10\%$ , while the

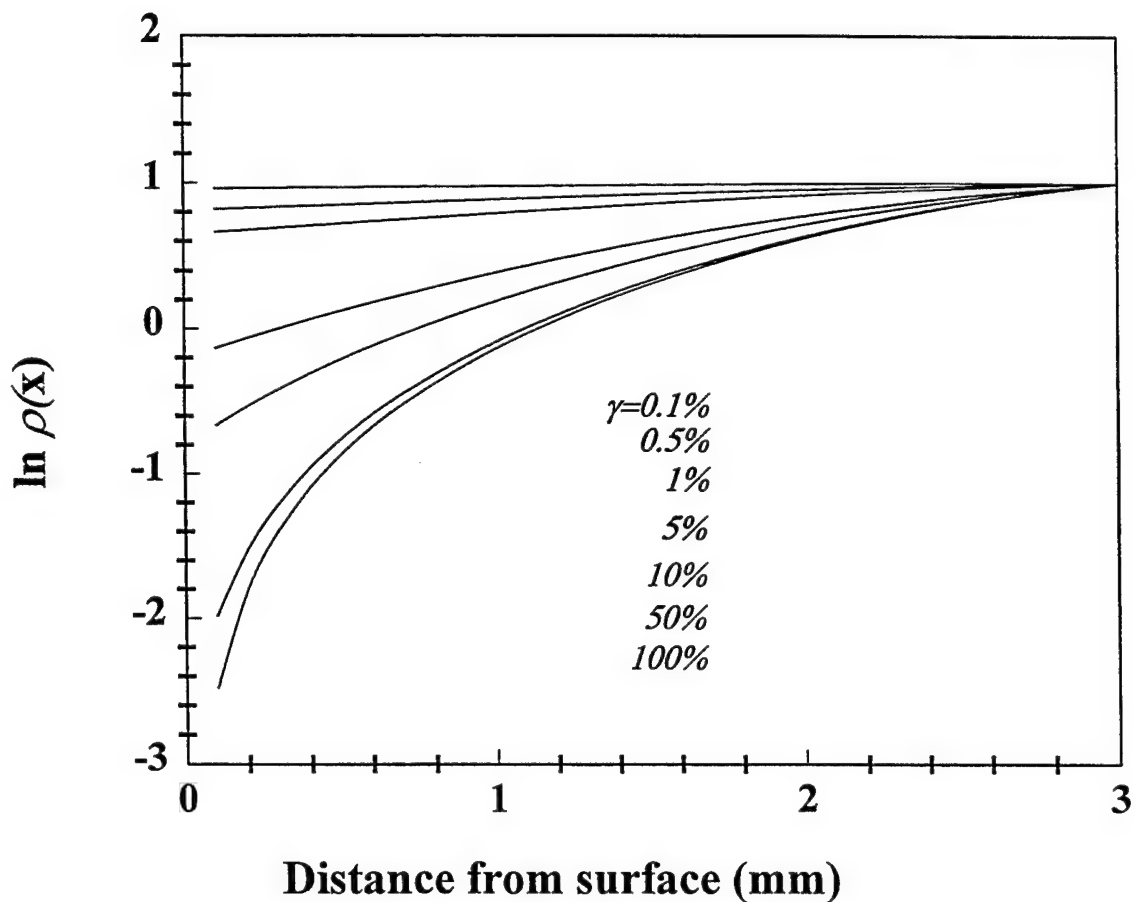


Figure 8. Simulations of the variation of H-atom concentration over a small distance from a surface characterized by a loss coefficient  $\gamma$  varied from 0.1% to 100%.

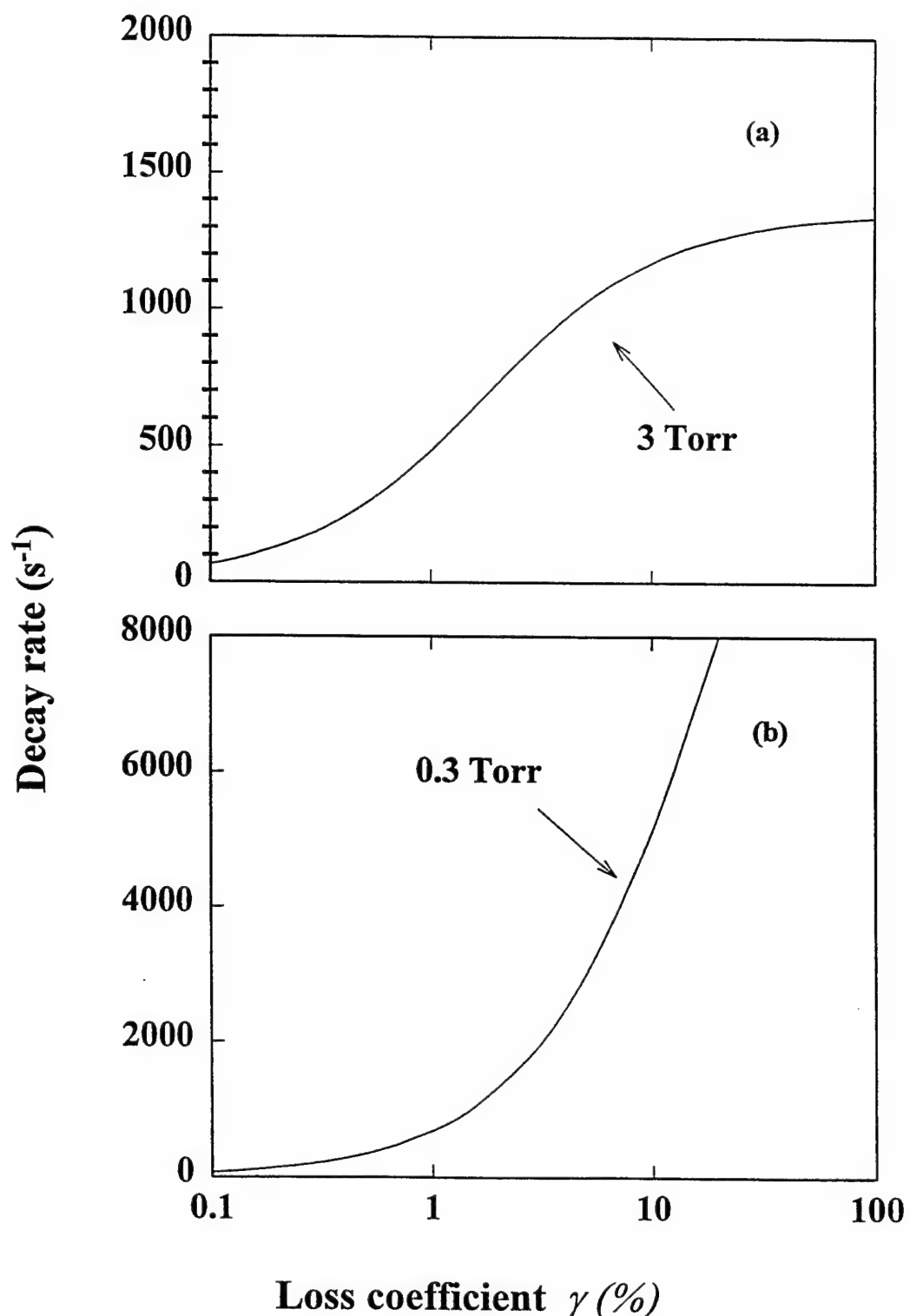


Figure 9. Simulations of H-atom concentration decay rates in the discharge afterglow as a function of the loss coefficient  $\gamma$  of the electrode surface

decay rates almost plateau at higher values of  $\gamma > 10\%$ . Furthermore, Fig. 9 (b) indicates that the sensitivity range for  $\gamma$  is extended to well above 10% at a much smaller pressure (0.3 Torr).

To conclude, decay rates obtained from the temporal profiles can accurately determine small loss coefficients, since  $k_d$  is proportional to  $\gamma$  in the limit where  $\gamma \rightarrow 0$ . For example, the sensitivity to determine  $\gamma$  for H atoms in a 3 Torr discharge is reasonable for  $\gamma < 10\%$ , while for higher  $\gamma$  values a typical experimental error ( $\pm 10\%$ ) would result in a significant error in determining  $\gamma$  ( $\geq \pm 40\%$ ). However, spatial profiles provide more accurate means to yield and extend the upper limit of accurately determined  $\gamma$  values to  $\sim 50\%$ . Otherwise, temporal profiles should be taken in a smaller discharge pressure (for example in 0.3 Torr) that allows extension of the range of accurate  $\gamma$  values (to  $\sim 50\%$ , as shown in Fig. 9 (b)).

## 2. Loaded H<sub>2</sub> discharges

Since the first report of Si etching by neutral hydrogen atoms in a low pressure plasma,<sup>21</sup> radio frequency (RF) reactors have been widely employed in the fabrication of microscopic devices. The application of reactive plasma methods in silicon technology has been extended to the technology of GaAs as well, for deposition, etching, cleaning and passivation.<sup>22,23,24,25</sup> Beyond the wide use of these discharges, there is however a need for a more fundamental understanding of plasma-surface interactions. In particular, space and time resolved optical measurements are used to monitor the distribution and development of reactive species,<sup>26,27,28,29,30,31,32</sup> and therefore help to elucidate the mechanisms that lead to processing of device surfaces. In this section, we will describe spatial and temporal profiles taken in H<sub>2</sub> discharges loaded with surfaces of technological interest in microelectronics industry; Si and GaAs semiconducting surfaces and metallic surfaces. Quantitative analysis of the spatial and temporal distribution of H atoms leads

to an estimation of the reactivity between the species and the surface, in terms of the fraction of the flux of species that are removed by the surface, as we discussed in section B.1.

The samples that we loaded in the RF reactor were n-type GaAs and Si (100, 111) substrates, used without being treated, of 0.5 mm thickness. We simply placed them centered on the ground bottom electrode, very much like loading industrial processing reactors. Different metal films ( $\approx 0.2 \mu\text{m}$ ) were deposited on Si wafers in a micro-etch ion-milling vacuum system. The typical diameter of the substrates loaded in our reactor was 50 mm, when axial profiles (along the interelectrode space) were taken, so that the electrode surface was completely covered. This way we eliminated any effects caused by the non-homogeneity of electrode surfaces on the axial profiles of H atoms. However, the substrate diameter was reduced to 10 mm for the radial profiles (parallel to the electrode surface) to be taken, as it will be described in the following paragraph.

To demonstrate the dependence of the spatial distribution of H atoms on the nature of the substrate surface, we measured spatial concentrations 1.5 mm above the grounded bottom electrode (bearing the substrate) while the reactor cell was translated horizontally (radial profiles). The radial profile shown in Fig. 10(b) was taken over a 10x10 mm GaAs wafer. We observe a significant increase in hydrogen atom concentration localized over the wafer surface. A radial profile over an identical stainless steel piece, shown in Fig. 10(a), proved that the drastic change in the concentration could not be attributed to changes in the bulk properties of the discharge, or in the detection geometry, but rather to the nature of the GaAs surface. We further verified that, by depositing 2- $\mu\text{m}$ -thick gold on the GaAs wafer. A radial profile taken over the gold-coated GaAs wafer, shown in Fig. 10(c), indicates a *reduction* in the hydrogen

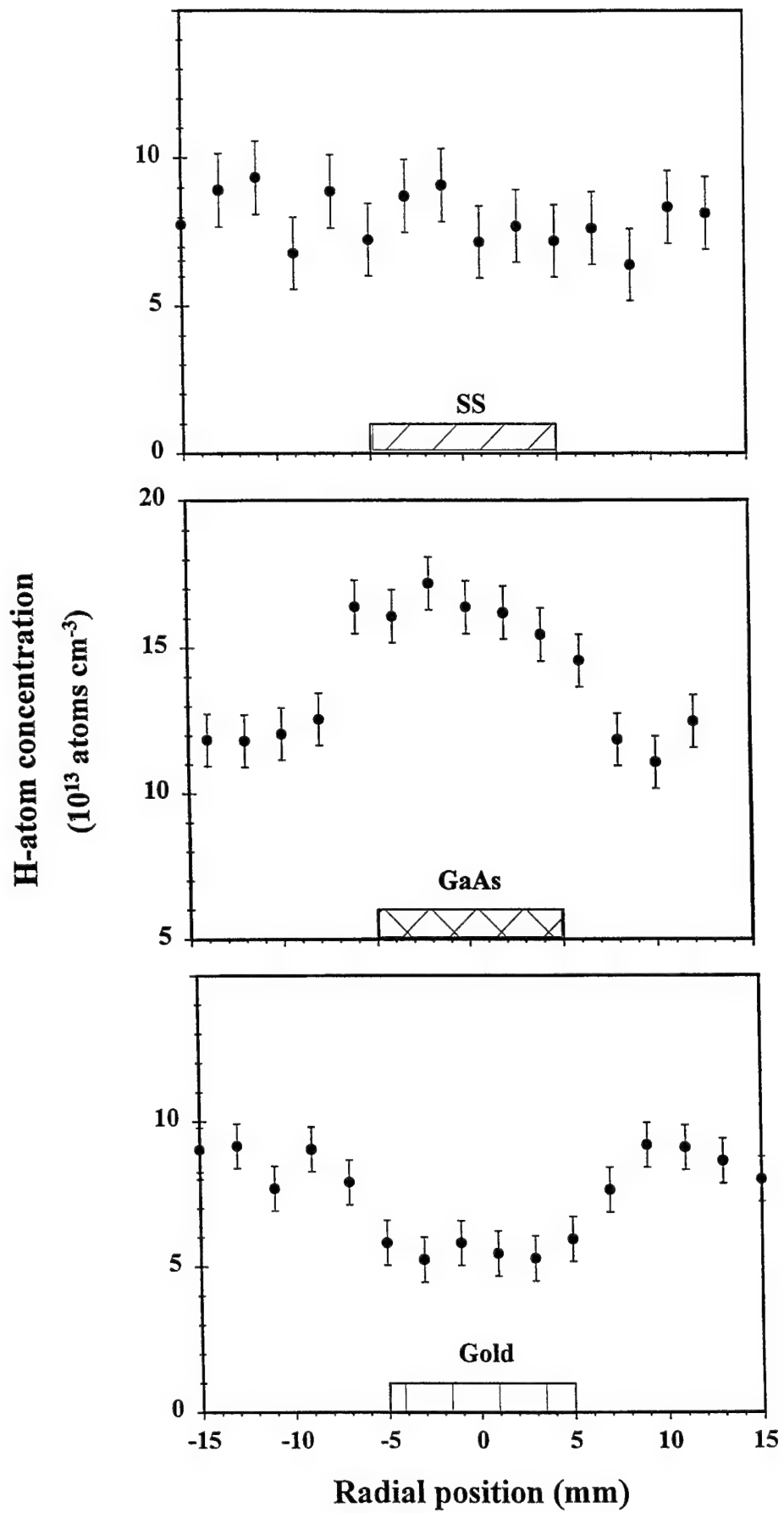


Figure 10. Comparison of H-atom radial profiles probed 1 mm above a (a) stainless-steel, (b) GaAs, and (c) gold-coated (10x10 mm) substrate, placed on the ground electrode.

concentration and suggests that certainly a surface/atomic hydrogen interaction must be responsible for the variation in the measured atomic concentrations.

By employing a *pulsed* discharge, we studied the temporal development of the hydrogen concentrations in the interelectrode space. In Fig. 11 we show hydrogen atom concentrations in a discharge loaded with a  $15 \text{ cm}^2$  GaAs wafer at various times after the onset of the discharge. Specifically, the spatial concentrations shown were measured at times  $t=0.15 \text{ ms}$ ,  $0.50 \text{ ms}$  and  $2.50 \text{ ms}$ . The profile at  $t=0.15 \text{ ms}$  indicates that the production of hydrogen atoms in these plasmas occurs in localized regions in close proximity to the electrodes. In time, the hydrogen atoms diffuse from their sources towards the center and the electrode surfaces. We observe that the spatial profile at very early times is not affected by the presence of the GaAs wafer, however, as time increases, the concentration of the hydrogen atoms builds up close to the wafer surface, resulting to the apparent spatial asymmetry of the profile taken at time  $t=2.5 \text{ ms}$ .

Spatial variations in the steady-state concentration of H atoms in a  $10 \text{ W}$ ,  $3 \text{ Torr H}_2$  plasma are shown in Fig. 1. Data points were taken every  $0.5 \text{ mm}$  along the interelectrode distance, and the intensities were converted to absolute concentrations by means of a titration technique described previously. The concentrations have been also corrected for the quenching of the laser-excited state by  $\text{H}_2$  at  $3 \text{ Torr}$ . It appears that the presence of various materials that cover the bottom electrode (with a stainless-steel top electrode) alters the spatial distribution of atomic hydrogen in the interelectrode space, and results in concentration gradients varying from nearly zero adjacent to Si and Al surfaces to much higher values near stainless-steel (SS) and Ni surfaces.

The temporal behavior of the H concentration in the afterglow of the plasma for  $40 \text{ W}$

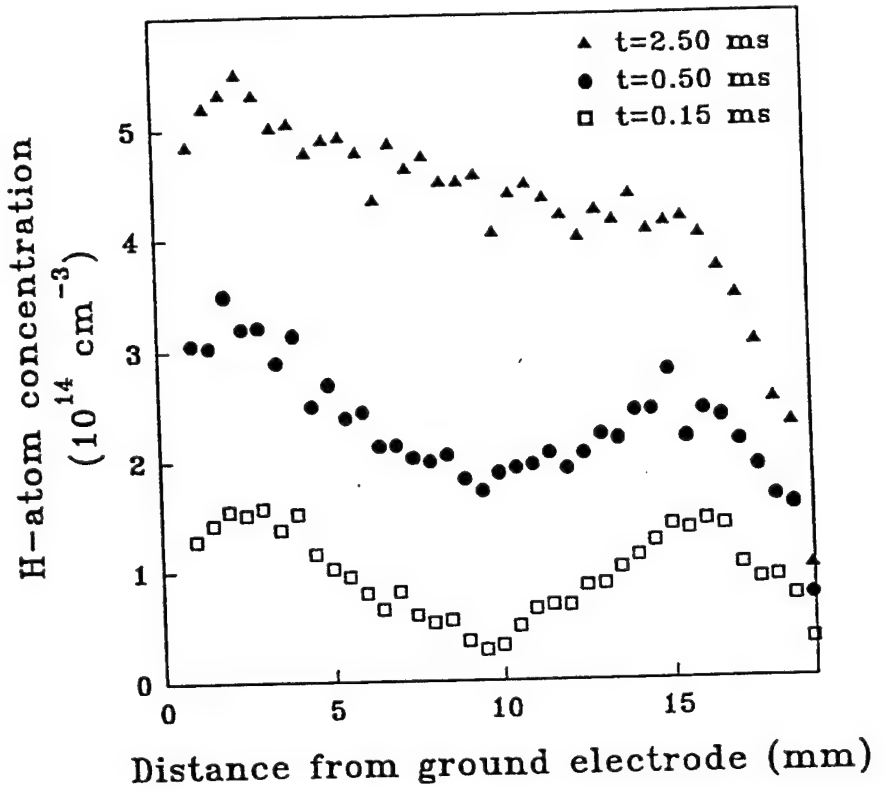


Figure 11. Evolution of H-atom spatial profiles after the onset of a pulsed discharge loaded with a GaAs wafer on the ground electrode; data points at  $t=0.15$ ,  $0.50$ , and  $2.50$  ms

input power in 3 Torr H<sub>2</sub> is shown in Fig. 2, with the measurements taken at 2 mm from the bottom electrode surface of the indicated material. The H concentration decays much faster near the Ni and SS surfaces than near the Al or Si surfaces. The decays are single exponential, as shown by the linearity of the semi-logarithmic plots, for all the materials present on the electrode surface with the exception of data points taken at very short time ( $t-t_0 < 0.3$  ms) in the case of SS and Ni.

The simple diffusion model described in section B1 was used to fit the experimental data of the spatial profiles at equilibrium ( $t \rightarrow \infty$ ), the determined parameters being the production rates  $R_0$  and the loss coefficients,  $\gamma_i$ , of the surfaces. The solid lines shown in Fig. 1 are the results of such fits with the values of  $\gamma_i$  given in the first column of Table 1. These  $\gamma_i$  values were compared with the results of measurements of the recombination coefficient of H atoms on surfaces in previous experiments<sup>33,34</sup> (see Table 1, column 3). The result for Ni is in good agreement with that from the flow tube experiments, but  $\gamma_{Al}$  and  $\gamma_{Si}$  are much smaller. We believe that a thin layer of oxide, known to be formed easily on these surfaces, is responsible for the discrepancy. In fact, oxidized surfaces are typically characterized by recombination coefficients in the order of 0.1 %.<sup>33</sup>

From least square fits of the experimental decays shown in Fig. 2, the loss coefficients for Al, Si, SS and Ni were estimated, and are given in the second column of Table 1. These fits required to fix the loss coefficient for the opposite electrode (SS), which was estimated from the spatial profiles ( $\gamma_{SS} = 3.0 \pm 1.4$  %). Both spatial and temporal profiles lead to similar values for the loss coefficients, as shown in Table 1.

**TABLE 1.** H atom surface loss coefficients

	This work		Previous investigations
	spatial	temporal	
Al	0.18±0.03 % <sup>a</sup>	0.20±0.01 % <sup>a</sup>	32 % <sup>b</sup>
Si	0.30±0.03 % <sup>a</sup>	0.25±0.02 % <sup>a</sup>	70±10 % <sup>c,d</sup>
SS	3.0±1.4 %	4.5±0.2 %	
Ni	18±3 %	20±9 %	22 % <sup>b</sup>

<sup>a</sup> oxidized materials

<sup>b</sup> See Ref. 33.

<sup>c</sup> See Ref. 31.

<sup>d</sup> See Ref. 34.

The uncertainties shown in the table represent the confidence in determining  $\gamma$  by fitting a single profile (as in Figs. 1 and 2) to Eqs. 3 and 6. The error of  $\gamma_{ss}$ , in particular, is determined from four spatial profiles taken over a period of a month. Typically, the day-to-day reproducibility of the data leads to a variation of  $\gamma$  up to 50%.

### 3. Modification of the surface loss coefficient by the plasma

#### a. Permanent modification

Because of the great importance of  $H_2$  plasmas in semiconductor processing, we exposed Si surfaces (of 111 and 100 type) in low-pressure (0.5 Torr)  $H_2/Ar$  plasmas, operated in the continuous mode. After every exposure of the surface to the low-pressure plasma for a few minutes, we measured the temporal decay of H atoms over the treated Si surface in the afterglow

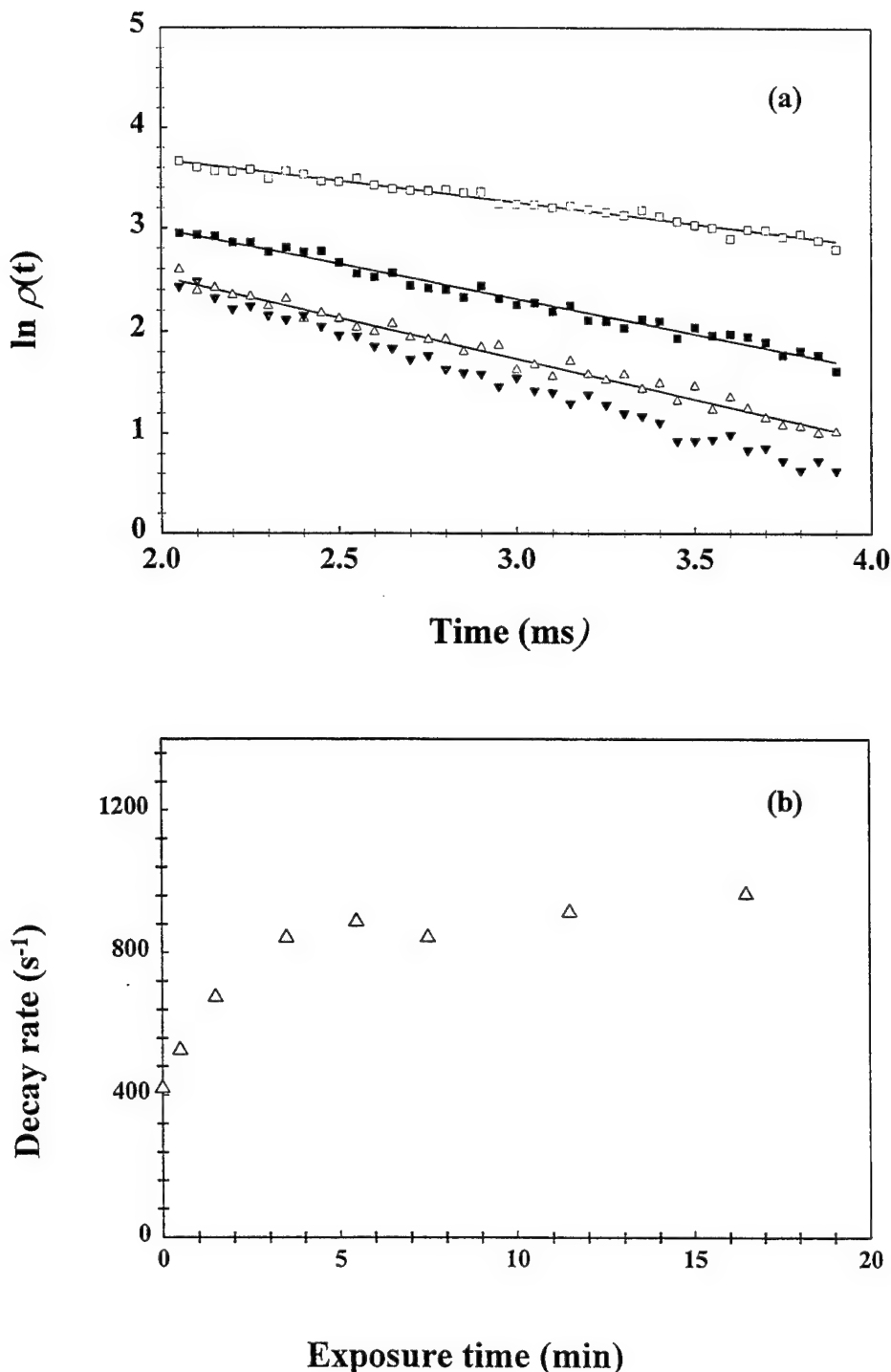


Figure 12. (a) Temporal decay of H atoms near an Si surface exposed to a low pressure  $H_2/Ar$  discharge for  $T=0, 1.5, 3.0, 16.5$  min. (b) Decay rates of H atoms as a function of exposure time  $T$ .

of a 3 Torr H<sub>2</sub> plasma. Fig. 12a shows a few representative temporal decays taken after exposure times T=0, 1.5, 3, and 16.5 minutes, respectively. The variation of the decay rates with T is shown in Fig. 12b. We observe that the decay rate increases drastically initially, while it plateaus after an exposure time T≈5 min.

This observation could result from removal of the oxide from the Si surface that has been previously reported to enhance the H consumption due to etching of SiO<sub>2</sub> and subsequent etching of Si.<sup>7</sup> However, analysis of the Si surfaces after their treatment in the plasma, by means of *ex situ* x-ray photoelectron spectroscopy (XPS), showed an unexpected change in the surface composition; a small amount of iron was deposited on the surface (estimated to be ~5% after a 10 min exposure in the low-pressure H<sub>2</sub>/Ar plasma), possibly the result of sputtering that is favored at low pressures. The measurement of the decay rates in the 3 Torr pulsed discharge could not alter the characteristics of the treated surface due to the low duty cycle of the pulsed discharge and the inefficiency of ion bombardment on the surface at the pressure of 3 Torr. An estimation of the loss coefficient that corresponds to the maximum value of the decay rate shown in Fig. 12b ( $\gamma=3.5\%$ ) is consistent with deposition of iron on the Si surface. We conclude that sputtering can cause alteration of the loss coefficient of a surface (and thus of the spatial and temporal profiles) in a direction characterized by the deposited material. The loss coefficient increases if the deposited material is characterized by a loss coefficient higher than that of the surface (as in the case of SS deposited on SiO<sub>2</sub>), and it decreases in the opposite case. Obviously, any reduction of the SiO<sub>2</sub> from the surface would be screened by the deposition of iron, since both effects would tend to increase the recombination coefficient of the surface.

Similar observations were made at a GEC RF Reference Cell installed at Wright

Laboratory,<sup>35</sup> where sputtering of electrode material onto substrates caused significant discrepancies between spatial profiles taken a few days apart, after long exposure of the substrate surfaces to the discharge. These observations reveal unintentional sputtering of electrode material in loaded discharges and demonstrate the sensitivity of the LIF diagnostics to detect, *in situ* and in real-time, changes induced by energetic plasmas on exposed surfaces.

These observations of unintentional sputtering in our reactor as well as in the Reference Cell at Wright Laboratory indicate that sputtering may be present in many industrial systems (since they are similar to our reactors) and it could lead to undesirable or deleterious effects on surfaces treated in processing reactors. And although it would be difficult to eliminate it, unintentional sputtering could be certainly reduced, once researchers are aware of its occurrence.

In order to investigate the etching of  $\text{SiO}_2$  from the Si substrate surfaces in low-pressure  $\text{H}_2$  discharges, we replaced the SS electrodes with Al ones, so that we prevent an increase of  $\gamma$  due to iron sputtering. Since Al surfaces are characterized by similar decay rates as Si ones, one would expect to readily observe the native oxide removal after long exposure to a low-pressure and high-power  $\text{H}_2$  discharge. However, we did not observe any change in the decay rates of the H atoms, within the experimental error, even after a 20-minute exposure of the surface in the discharge. This indicates that surface oxides of Si continue to cover the semiconducting surface during the time we performed the experiment. Possibly, *in situ* generation of  $\text{H}_2\text{O}$  due to reaction of H atoms with the surface oxides ( $\text{SiO}_2$ ) or with the pyrex walls of the reactor favors the reformation of these oxides on the surfaces, as water does not readily desorb from the passivated surfaces at room temperature.<sup>36,37</sup>

b. Temporary modification

From temporal profiles for H atoms taken in a pure H<sub>2</sub> discharge confined by Al electrodes, we observed a temporary change of the surface loss coefficient as a function of pressure. This observation is important since processing plasmas are routinely operated at pressures 1-10 mTorr, much lower than that we have used so far (3 Torr). We operated the discharge in the pulsed mode (low duty cycle). The pressure was varied from 4 Torr down to 0.2 Torr and the temporal decay of the atomic hydrogen was measured at 2 mm above the bottom-electrode surface. In Fig. 13 we show the variation of the decay rates as a function of pressure. The solid lines represent the calculated variation of the decay rate  $k_d$  with pressure for various  $\gamma$ 's (according to  $k_d = -D\lambda_1^2$ , where  $\lambda_1$  is the first root of Eq. (8)), assuming that H atoms are at room temperature. As shown in Fig. 13, it appears that the loss coefficient of Al increases 2-3 times as pressure decreases from 4 to 0.2 Torr. We believe that surface damage or enhanced gas-surface chemistry due to ion bombardment (ion-neutral synergism)<sup>38</sup> could be responsible for this observation. A possible increase of the species temperature with pressure<sup>39</sup> would enhance this effect even more, since it would lead to an estimation of an even smaller loss coefficient for H atoms at elevated temperatures (at high pressures), as  $k_d$  is in a first approximation proportional to  $\gamma v \sim \gamma T^{1/2}$ . The observed change is only temporary since the alteration of the loss coefficient of the surface with pressure is consistently reversible, *i.e.* the variation of  $\gamma$  with pressure is independent from the history of the surface in the discharge, unlike the modification of the Si surface due to sputtering.

In conclusion, the nature of a surface exposed to a discharge affects the concentration gradients and the decay rates of atomic hydrogen close to the surface in a way characteristic of

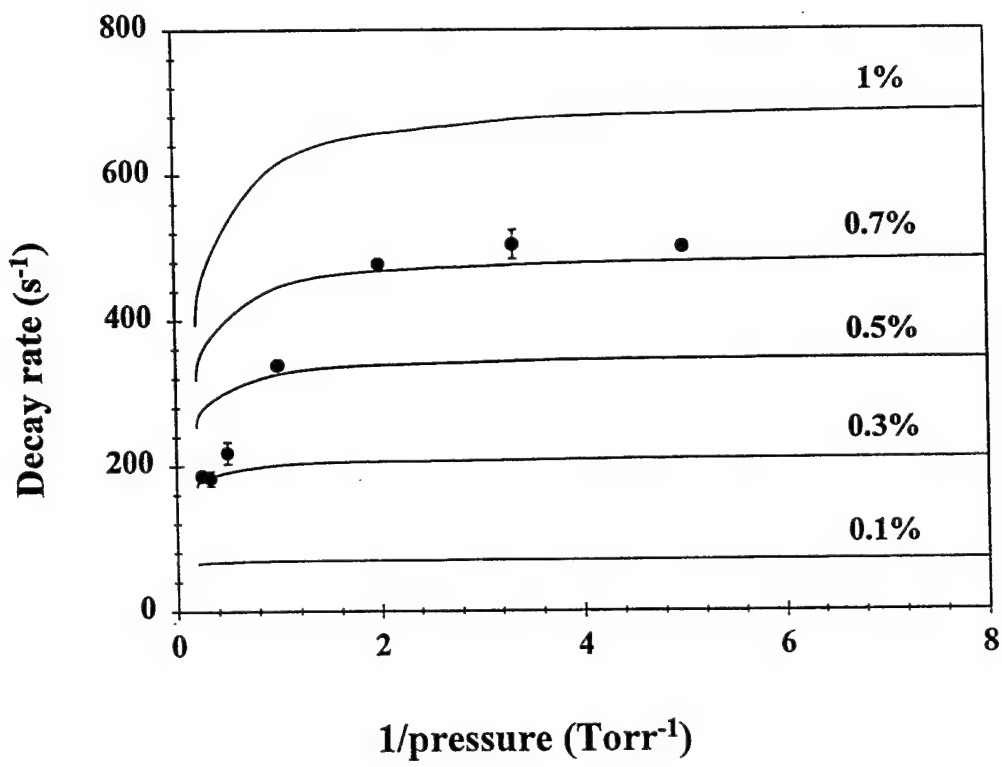


Figure 13. Variation of the decay rate (and the loss coefficient) of H atoms over an Al surface as a function of the discharge pressure.

---

the material. This fact allows the loss coefficients for H atoms on these surfaces to be determined. Finally, the removal rate of reactive atoms by a surface was found to depend on mechanisms such as sputtering and ion bombardment, that often alter the surface characteristics in energetic plasma environments.

### 3. O atom TALIF diagnostic in plasmas

The important role that O atoms play in the striping of polymers<sup>40</sup> and the anisotropic etching of SiO<sub>2</sub> in CF<sub>4</sub>/O<sub>2</sub> plasmas<sup>41,42</sup> has dictated the extensive use of optical diagnostics in recent years, for direct or indirect detection of their ground state population. Optical emission spectroscopy<sup>43</sup> has been used to monitor relative variations of atomic oxygen concentrations in etching plasmas, while the need for quantitative measurements of the ground state concentrations has led to the use of actinometric optical emission (AOE). Since actinometry is not always reliable as a means to monitor ground state concentrations under certain discharge conditions,<sup>44</sup> time-resolved actinometry<sup>45</sup> and two-photon laser-induced fluorescence<sup>46,47,48</sup> have been used to investigate the parameter space of applicability of AOE spectroscopy. Some works also focused on the kinetics of O atoms,<sup>48</sup> an understanding of which would allow optimization of, and a better control over, microelectronics fabrication conditions.

In this section, we describe TALIF studies used to determine absolute O-atom concentrations, their spatial distribution indicative of the production regions, and their temporal profiles that depend on the discharge parameters. Specifically, the absolute concentration measurements were achieved by an *in situ* standard titration technique with NO<sub>2</sub>, performed in a flow tube that is appropriately imbedded in our RF reactor to prevent any errors due to changes in optical detection geometry. The spatial distribution, before or after the establishment of steady-state concentrations, was found to be relatively uniform across the interelectrode space in the range of pressures studied (0.1-3 Torr). Finally, the heterogeneous losses of O atoms in the RF reactor were studied by means of a 100% rectangular wave-modulated discharge, and they were expressed in terms of pressure and power dependent loss coefficients for O atoms on the

electrode surfaces.

#### A. Experiment

The parallel plate RF reactor where O atoms are produced is very similar to the one for H atoms while the detection technique we utilized has been successfully employed in the past for the detection of atomic oxygen<sup>46,47,48,49</sup>. A brief description of the experiment layout follows below.

The RF reactor was again a six-way pyrex vessel with stainless-steel electrodes, 55 cm in diameter, fitted onto the vertical ports at a separation of 18 mm. The top electrode was driven by a power supply operating at 10 MHz with the bottom electrode connected to ground. The 226-nm light, in resonance with the two-photon transition from the ground  $2p^4\ ^3P$  state to the  $3p^3\ ^3P$  state, was produced by mixing the fundamental of the Nd/YAG laser at 1064 nm with the second harmonic of the output of the dye laser at 572 nm. The probe beam was directed into the cell parallel to the electrode surface, and was focused to a spot inside the plasma reactor by means of 15 cm quartz lens. The fluorescence of the upper state to the  $3s^3\ ^3S$  which results in 844.6 nm emission was detected at right angles with respect to the excitation beam, through an interference filter centered around 845 nm, by a photomultiplier tube (PMT).

Spatially resolved concentration profiles were obtained by moving the reactor with respect to the fixed excitation/detection geometry so that concentrations can be probed across the interelectrode space. Temporal profiles were obtained by means of a repetitive pulsed discharge, accomplished by a 100% amplitude modulation of the output of the signal generator that drove the power amplifier, with a computer adjusted delay between the onset of the discharge and the firing of the laser.

to signals from known concentrations of O atoms produced in a flow tube by a microwave discharge. The comparison of TALIF signals from the RF and microwave reactors is possible since O atoms were excited and detected with the same geometric arrangement. This was achieved by mounting the flow tube with the microwave source on the upper vertical port of the reactor, in place of the top electrode. A detailed description of the titration apparatus and typical procedures has been given in previous work.<sup>50</sup> O atoms were produced by flowing a mixture of O<sub>2</sub>/Ar through a microwave cavity and they were detected downstream. The concentration of the O atoms at the probe region can be determined by means of an *in situ* titration technique. O atoms were mixed with NO<sub>2</sub> at a region about 2 cm above the detection point and they reacted according to



Due to the reaction of O atoms with NO<sub>2</sub>, the TALIF signal decreases linearly upon addition of NO<sub>2</sub> in the reaction region, as shown in the inset of Fig. 14. By measuring the NO<sub>2</sub> concentration at the end-point of the titration (x-intercept), we determined the concentration of O atoms corresponding to the initial TALIF intensity (y-intercept).

## B. Results and Discussion

### 1. Concentration measurements in space and time

In Fig. 14, we show a calibration curve constructed by repeating the titration experiment for various O-atom concentrations produced in the flow tube. The curve exhibits a linear dependence of the TALIF signal on the O-atom concentration, a fact that indicates that a fluorescence-depleting mechanism such as stimulated emission could not have an appreciable

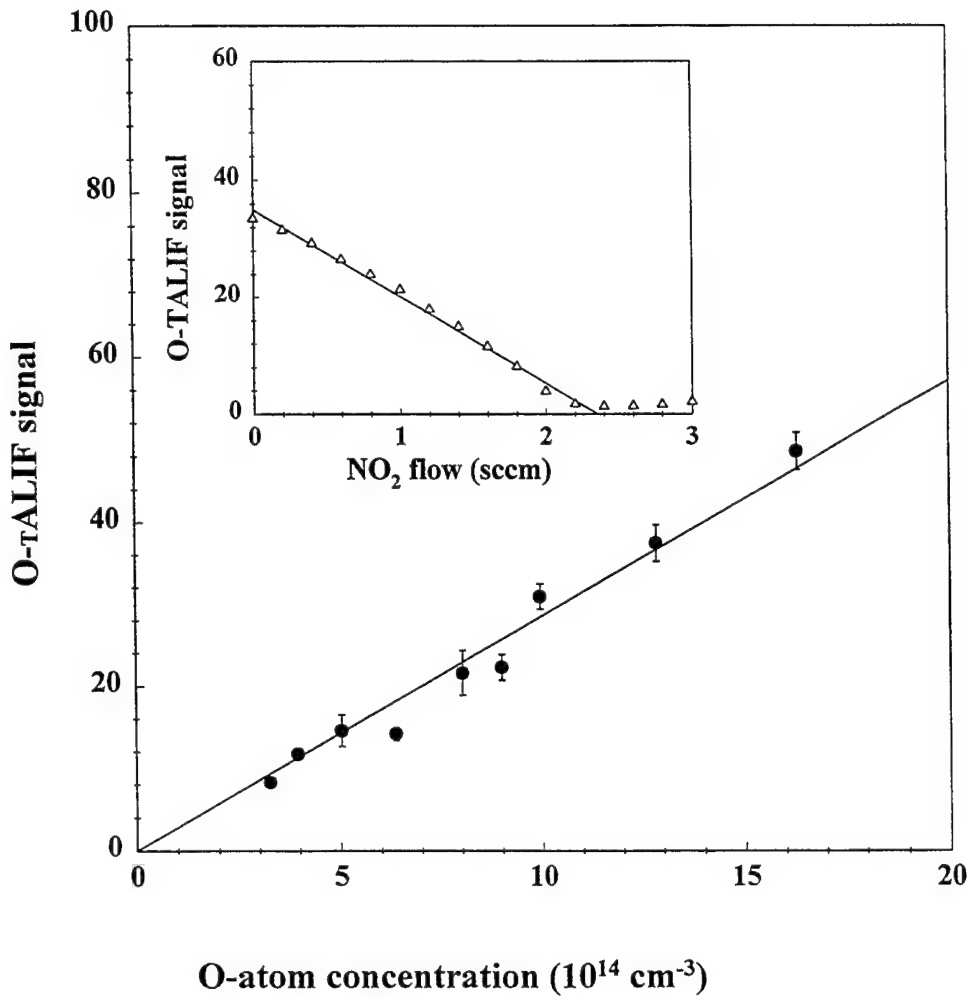


Figure 14. Calibration curve for O-TALIF intensities. Each data point is determined by titrating *in situ* an O-TALIF signal with a known concentration of NO<sub>2</sub> (inset)

effect on the TALIF diagnostic, at least up to concentrations ( $2 \times 10^{15} \text{ cm}^{-3}$ ) corresponding to the maximum level of signal calibrated in this experiment. This calibration curve is used to convert TALIF signals (obtained under identical detection conditions as the signals on the curve) to absolute concentrations.

Since O-atom concentrations were measured over a wide range of pressures (0.1-3 Torr) of the discharge, TALIF signals were corrected for the quenching of the upper state as pressure increased. The quantum yield of the transition as a function of pressure of various quencher gases has been measured by Bittner *et al.*,<sup>51</sup> and these results were used here to obtain absolute concentrations in a pure oxygen discharge. Concentrations in the range of  $0.4-3 \times 10^{15} \text{ cm}^{-3}$  were measured in 0.1-3 Torr  $\text{O}_2$  discharges, at powers 20-100 W. These concentrations correspond to conversion efficiencies of 1.6-2.4 % from molecular oxygen, in agreement with previous investigations limited to low pressures (< 100 mTorr).<sup>48,49</sup>

Spatial profiles obtained in a 3 Torr  $\text{O}_2$  discharge are shown in Fig. 15. Both traces obtained in a pulsed discharge, at time  $t=0.25 \text{ ms}$  and  $t=1.8 \text{ ms}$ , respectively, after initial turn-on, exhibit the same qualitative characteristics; they are mostly uniform throughout the interelectrode space with small concentration gradients near the electrode (stainless-steel) surfaces. The uniformity of the profile taken very early in the discharge ( $t=0.25 \text{ ms}$ ) indicates a rather uniform production of O atoms in the interelectrode space (in contrast to H atom production which was found to occur predominantly near the plasma sheaths<sup>50</sup>), while the small concentration gradients close to the electrode surfaces indicate relatively small losses for O atoms on the electrode surfaces.

A typical temporal profile, obtained by means of a pulsed discharge at 3 Torr, is shown in

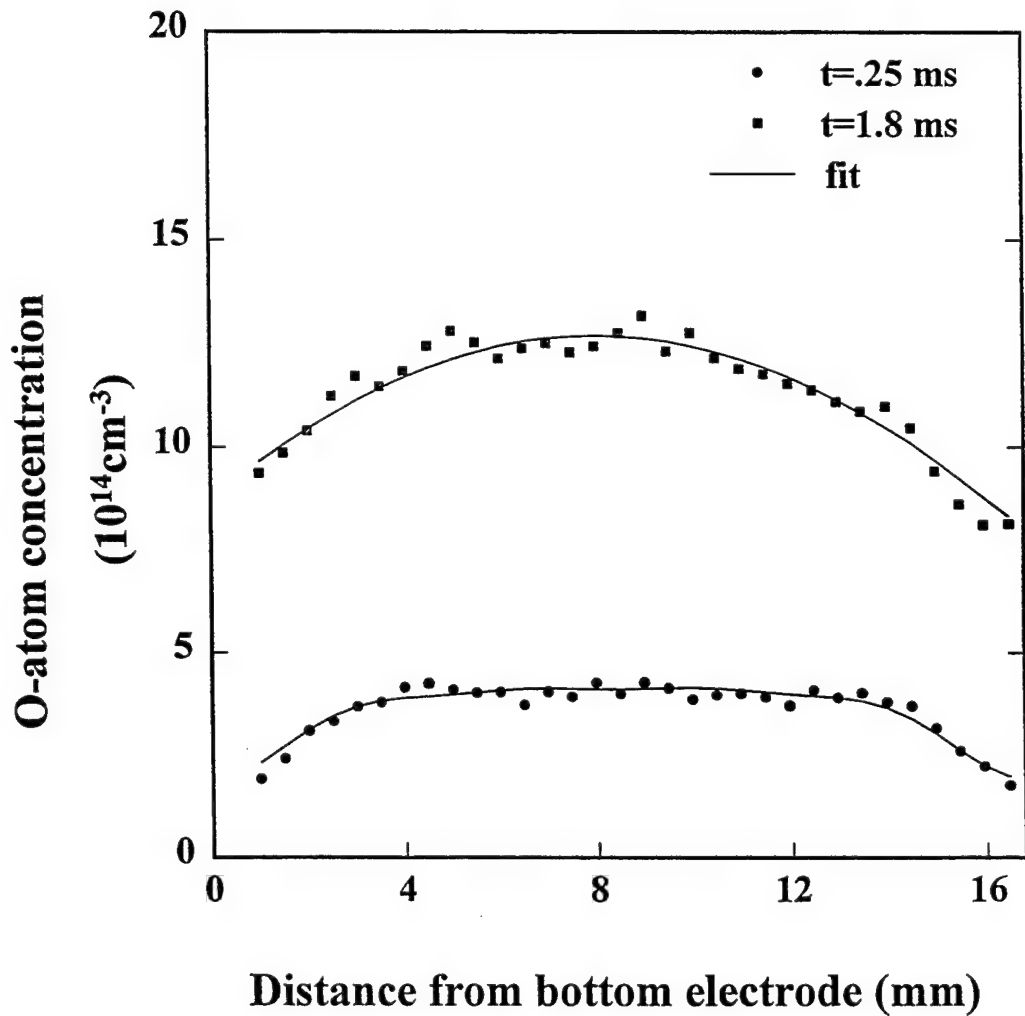


Figure 15. Spatial profiles of O-atom concentration in a 3 Torr discharge, after initial discharge turn-on ( $t=0.25 \text{ ms}$ ,  $t=1.8 \text{ ms}$ ).

Fig. 16. Semilogarithmic plots of the O-concentration versus time after discharge turn-off exhibit linear behavior, characteristic of a first order mechanism responsible for the decay of the atomic oxygen, with a rate of  $86 \text{ s}^{-1}$ . This is consistent with the fact that the second-order in O atoms, homogeneous recombination (three-body) process,



characterized by a low rate coefficient<sup>48</sup>  $k_2 = 7 \times 10^{-33} \text{ cm}^6 \text{s}^{-1}$ , results in a low rate even at the highest pressure of 3 Torr ( $\sim 5 \text{ s}^{-1}$ ). Thus, as in the case of hydrogen atoms evolving in a discharge,<sup>52</sup> heterogeneous loss of O atoms on the surface material is the dominant loss mechanism that can explain the observed single-exponential decay.

## 2. Model

We now wish to modify the model used in the previous section for H atoms, to describe the spatial and temporal evolution of O atoms at all times except immediately after discharge initiation (see part B.3 for a discussion of the behavior during this time). We will assume for simplicity that O atoms are produced at a rate  $R_0(x)$  in the interelectrode space, and they are removed by heterogeneous processes on the surfaces. The surface loss of O atoms is expressed in terms of the loss coefficients  $\gamma_1, \gamma_2$  of the two electrode surfaces, and it is embodied in the boundary conditions.<sup>52</sup> Therefore, we solve the following diffusion equation for the mass transfer of O atoms in the interelectrode space:

$$\frac{\partial p}{\partial t} = D \frac{\partial^2 p}{\partial x^2} + R_0(x) \quad (13)$$

We tried a variety of functions to express the production rate for O atoms: two point sources symmetrically located at the sheaths of the discharge<sup>52</sup> or a uniform production throughout the interelectrode space. The appropriate function for  $R_0(x)$  was chosen by producing the best fits to

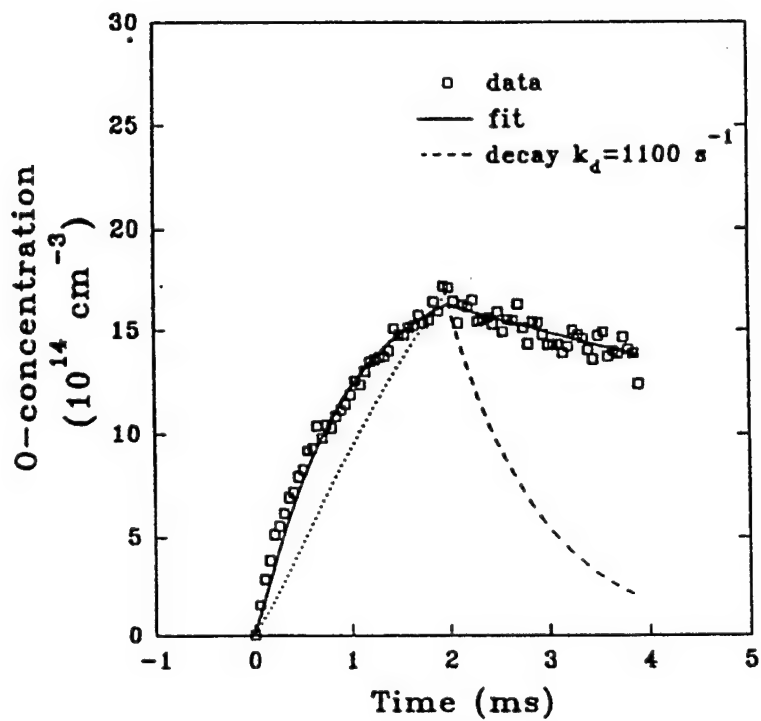


Figure 16. Temporal profile in a 3 Torr pulsed discharge. The decay of the atomic oxygen ( $t > 2$  ms) is much slower than the rise ( $0 < t < 2$  ms) as shown by the dotted curve shown in the afterglow obtained with a decay rate equal to that in the rise. The data in the decay are fit to Eq. (11) with  $\gamma = 0.6\%$ , while even a loss coefficient as high as 100% cannot accommodate the high rate constant for the rise of the O-concentration (dotted line)

the spatial profile at  $t=0.25$  ms, since the spatial profiles at longer times or at steady state conditions are not sensitive to the spatial dependence of  $R_0$ . The best results were obtained for a uniform production of O atoms at a region in the interelectrode gap extended from a distance  $x_0$  from either electrode surface. It is convenient for the analytical solution of Eq. (13) to assume that the production rate  $R_0(x)$  results from a continuous distribution of sources of the same production rate  $\rho_0$ , each located at a distance  $x'$  from the electrode surface, with  $x'$  ranging from  $x_0$  (the edge of the production region) to  $a-x_0$ . We can then conveniently express such a production term as an integral

$$R_0 = \rho_0 \int \delta(x-x') dx' \quad (14)$$

over the interelectrode range  $[x_0, a-x_0]$ , due to the symmetry of the problem.

The solution of Eq. (13) has the general form

$$\rho(x,t) = \sum \rho_n(x) \{1 - \exp[-(D\lambda_n^2 t)]\} \quad (15)$$

where

$$\rho_n(x,t) = [2\rho_0/(aD\lambda_n^3)] \cos(\lambda_n x - \delta_n) [-\sin(\lambda_n x_0 - \delta_n) + \sin(\lambda_n(a-x_0) - \delta_n)] \quad (16)$$

$D$  is the diffusion coefficient,  $v$  is the mean thermal velocity of O atoms, and  $\lambda_n$ ,  $\delta_n$  are given by Eqs. (17) and (18) respectively,

$$\lambda_n a = \tan^{-1}[\gamma_1 v / (4(1-\gamma_1)D\lambda_n)] + \tan^{-1}[\gamma_2 v / (4(1-\gamma_2)D\lambda_n)] + n\pi \quad (17)$$

$$\delta_n = \tan^{-1}[\gamma_1 v / (4(1-\gamma_1)D\lambda_n)] \quad (18)$$

Eqs. (15)-(18) are used to fit the experimental data with parameters  $x_0$ ,  $\gamma_1$ ,  $\gamma_2$ , and  $\rho_0$ . The value used for the diffusion coefficient for O was  $80 \text{ cm}^2/\text{s}$  at 3 Torr and at room temperature.<sup>53</sup> The fit curve on the spatial distribution at  $t=0.25 \text{ ms}$  (Fig. 15) was obtained for O atoms uniformly produced in the interelectrode region extended from  $x_0=1.2 \text{ mm}$  from each electrode surface and destroyed on surfaces (SS) with a loss coefficient  $\gamma=(0.5 \pm 0.1)\%$ . For the rest of the fit curves that will be shown in this work,  $x_0$  is used as a (determined) constant.

The solution of Eq. (13) with the production rate  $R_0=0$  in the afterglow of a discharge ( $t>t_0$ ) is given by

$$\rho(x,t) = \sum \rho_n(x) \{1 - \exp(-D\lambda_n^2 t_0)\} \exp[-D\lambda_n^2 (t-t_0)] \quad n=1,2,3,\dots \quad (19)$$

This equation is used to determine the loss coefficient of O atoms on the SS surfaces, from the temporal decay rates measured in the discharge afterglow. From the temporal profile of Fig. 16, a loss coefficient  $\gamma=0.6 \%$  was determined, while temporal profiles taken at different pressure and power indicated a dependence of  $\gamma$  on the discharge parameters. Specifically, comparison of the decay rates in Fig. 17 shows that while  $\gamma=0.6\%$  in a 3 Torr/50 W discharge (17a), the loss coefficient increases to  $\gamma=1.3\%$  in a 0.1 Torr/50 W discharge (17b). Similarly, in Fig. 18, the value of the loss coefficient  $\gamma$  increases from 0.75% in a 0.2 Torr/55 W discharge (18b), to  $\gamma=1.3\%$  in a 0.2 Torr/90 W discharge (18a). The increase of the loss coefficient with decreasing pressure and increasing power is consistent with enhancement of ion bombardment, that is

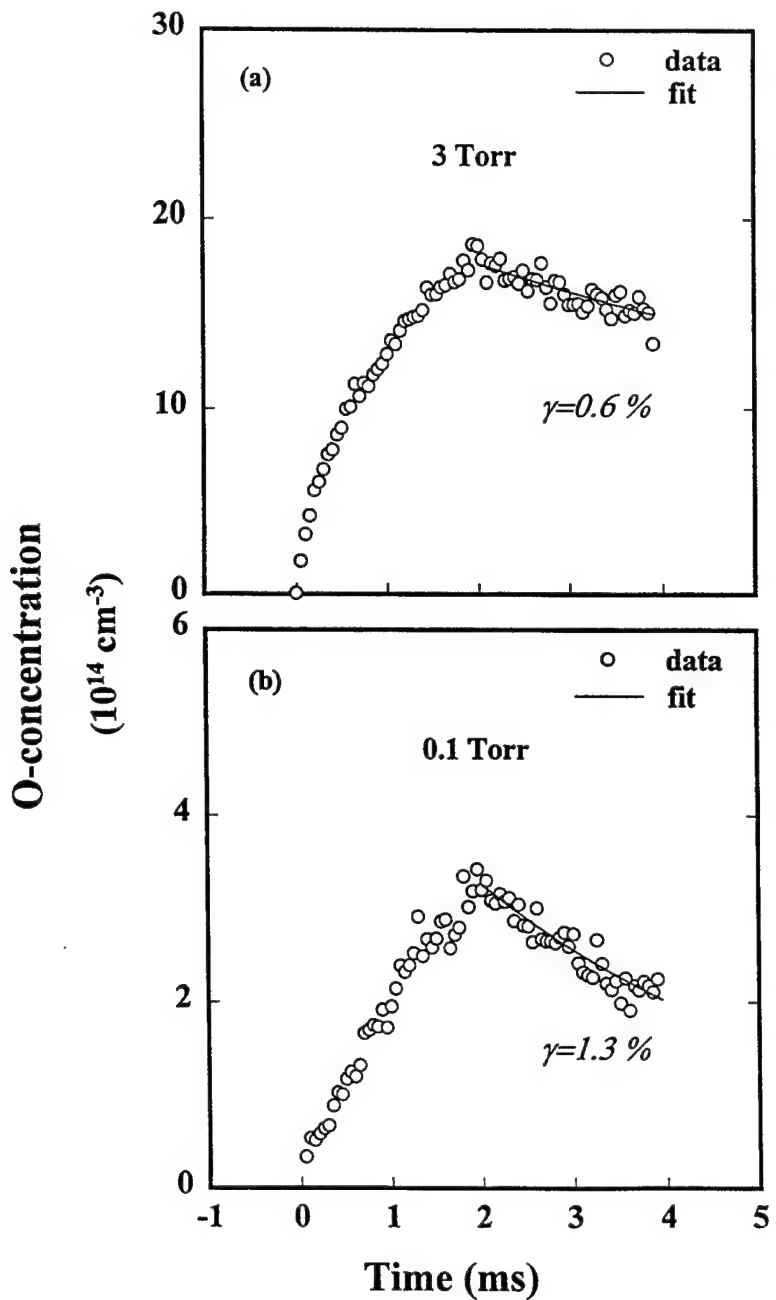


Figure 17. Dependence of temporal profiles on the discharge pressure. (a) The data in a 3 Torr/50 W discharge were fit with  $\gamma=0.6\%$  and  $R_1/R_0=8$ . (b) The data in a 0.1 Torr/50 W discharge were fit with  $\gamma=1.3\%$  and  $R_1/R_0=2$

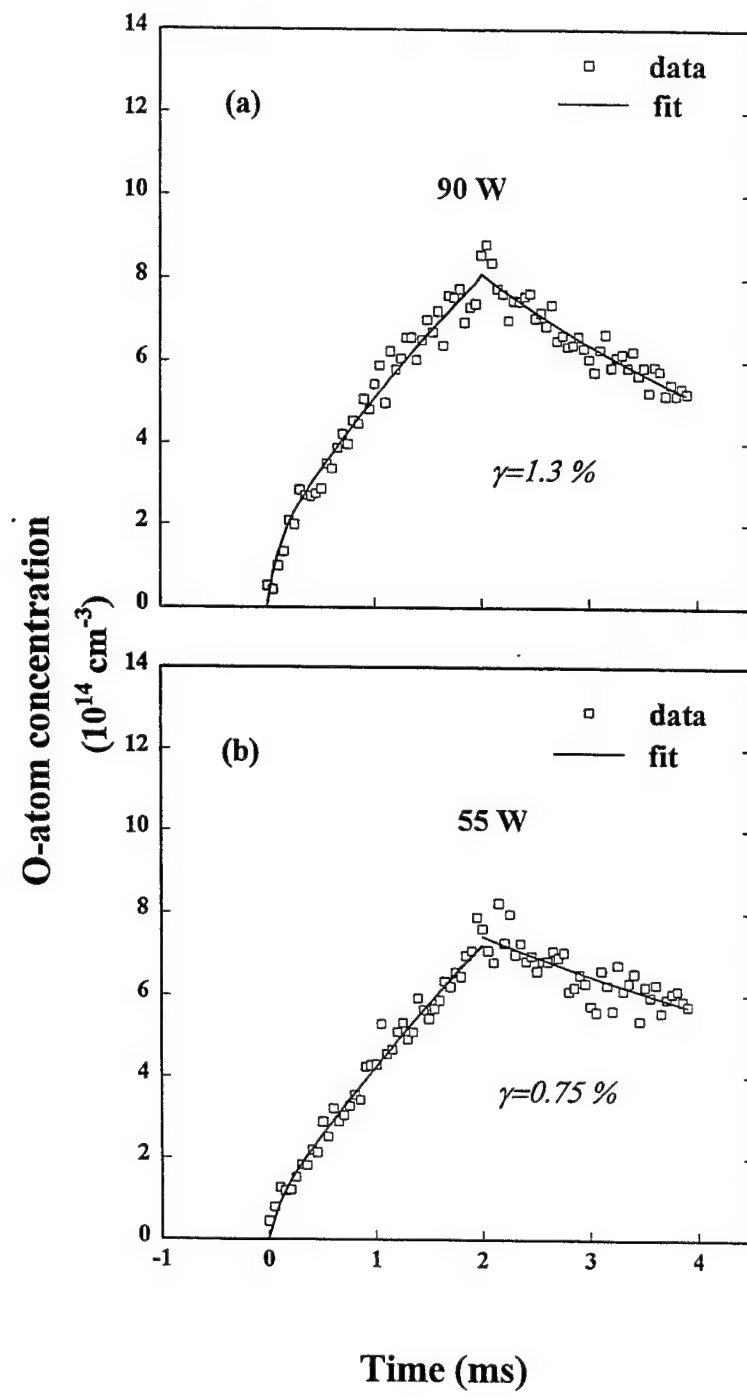


Figure 18. Dependence of temporal profiles on the discharge power. (a) The data in a 90 W/0.2 Torr discharge were fit with  $\gamma=1.3\%$  and  $R_1/R_0=3$ . (b) The data in a 55 W/0.2 Torr discharge were fit with  $\gamma=0.75\%$  and  $R_1/R_0=2$

expected at low pressures where ions are more energetic (they do not lose energy in collisions) and at high powers where the ion density increases.

Fig. 19 describes in detail the increase of the decay rate (in the discharge afterglow) with discharge power, in a 0.2 Torr discharge. The decay rate increases linearly with power, possibly since the charged particle density increases linearly with discharge power. The corresponding increase of the loss coefficient for O atoms on an SS surface is also shown in Fig. 19. Interestingly, a corresponding increase of  $\gamma$  in this power range was not observed for H atoms on a SS surface.<sup>52</sup> A mechanism possibly responsible for the increase in  $\gamma$  at higher powers is enhanced ion bombardment which may create more sites for O atoms on the surface, however, this mechanism apparently does not alter significantly the loss rate for the more mobile H atoms for which a SS surface appears nearly saturated with sinks.

The pressure dependence of the O atom loss coefficient on an SS surface is demonstrated in detail by means of both spatial and temporal profiles, as in Figs. 20 and 21. Fig. 20 shows spatial distributions of O atoms obtained under steady-state discharge conditions at pressures ranging from 3 Torr down to 0.25 Torr. We obtained best fits by increasing the loss coefficient of the SS surface from 0.3 % to 1.1 % for the above noted reduction in pressure. In the same pressure range, the production rate  $p_0$  decreased by a factor of ~26 for a decrease in pressure by a factor of 12, indicative of a relatively constant degree of dissociation with pressure (estimated to ~2 %). Fig. 21 shows the variation of the decay rates of O, determined by temporal profiles, as the pressure decreases from 3 to 0.1 Torr. The solid lines represent the predictions of the diffusion model for the decay rates of O atoms on surfaces with a loss coefficient  $\gamma$  over the investigated pressure range. We found that the loss coefficient for O atoms on the SS surface

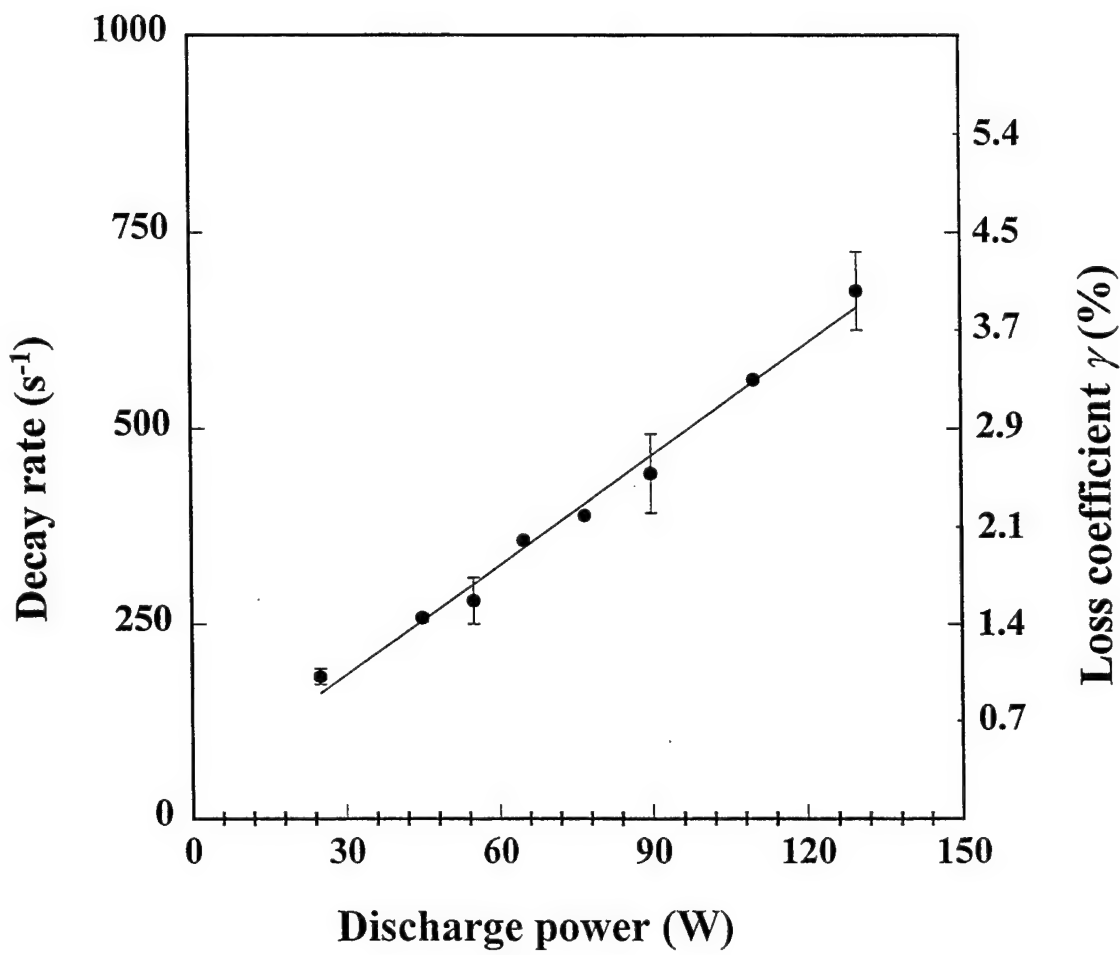


Figure 19. Variation of the decay rates in a pulsed discharge as a function of the discharge power. The observed increase of the decay rate with power corresponds to an increase of the loss coefficient of O atoms on an SS surface from 0.8 to 4.0%.

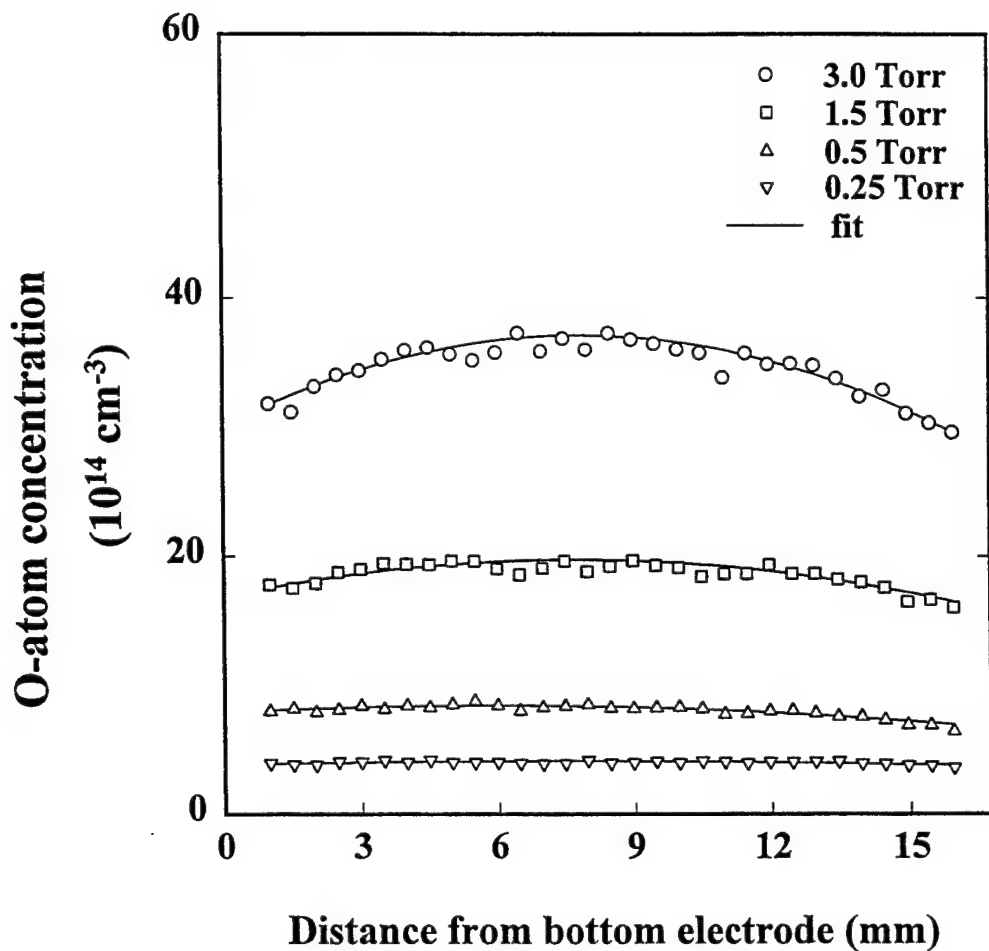


Figure 20. Spatial profiles for O atoms as a function of pressure. Fits to the data indicate a reduction of the loss coefficient of the SS surface from 1.1% to 0.3% as pressure increases from 0.25 to 3 Torr.

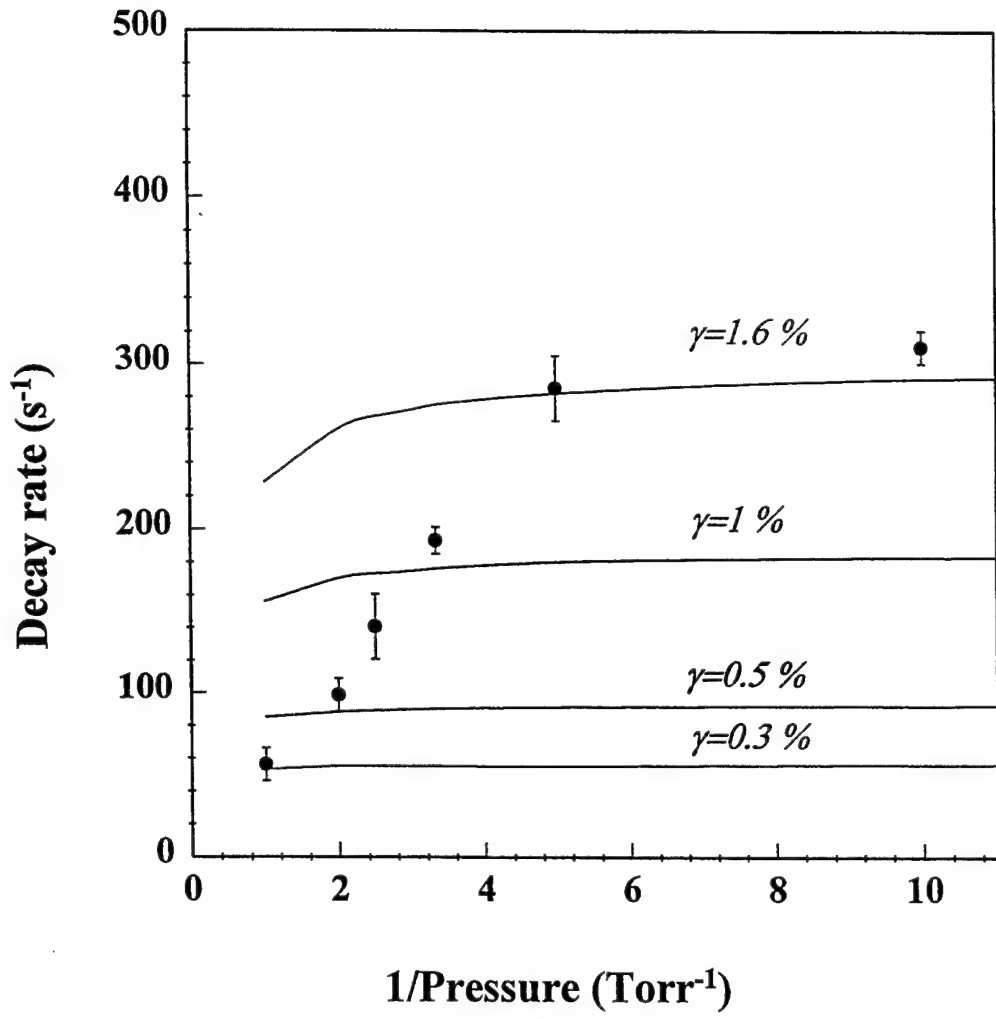


Figure 21. Decay rates for O-atoms in the afterglow of a pulsed discharge as a function of inverse pressure. The solid curves are the predictions of the diffusion model (discussed in the text) for the variation of the decay rate with pressure, and indicate an increase of the loss coefficient  $\gamma$  from 0.3 % to 1.6 % as the pressure decreases from 1 to 0.1 Torr

increases from 0.4% to 1.6% as pressure decreases from 3 to 0.1 Torr. As we discussed previously, a possible explanation for the observed effect is that enhanced ion bombardment (at lower pressures where the sheaths get less collisional) may create more sites available for O atoms to stick or recombine.

### 3. Early discharge behavior

Comparison of the temporal profiles in the rise and the afterglow of a discharge has revealed another interesting aspect of the oxygen discharges we studied. If the rise ( $t < 2$  ms) of the population in Fig. 16 was simulated -at a first approximation- by a single exponential, a rate constant  $k_r = 1100 \text{ s}^{-1}$  would be necessary, while a much smaller rate  $k_d = 86 \text{ s}^{-1}$  was necessary for the decay ( $2\text{ms} < t < 4\text{ms}$ ). The dashed line in the afterglow represents a decay at a rate as fast as that of the rise. Therefore, there exists an additional mechanism during the discharge that is responsible for the fast rise of the atomic population.

We can exclude gas-phase reactions between O atoms and other molecules (present in an oxygen discharge), such as



and



that could lead to single-exponential decays (if the concentrations of  $\text{O}_2$  or  $\text{O}_3$  were considered as constant during the decay of O), since first they result in decay rates (calculated from the rate constants of the corresponding reactions<sup>54</sup>) much smaller than those we measured experimentally, and second, these would occur both in the afterglow and during the discharge.

Thus, charged particles (present only during the discharge) should play an important role

in it. We should examine various possibilities for processes involving ions or electrons. First, ion-molecule reactions involving O atoms were excluded since, as three body processes, they have a small probability to occur. Second, we investigated the possibility that electron collisions might remove O atoms either from their ground state or from the laser-excited state. Ground-state oxygen atoms are known to be directly excited by electron collisions and cross-sections for these excitations have been calculated.<sup>47,55</sup> Actually, the actinometric techniques for detection of atomic species by optical emission are based on this process, however the question is whether the effect of direct electron excitation of ground-level atoms is significant enough to result in detectable loss of O atoms in the discharge. If we assume that the rate we measure during the discharge is totally due to direct electron excitation of ground-state atoms, then we determine a cross-section for this process that is at least two orders of magnitude higher than the theoretical calculations<sup>54</sup> even for low-energy electrons. On the other hand, if laser-excited O atoms were quenched by electron collisions during the discharge, this would result in a sharp increase of the LIF signal apparent immediately after the turn-off of the discharge, as charged species that are responsible for the quenching die-off rapidly, thus increasing the yield of the fluorescence. However, such a jump in the LIF signal coincident with the discharge turn-off was not observed in our experiments. We should therefore turn to some other mechanism to explain this observation.

Specifically in Fig. 16, the rise rate cannot be attributed to losses of O atoms on surfaces, since even a loss coefficient  $\gamma$  as high as 100% could not accommodate an observed rate of the order of  $1100 \text{ s}^{-1}$  (as shown with the dotted line). So, one has to modify the assumptions of the previous model in order to simulate the data immediately after discharge ignition. More specifically, if one assumes that the production rate for O atoms decreases as the discharge

evolves towards equilibrium, then the behavior of the rise of the population could be explained qualitatively. And since no appreciable dissociation was observed in the investigated discharges, the slowing down of the production rate could not be attributed to the depletion of the parent molecule concentration ( $O_2$  in this case). It is evident that one should seek the variation of electron density distribution as a likely candidate. Independent studies in oxygen discharges<sup>45</sup> have shown that although the electron temperature equilibrates rather rapidly ( $\sim \mu s$ ), the electron density reaches equilibrium only after 100-200  $\mu s$ , *i.e.* a time scale roughly comparable with that of our experiments (2 ms).

We have to incorporate this hypothesis (of a time-dependent production rate for atoms in the discharge) in the model. For simplicity, we could include the spatial boundary conditions and the mass transport due to diffusion in a first-order loss term for the atomic concentration  $\rho(t)$  of the form  $-k_d\rho(t)$ , since we are interested in simulating the temporal behavior of the concentration measured at a point in space. Then the time-varying concentration should satisfy the equation

$$d\rho(t)/dt = R(t) - k_d \rho(t) \quad (22)$$

where  $R(t)$  is the time-dependent production rate. It is appropriate for the production rate (that is large at small values of  $t$  and evolves to a constant value as time advances) to be approximated by the following function:

$$R(t) = R_0 + R_1 \exp(-k't) \quad (23)$$

where  $R_0$  is the steady-state production rate, and  $R_1$  is the amplitude of the additional production rate that is exponentially decaying at a rate determined by the electronic density equilibrium time ( $k' = 1/\tau \sim 10^4 \text{ s}^{-1}$ ). The solution of Eq. (22) is given by

$$\rho(t) = R_0 [1 - \exp(-k_d t)] / k_d + R_1 [\exp(-k_d t) - \exp(-k't)] / (k' - k_d) \quad (24)$$

The rise of the temporal profiles shown in Figs. 17, 18, taken under various conditions of pressure and discharge power, was fit to Eq. (24) with parameters  $R_0$  and  $R_1$  ( $k' = 10^4 \text{ s}^{-1}$  was used,<sup>45</sup> and  $k_d = D\lambda_1^2$  was determined by temporal profiles in the discharge afterglow). Obviously, the fit clearly reproduces the data. In addition, we found that, at conditions of high pressure and power, a higher value for the ratio of the production rates  $R_1/R_0$  was necessary than that at low pressure and power. The variation of the ratio  $R_1/R_0$  with pressure and power is expected due to the dependence of the production rates on electron density and  $\text{O}_2$  concentration.

We conclude this section with the following observation. The solution in Eq. (24) for a time-dependent production rate converges at large values of  $t$  to the temporal behavior of Eq. (19) derived for a time-independent production rate, thus one should expect the spatial distributions for O atoms at steady-state ( $t \rightarrow \infty$ , Fig. 20) not to be sensitive to details concerning the production of the atoms during the first few 100's  $\mu\text{s}$  after initialization of the discharge. This is the reason that the fits in Fig. 20 were obtained with a time-independent production rate for O atoms.

#### 4. Etching plasmas

Because of the technological importance of O atoms in etching plasmas containing fluorine atoms, we measured the decay of O atoms in the presence of fluorine atoms in the discharge. We used a mixture of  $\text{O}_2/\text{CF}_4$  at a constant total pressure of 0.2 Torr, and at a total power of 110 W. We varied slowly the composition of the mixture by adding  $\text{CF}_4$  to  $\text{O}_2$  and we measured the decay rates, as shown in Fig. 22. We observed a significant decrease in the decay rate by about 50% for a small addition ( $\approx 5\%$ ) of  $\text{CF}_4$  in the discharge which should not alter the characteristics of the discharge and the diffusion of O atoms, it could however result in

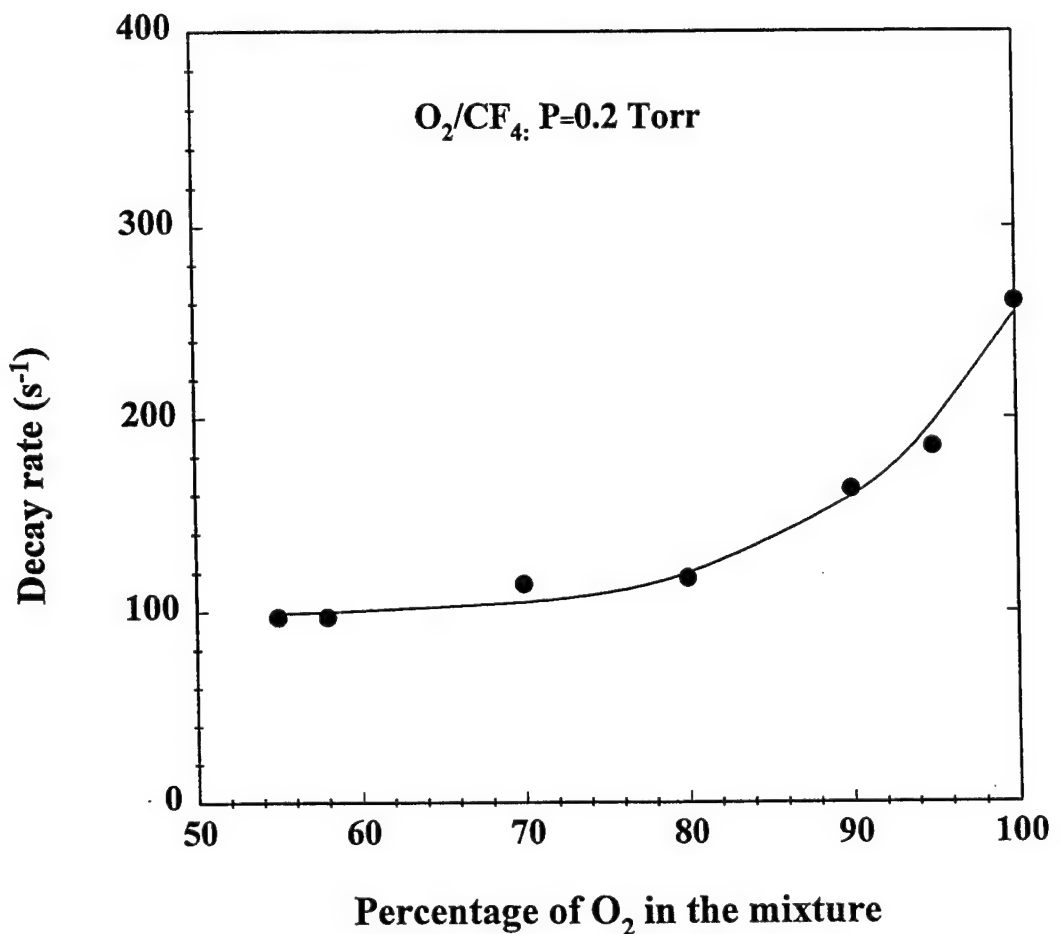


Figure 22. Variation of the decay rate of O atoms upon addition of  $\text{CF}_4$  in a  $\text{O}_2$  discharge. The decay rates were measured in the afterglow of a pulsed  $\text{CF}_4/\text{O}_2$  discharge kept at a constant total pressure (0.2 Torr). The solid curve is a guide to the eye.

competition between O and F atoms to occupy available surface sites. This competition between O and F atoms results in a reduction of the O atom loss coefficient from 1.45 % to 1.01 % upon 5 % addition of CF<sub>4</sub> in the 0.2 Torr mixture. A more severe effect under addition of fluorinated gases in O<sub>2</sub> discharges had been previously observed by other investigators in CF<sub>4</sub> and SF<sub>6</sub> discharges.<sup>45,49</sup> We believe that the discharge power at which the experiment is performed affects critically its outcome; when we performed this experiment at a smaller power (55 W) no effect of CF<sub>4</sub> addition on the O-atom loss coefficient could be detected, possibly due to insufficient dissociation of CF<sub>4</sub> that provides fluorine atoms in the discharge.

Finally, we studied the effect of O atoms in a discharge loaded with a photoresist material. We measured the decay rate of O atoms on the photoresist surface by means of a pulsed discharge (110 W, 0.1 Torr) initially and after exposing the material under severe plasma conditions: a high power and low pressure continuous discharge. We observed that, although the material was removed from the surface (evident by the discoloration of the surface on which the photoresist was applied), the decay rate of the O atoms on the surface did not change significantly (a decrease by only ~10 % was observed). A similar behavior had been observed by Booth et al.<sup>45</sup> who reached the conclusion that O atoms are lost at the same rate on both surfaces. However, when we measured the decay rates in a 55-W pulsed discharge, a reduction in  $\gamma$  by about 20-30 % was observed. We believe this is due to the fact that the small decrease in  $\gamma$  after the photoresist stripping from the surface can be easily obscured by enhanced ion bombardment in high-power discharges.

### C. Conclusion

Absolute O-atom concentrations were obtained in a parallel plate RF reactor. Spatial

profiles and their evolution in time indicate a nearly uniform production/distribution of O atoms throughout the interelectrode space and small losses on the electrode surfaces. Temporal profiles in the afterglow of the discharge also determine the loss coefficient for O atoms on the electrode surface that was found to vary with the discharge conditions; it increased with decreased pressure, and linearly increased with power. In terms of the composition of the gas mixture, the loss coefficient of O atoms on the electrode surface was found to sharply decrease with a small addition of CF<sub>4</sub> in the O<sub>2</sub> discharge. The notion that the loss coefficient of atoms on a surface varies with the specific discharge conditions is very important, since it establishes the use of *in situ* diagnostics as the only reliable way to identify surface characteristics in a reactive environment.

#### 4. Effect on TALIF diagnostics of stimulated emission in O plasmas

In the preceding section, we demonstrated the capability of TALIF to measure, under certain conditions, absolute O concentrations in a reactive plasma environment. When determination of the absolute concentrations of the species by TALIF is undertaken, an understanding of all the physical mechanisms that may depopulate the laser-excited state, and under certain conditions may cause a nonlinear dependence of the LIF signal on ground state population, is necessary. Furthermore, a correction has to be made to the quantum yield of the fluorescence for every deexcitation mechanism that leads to a detectable decrease of the LIF signal. Observation of amplified stimulated emission (SE) has been reported for TALIF detection of O atoms in flames and generally is common in many two-photon excitation studies.<sup>56,57,58</sup> Knowledge of its effect on laser diagnostic techniques such as TALIF is very important for the proper employment of the technique and the correct interpretation of the results.

In TALIF of oxygen, the two-photon-excited  $2p^3P \rightarrow 3p^3P$  atomic transition is followed by fluorescence to the  $3s^3S$  level. The rapid population of the  $3p^3P$  level in conjunction with the short lifetime (1.8 ns) of the lower  $3s^3S$  level<sup>59</sup> can create population inversion between these two levels. Consequently, SE is not uncommon in this classic three-level system and it may compete with fluorescence or with multiphoton ionization<sup>60</sup> in the depletion of the excited state. Studies of the effect of SE on the quantum yield of the fluorescence seem complicated by the fact that the conditions in reactive environments (flames, combustion, discharges) that produce O atoms and hence where its SE can be detected, vary significantly. A kinetic model was developed recently by Huang and Gordon<sup>61</sup> to simulate the effect of SE on the population of the laser-excited O( $3p^3P$ ) state, although the actual atomic densities were unknown. The present work provides for

the first time a method for observing SE simultaneously with absolutely calibrated TALIF signals, to determine the O-atom population threshold for SE. We find that this threshold corresponds to a rather constant concentration of O( $2p^3P$ ) atoms (even at varying excitation laser power), above which the level of SE increases abruptly. Further, we discuss the conditions under which the influence of the SE on the fluorescence should not be neglected. Finally, we show the use of the method in interpreting TALIF signals from atomic oxygen in a parallel plate RF plasma reactor.

#### A. Experiment

Our method of determining a threshold for SE requires simultaneous observation of TALIF and SE signals with a calibration procedure for the TALIF signal. The experimental set-up is similar to that described previously. Briefly, a parallel plate RF reactor cell has been modified by attaching a flow tube on the port usually bearing one of the electrodes, to allow for the calibration procedure. The flow tube was coaxial with the outer tube carrying a mixture of O<sub>2</sub> and Ar and running through a microwave cavity. O atoms produced by the microwave discharge were flowing downstream towards the excitation/detection region. The inner tube carried NO<sub>2</sub> and had perforations at its end to provide better mixing of NO<sub>2</sub> with O atoms. The mixing took place a few centimeters above the end of the outer titration tube to facilitate a complete reaction between NO<sub>2</sub> and O, according to the reaction, NO<sub>2</sub>+O → NO+O<sub>2</sub>.<sup>62</sup> The surviving O atoms were detected by the TALIF technique. The 226-nm light, necessary to induce the 2p<sup>3</sup>P–3p<sup>3</sup>P transition, was produced by mixing the 1064-nm fundamental output of a DCR-2 Nd/YAG laser with the second harmonic of the 574-nm output of a DCR-2 dye-laser operating on a Rhodamine-590/610 dye mixture. The 226-nm laser beam (diameter ~5mm) was then focused by a quartz

lens ( $f_l = 150$  mm) at a point located 1 cm below the end of the flow tube, to excite ground state O atoms in the probe region. The subsequent fluorescence of the excited atoms at 845 nm was collected at right angles by a lens configuration on a gated EMI photomultiplier tube (through a 10-nm filter centered at 845 nm). The SE passed through an iris, which was set along the forward direction of the exciting laser beam, and was collected on a Hamamatsu R928 PMT (after passing through a band-pass filter centered at 845 nm and a second UV blocking glass). Both signals were averaged on a Tektronix DSA 601 digitizer and were measured as a function of the flow of NO<sub>2</sub> in the titration tube. The flows for each gas in the cell were measured by MKS mass-flow controllers and the total pressure was measured by a MKS 122A (10 Torr) baratron head.

## B. Results and Discussion

In Figs. 23(a)-(c), we present data from three titration experiments done under identical conditions at significantly different laser powers. For each experiment, TALIF and SE signals were measured as the flow of NO<sub>2</sub> was increased up to the end-point of the titration, noted by the x-intercept of the linear fit to the TALIF data. Since the discharge parameters were kept identical for all three experiments presented in Fig. 23, the end-points occur at essentially the same titrant gas concentration that corresponds to the same initial O-atom concentration ( $5.2 \times 10^{14}$  atoms/cm<sup>3</sup>). Notice that the SE signals increase rapidly as the NO<sub>2</sub> flow decreases (or equivalently the O-atom concentration increases) beyond a cross-over region in titrant gas concentration. We define this cross-over between the linear dependence of the SE signal on the O-atom concentration and the asymptotic approach to zero as the threshold for SE. The existence of such threshold is expected by the very nature of SE.<sup>63</sup> From Fig. 23 we calculate the

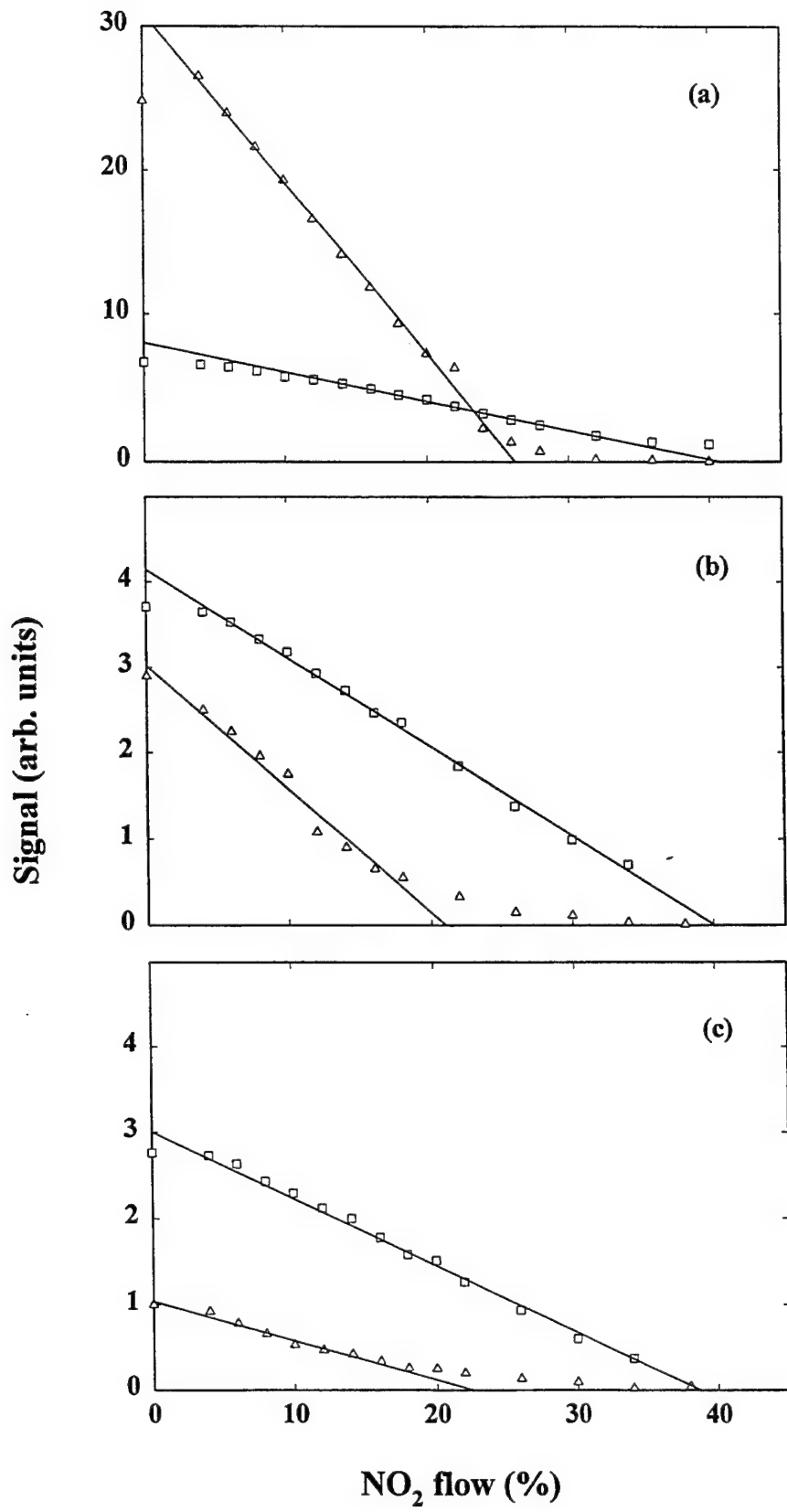


Figure 23. Titration curves for TALIF (open squares) and SE (open triangles) signals at a constant initial O-atom concentration. The laser power was (a) 185  $\mu\text{J}/\text{pulse}$ , (b) 57  $\mu\text{J}/\text{pulse}$ , and (c) 44  $\mu\text{J}/\text{pulse}$ . Every data point is an average of 128 laser pulses.

O-atom concentrations at the SE threshold to be  $N_{\text{thr}} = 2.1, 2.5$ , and  $2.9 \times 10^{14}$  atoms/cm<sup>3</sup> for 185, 57, 44 μJ/pulse, respectively.

The increase of the ground state O-atom concentration at the SE threshold with decreasing laser power is rather small. This is probably due to the fact that we approach partial saturation of the excitation transition. In such a case, even a substantial increase in laser power does not result in a significantly higher O(3<sup>3</sup>P) population, which in turn would enhance the SE signal. Fig. 24 shows that this is indeed the case. As expected, the TALIF signal as a function of laser power follows a straight line with a slope of 2 at low powers (since  $I \propto P_{\text{laser}}^2$  for a two-photon process), while it deviates from linearity at about 60 μJ/pulse and above.

We repeated the titration experiments at various O-atom concentrations, at constant excitation laser power. In Fig. 25, we show two titration curves taken at the same low laser power (44 μJ/pulse) and different O-atom concentrations ( $6.6$  and  $5.2 \times 10^{14}$  atoms/cm<sup>3</sup>, Figs. 3(a) and (b), respectively). Effort was made to keep the partial pressures of Ar and O<sub>2</sub> almost constant in the cell and as low as possible, so that the quenching of the upper excited state remains the same and does not affect significantly the TALIF (or the SE) signals. Similar to our result in Fig. 23, we find that SE takes place above a rather constant threshold value of O-atom concentration ( $2.9 \times 10^{14}$  atoms/cm<sup>3</sup>). We also observe that, although in Fig. 25(b) the TALIF signal is rather linear in O-atom concentration, in Fig. 25(a) it exhibits saturation-like characteristics at low NO<sub>2</sub> flow or equivalently at high O-atom concentrations. This is probably due to significant depopulation of the excited state by the mechanism of SE at high O-atom concentrations, that affects the TALIF signal, as we will discuss in detail below. In general, from a total of 11 experiments in which a threshold for SE was observed and in which the O-atom concentration

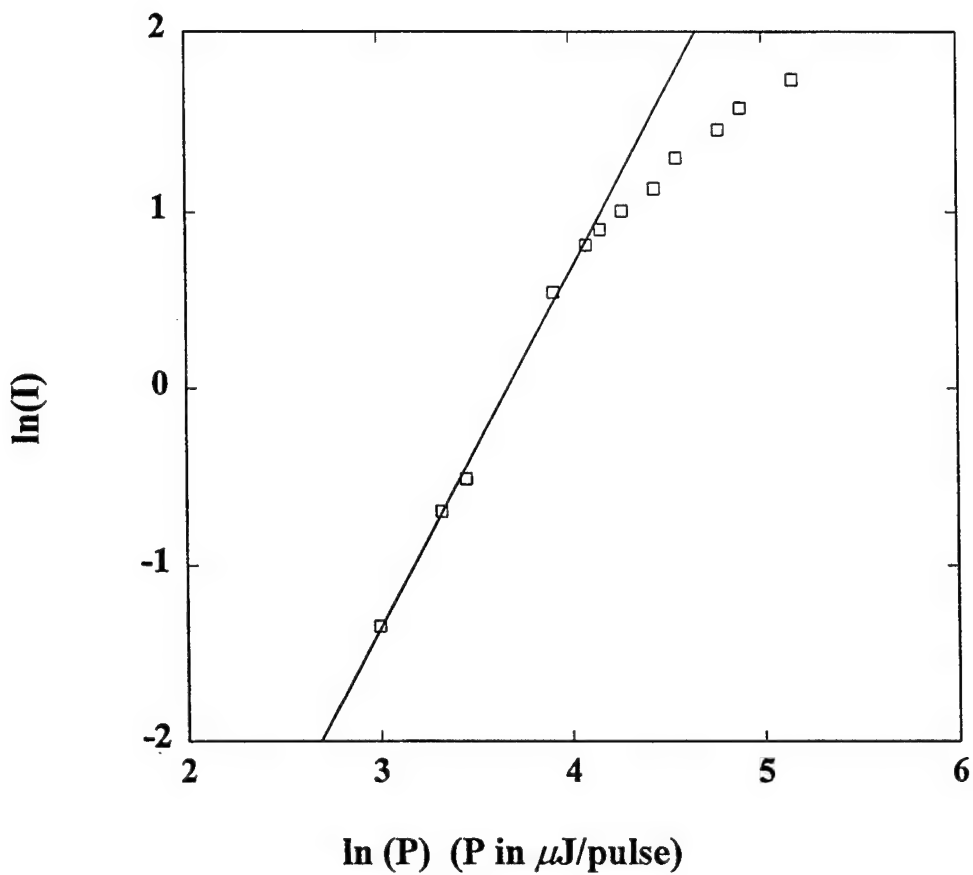


Figure 24. Intensity dependence of the TALIF signal in the flow reactor. The laser power  $P$  is measured in  $\mu\text{J}/\text{pulse}$ . The solid line is a fit to the low laser power ( $<60 \mu\text{J}/\text{pulse}$ ) data with a slope of 2.

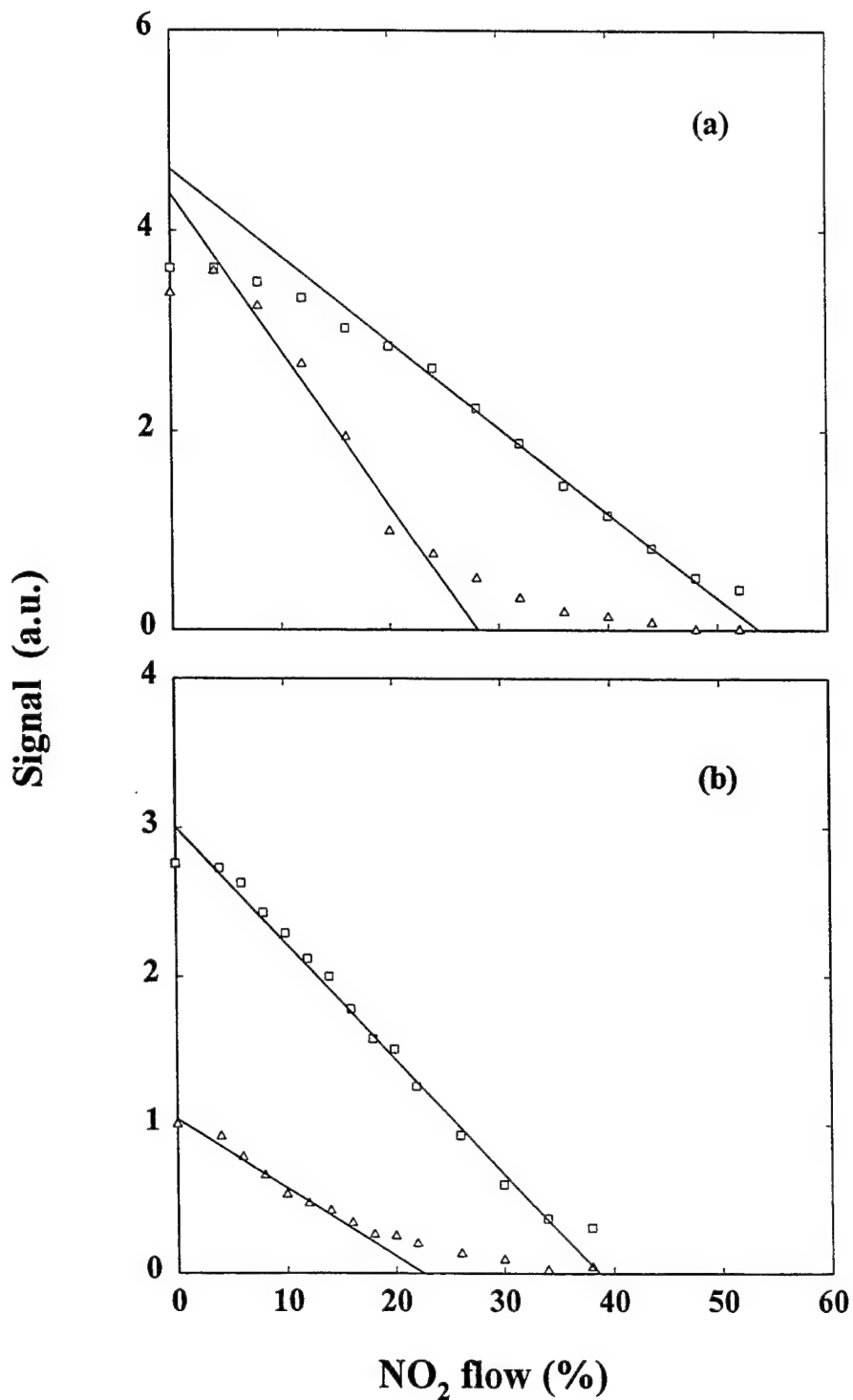


Figure 25. Titration curves taken at different initial O-atom concentrations but otherwise at identical conditions. The TALIF and SE signals are noted with open squares and triangles, respectively. The x-intercepts of the solid lines fitted to the data indicate the end-point of the titration and the threshold of SE, respectively.

was varied from 4.1 to  $7.4 \times 10^{14}$  atoms/cm<sup>3</sup> and the laser power from 0.04 to 0.51 mJ/pulse, we find that the threshold for SE occurs at a concentration  $N_{\text{thr}} = (2.5 \pm 0.4) \times 10^{14}$  atoms/cm<sup>3</sup>. This is a key result in our work.

It is useful to compare our experimentally measured threshold,  $N_{\text{thr}}$ , with theoretical expectations for this value. Recently Huang and Gordon used a coupled rate equation model to predict the threshold for SE under roughly comparable conditions. Their Fig. 2 predicts a threshold value of  $5 \times 10^{12}$  atoms/cm<sup>3</sup>, a factor of 50 smaller than our experimental value.

However, the discrepancy between theory and experiment is not so great as might be expected at first glance. Consider the rate equation<sup>61</sup> (in the absence of ionization), with laser flux,  $\Phi$ ,

$$dN_3/dt = \sigma^{(2)}\Phi^2(N_1 - N_3) - \sigma_e G c q (N_3 - N_2) - A_{32}N_3 \quad (25)$$

$N_1$ ,  $N_2$ ,  $N_3$  are the populations of the ground, intermediate and upper laser excited state, respectively. Values  $\sigma^{(2)} = (1.44 \pm 0.43) \times 10^{-46}$  cm<sup>4</sup>s, the effective two-photon absorbtion cross-section;  $\sigma_e = (2.01 \pm 0.22) \times 10^{-12}$  cm<sup>2</sup>, the stimulated emission cross section; and  $A_{32} = (2.89 \pm 0.31) \times 10^7$  s<sup>-1</sup>, the spontaneous emission rate coefficient<sup>61</sup>. In Eq. (25)  $G = \exp[(N_3 - N_2)\sigma_e z]$  is the gain factor<sup>64</sup> and  $q$  is the stimulated emission photon density. Then, just below the onset of SE ( $q \approx 0$  and  $G \approx 1$ ) and at steady-state conditions ( $dN_3 / dt = 0$ ), we obtain  $\sigma^{(2)}\Phi^2(N_1 - N_3) = A_{32}N_3$ , or  $N_1 / N_3 = 1 + A_{32}/\sigma^{(2)}\Phi^2 \approx A_{32}/\sigma^2\Phi^2$ . With a reasonable, but quite approximate, assumption of a focused laser beamspot diameter of 200 μm, we obtain for our experiment  $\Phi \approx 3 \times 10^{25}$  cm<sup>-2</sup> s<sup>-1</sup>, whereas in Fig. 2 of Huang and Gordon<sup>61</sup>,  $\Phi = 3 \times 10^{26}$  cm<sup>-2</sup> s<sup>-1</sup>. This result implies an approximate factor of 100 increase in  $N_1$  is required in our experiment to produce the same density  $N_3$ , the latter density controlling the SE. This result puts the calculation in

reasonable (factor of 2) agreement with our experimental result.

Efficient depopulation of the  $3p^3P$  level by the SE channel is expected to cause a deviation of the TALIF signal from a linear response as function of O-atom concentration. We sought such deviation in our data as an indication for the influence of SE on TALIF, which would provide another test for the theory. Fig. 26 shows the strongest influence of SE on the TALIF signal that has been observed in our measurements. The TALIF signal appears to be linear up to an O-atom concentration of  $4 \times 10^{14}$  atoms/cm<sup>3</sup>, above which it exhibits a saturation-like behavior. We thus observe that TALIF is not affected by the SE for concentrations up to about twice the threshold concentration  $N_{thr}$ . This is in reasonable agreement with the model<sup>61</sup> which predicts less than 20% reduction of the laser-excited level concentration due to SE at  $2N_{thr}$ . Furthermore, the observed 30% reduction of TALIF signal at O-atom concentration  $3N_{thr}$  is also in agreement with the model.

The general method we present in this work, for evaluation of a threshold for SE and investigation of the SE influence on TALIF, can be applied to a large variety of plasma environments where TALIF is employed as a diagnostic tool. Since plasma reactors are utilized today for a variety of applications, we chose to demonstrate the applicability of this method in an RF cell. The experimental set up has been described previously. For these experiments, the titration system has been detached from the rest of the reactor and a planar water-cooled stainless steel electrode has been mounted in its place, opposite to an identical electrode. Ground state O( $2p^3P$ ) atoms were generated in the RF reactor operating at 10 MHz. Pure oxygen has been used at pressures in the range 0-2 Torr. The data for TALIF and SE signals as functions of pressure are presented in Fig. 27. The TALIF signal has been corrected for the increase in quenching of the

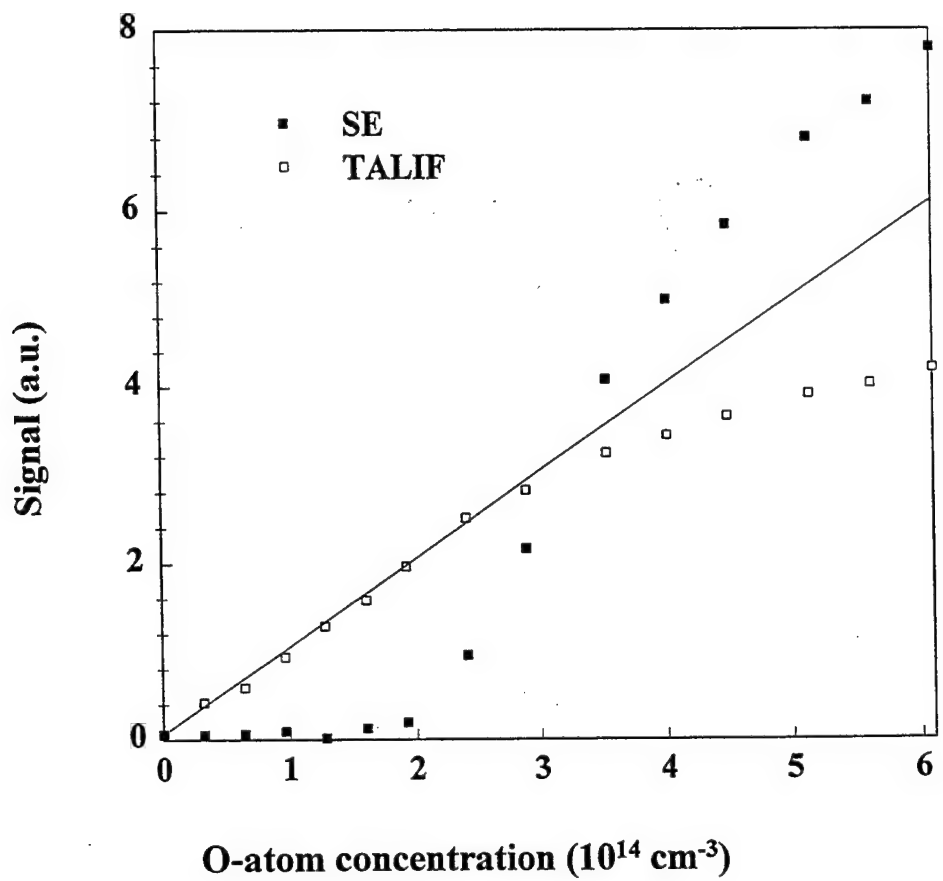


Figure 26. Titration curve showing a strong deviation of the TALIF signal from linearity due to significant SE. The observed reduction in TALIF due to SE is about 30%, the highest we have observed in our experiments.

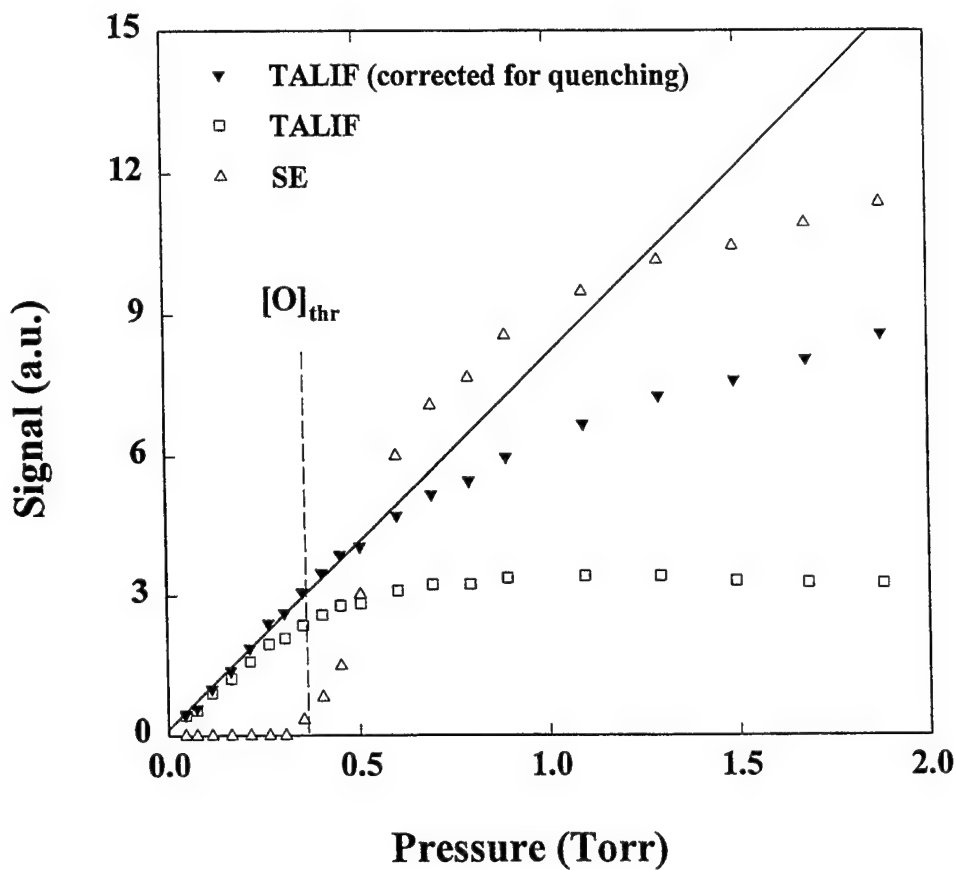


Figure 27. Pressure dependence of TALIF and SE signals in an RF parallel plate reactor. The raw TALIF data (open squares) have been corrected for the quenching of the laser-excited state by O<sub>2</sub> and a linear fit (solid line) is done to the corrected data (solid triangles). The O concentration at SE threshold is  $[O]_{\text{thr}} = 3.6 \times 10^{14} \text{ cm}^{-3}$ .

upper state by O<sub>2</sub>, as the pressure of oxygen rises (the quenching rate constant was measured in a separate experiment<sup>65</sup>). Since the data in the RF cell were taken under identical excitation and detection conditions as the titration experiment, we were able to calibrate the TALIF signal. The SE signal rises abruptly from zero at about 0.3 Torr O<sub>2</sub> pressure, or equivalently for a ground state O-atom concentration of  $3.6 \times 10^{14}$  atoms/cm<sup>3</sup>. The deviation of the (corrected for quenching) TALIF response from linearity starts above twice this concentration, in agreement with our observations above.

At high pressures, the observed deviation from linearity could result from either SE or from a sublinear production of O atoms as a function of O<sub>2</sub> pressure, due to a decrease in the efficiency of the discharge with increasing pressure. Therefore, the 50% TALIF reduction shown in Fig. 27 constitutes an *upper* limit of the effect of SE on the TALIF signal in a 2 Torr plasma. We further observe that the linearity of the TALIF signal with ground state O-atom concentration is re-established at high pressures. Similarly, Amorim *et al.*<sup>66</sup> found a linear increase of the TALIF as well as the SE signal at high concentrations, for O and H atoms. In fact, the rate of increase with concentration for both TALIF and SE signals is shown to be the same, implying that the ratio of the laser-excited atoms that decay to the intermediate level via TALIF and SE remains constant. This means that TALIF would remain a reliable tool for probing ground state concentrations that are much higher than the SE threshold values.

We believe that the method we have presented here for determination of the SE emission threshold provides a general diagnostic technique which can be easily applied to other atomic systems that exhibit similar spectroscopic characteristics. Certainly, it can be employed in other more complicated environments (such as flames, combustion environments, etc) to distinguish

between the effect of the stimulated emission and other competing mechanisms that perturb the population of the laser-excited state.

5. Angular Momentum State Mixing and Quenching of n=3 Atomic Hydrogen Fluorescence

Laser diagnostics have provided a means for making *in situ*, localized, and temporally precise measurements on a variety of chemical plasma parameters, including electric fields,<sup>67</sup> gas species temperatures and velocities, and concentrations.<sup>68</sup> Important to all varieties of low temperature plasma discharge environments is the presence of atomic species usually generated via electron impact dissociation of parent molecules. The atomic species present in plasma discharges can be generated with considerable translational energy and may be either in their ground or excited states. The capability to measure relative or absolute concentrations of atoms in plasmas can provide information on one of the dominant reactive species in chemical plasmas.

Hydrogen-bearing or hydrogenic plasmas are important for semiconductor processing applications such as amorphous silicon deposition from silane ( $\text{SiH}_4$ ) discharges, for H<sub>2</sub> discharge passivation of GaAs, for H<sub>2</sub>/CH<sub>4</sub> discharge etching of InP, and now for the production of novel materials such as diamond thin films by plasma-assisted chemical vapor deposition. Certainly, ground state atomic hydrogen is one of the dominant reactant species produced by these discharges, so that measuring H atom distributions is useful for modeling and control of these processes.

However, there exists a difficulty which figures predominantly in plasma TALIF concentration measurements above a few hundred millitorr. The difficulty arises due to quenching of the excited fluorescence state by collisions with ambient background gas molecules. Molecular hydrogen, in particular, is known to be a very efficient fluorescence quenching molecule.<sup>69</sup> Reference data in the form of collisional quenching rates are few and often in disagreement.<sup>70</sup> Bittner *et al.* have provided the most comprehensive collisional

quenching rate constants to date in conjunction with their analysis of atomic hydrogen and oxygen measurements in low pressure afterglows.<sup>51</sup>

Since collisional fluorescence quenching effects are very pronounced at higher pressures such as required in CVD diamond deposition, it is necessary to quantify this quenching as completely as possible to extend our previous work to higher pressures. To obtain a convenient concentration of H atoms for this purpose, we use photodissociation of C<sub>2</sub>H<sub>2</sub> to generate ground state H atoms in a static pressure cell. The H atoms are subsequently excited by the TALIF laser probe and the effects of adding other gases at various pressures are studied to determine rate constants for quenching of the n=3 excited state atomic fluorescence used in the TALIF diagnostic. Quenching was measured both by lifetime measurements (up to the temporal response resolution of the photomultiplier used) and by time-averaged integrated signal measurements which allowed extension into much higher pressure regimes.

#### A. Experiment

The TALIF transition for atomic hydrogen is from the 1s<sup>2</sup>S<sub>1/2</sub> ground state to the 3d<sup>2</sup>D<sub>5/2,3/2</sub> and 3s<sup>2</sup>S<sub>1/2</sub> excited states at 97492 cm<sup>-1</sup>, which requires two 205.14-nm photons for excitation ground state. Procedures for the excitation and detection are as described previously in this report.

The photodissociation of acetylene provides a convenient source of hydrogen atoms using the 205-nm TALIF laser probe beam. A previous study of photodissociation of acetylene was completed in the wavelength region 201-216 nm.<sup>71</sup> The photodissociation process at 205 nm was shown to produce solely ground state C<sub>2</sub>H and H atoms. The excited C<sub>2</sub>H<sub>2</sub> predissociative state was also measured in this work to have a lifetime of 10-20 picoseconds, which implies that over

the lifetime of this state the molecule can suffer practically no deexcitation collisions even up to ambient pressures of several hundred Torr. Given the same concentration of C<sub>2</sub>H<sub>2</sub> and photon flux density, the photodissociation process should yield a H-atom concentration independent of the pressure or the identity of other gases present, provided the gas environment is optically thin to the probe laser. Our measurements in a static cell pressurized with neat acetylene have shown that the system will remain optically thin below ~5 Torr. For the other gases used here, no absorption at 205 nm could be observed experimentally.

The quenching measurements using acetylene at 60-120 mTorr were performed in a glass cell equipped with quartz windows which could be filled with gases and the pressure monitored with a capacitance manometer. Ultra-high purity research grade gases were used in all experiments. The pressure of quenching gases was raised incrementally using needle valves or mass flow controllers and measurements obtained using either statically filled or flowing gas fills. No discernable systematic difference was found in obtaining the measurements by either method.

#### B. Results and Analysis of Excited State Fluorescence Quenching Measurements

As an obvious first step we examined the effect of acetylene pressure on the fluorescence itself. The H atom TALIF signal response as a function of acetylene pressure is shown in Fig. 28. After an initial linear rise, the photodissociation-generated TALIF signal begins to saturate around 1 Torr ambient pressure. At pressures above 150 mTorr, the TALIF signal response deviates strongly from a linear process which would depend solely on acetylene concentration. The quantum yield in our experiments can be defined as the ratio of the actual TALIF signal data to the value predicted by the straight line fit to the (lowest pressure) linear data.

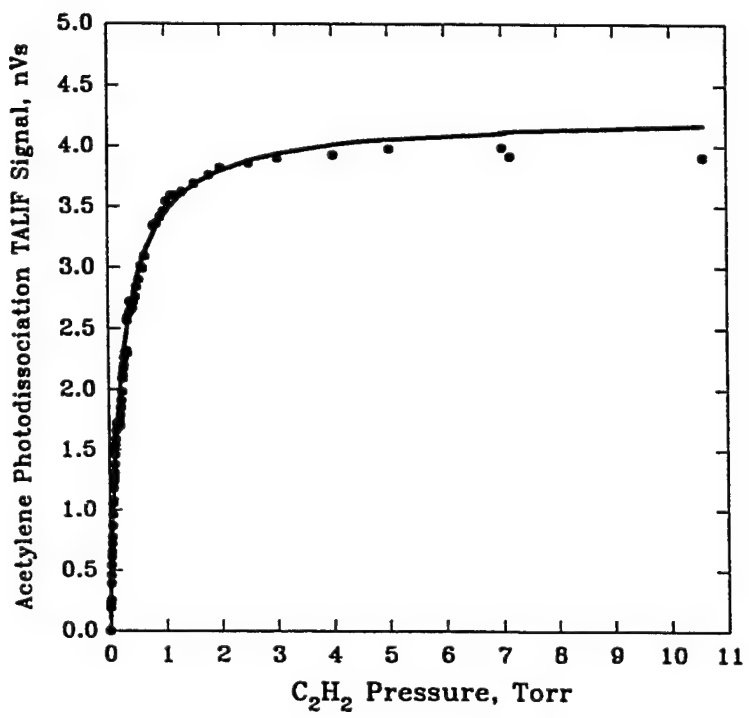


Figure 28. Measured Versus Calculated Photodissociated Acetylene H-Atom TALIF Signal.

Besides affecting the overall TALIF signal strength as a function of pressure, the apparent radiative lifetime of the atom is also influenced. Figure 29 shows the lifetime dependence of the H atom n=3 state as a function of background acetylene pressure. At very low pressures the radiative lifetime approaches  $15.7 \pm 1.5$  ns. This value is larger than the statistical average lifetime of the n=3 state. The explanation for this observation is that the three angular momentum states of the n=3 level are not equally populated. Due to the selection rules for such a two-photon absorption transition only the L=0 and L=2 states and not the L=1 state are populated. In addition, the two-photon absorption cross-sections to the S and D state are different. The ratio of the D-state absorption cross-sections to that for the S-state is 7.56.<sup>72</sup> Since the laser linewidth is wider than the energy separation between each L-state, this means that; 12% of the n=3 population is contributed by the s-state and the remaining 88% is contributed by the d-state. The natural radiative lifetime of the d-state is 15.6 ns and 159 ns for the s-state. Thus, the observed lifetime for the n=3 level in this experiment at low pressure is dominated by the D-state natural radiative lifetime.

Collisional quenching of the excited state fluorescence can be thought of as having two mechanisms. The first would be an overall nonradiative deexcitation of the excited state atom. The second mechanism would involve the mixing of angular momentum L-state populations within the n=3 energy level. It is reasonable to expect that collisions could perturb the distribution in the angular momentum states after population by the laser. This redistribution or mixing of the angular momentum state populations can have two effects. First, there would be variations in the contributions to the radiative lifetime of the Balmer- $\alpha$  fluorescence from each of the three states. Secondly, since the p-state could then be populated by mixing, not only does the

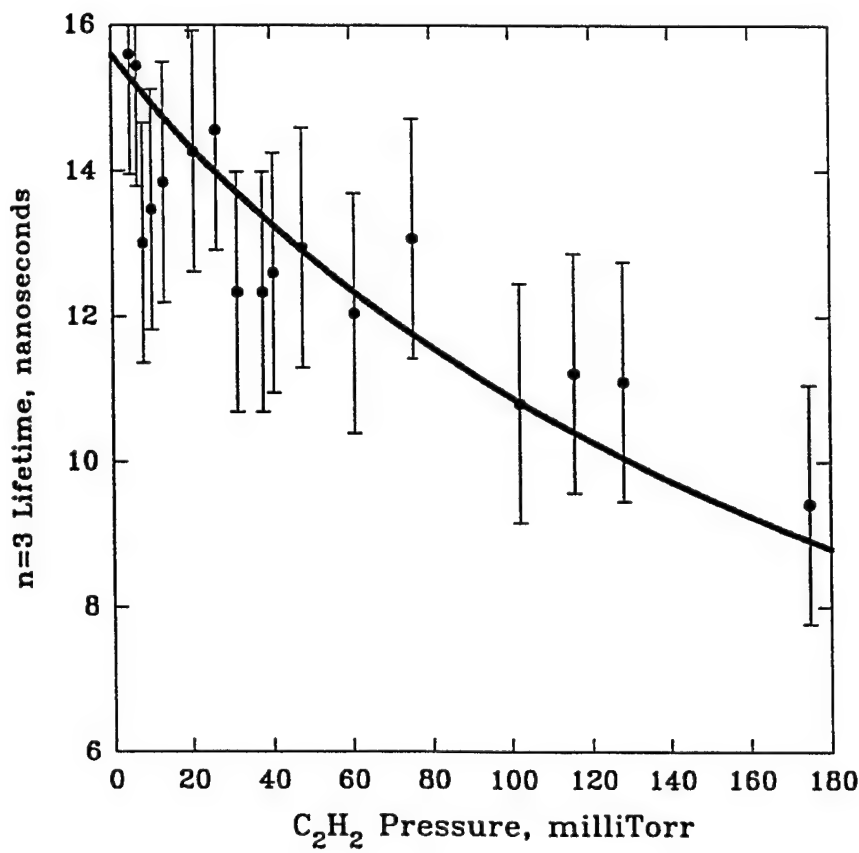


Figure 29. Measured versus Calculated H-Atom TALIF Lifetime from Photodissociation of C<sub>2</sub>H<sub>2</sub>. Curved line is predicted from model calculations.

3p-2s channel contribute Balmer- $\alpha$  fluorescence, but the 3p-1s fluorescence channel in the vacuum ultraviolet allows for a loss of fluorescence from the Balmer- $\alpha$  emission. A simple model incorporating these mechanisms yields a set of coupled rate equations which describe the time development of the n=3 angular momentum L-state populations after population by the laser probe:

$$\begin{aligned}\frac{dN_s}{dt} &= -N_s \left\{ \frac{1}{\tau_s} + N_Q (8k_{mix} + k_Q) \right\} + N_Q k_{mix} (N_p + N_d), \\ \frac{dN_p}{dt} &= -N_p \left\{ \frac{1}{\tau_p} + N_Q (6k_{mix} + k_Q) \right\} + 3N_Q k_{mix} (N_s + N_d), \\ \frac{dN_d}{dt} &= -N_d \left\{ \frac{1}{\tau_d} + N_Q (4k_{mix} + k_Q) \right\} + 5N_Q k_{mix} (N_s + N_p)\end{aligned}\quad (26)$$

where  $N_s$ ,  $N_p$ , and  $N_d$  are the populations of the s, p, and d angular momentum states,  $N_Q$  is the concentration of quenching molecules, and  $k_{mix}$  and  $k_Q$  are rate constants respectively associated with collisional population mixing of the angular momentum L-states and nonradiative deexcitation of the entire n=3 manifold respectively. In the above we have assumed the mixing rates between different L-states are the same,  $k_{mix}$ , and the integer coefficients account for the statistical weighting of the L-states degeneracies by the number of  $m_l$  sublevels. The right-hand side of each rate equation has two parts. The leftmost term accounts for population loss and the right term accounts for population gain. Loss occurs directly by fluorescence or by transfer to other angular momentum states or by nonradiative deexcitation. Gain for a level occurs by transfer from the other L-states.

This set of coupled rate equations is solved numerically by a Runge-Kutta differential

equation routine written in Fortran.<sup>73</sup> While the most rigorous approach to solving these equations would involve the effect of the time-dependent laser excitation, we have assumed as a practical approximation the instantaneous population of the excited states by the laser probe where the initial conditions are given by the initial L-state distributions populated by the laser. The equations are then allowed to propagate in time without reference to the temporal response profile of the laser. The time development of the L-state populations is shown for an arbitrary foreign gas at 10 Torr in Fig. 30. The calculations are normalized with respect to the initial overall populations in the n=3 energy level with quenching eliminated. Also displayed is a normalized radiative rate which is related to the time history of the total population of the n=3 level. A radiative rate from the n=3 level can be defined as

$$R(t) = \frac{f_s}{\tau_s} N_s(t) + \frac{f_p}{\tau_p} N_p(t) + \frac{f_d}{\tau_d} N_d(t) \quad (27)$$

where  $f_s$ ,  $f_p$ , and  $f_d$  are the branching ratios for fluorescence decay from each L-state of the n=3 level to lower n-levels. The S and D states each decay to a single lower state in the n=2 level, so  $f_s$  and  $f_d$  are unity. The P-state however, can decay not only to the 2S state, but also to the 1S level. The branching ratio,  $f_p$ , can be calculated as the ratio of the transition probabilities for the transitions 3P-2S and 3P-1S.<sup>72</sup> This gives a branching ratio for  $f_p$  of 0.1183.

The radiative rate in Eq. 27 can be normalized to the radiative rate at time t=0 and integrated with respect to time to determine the quantum yield. At time t=0, only the S and D states are populated and so the initial radiative rate,  $R_0$ , is calculated as

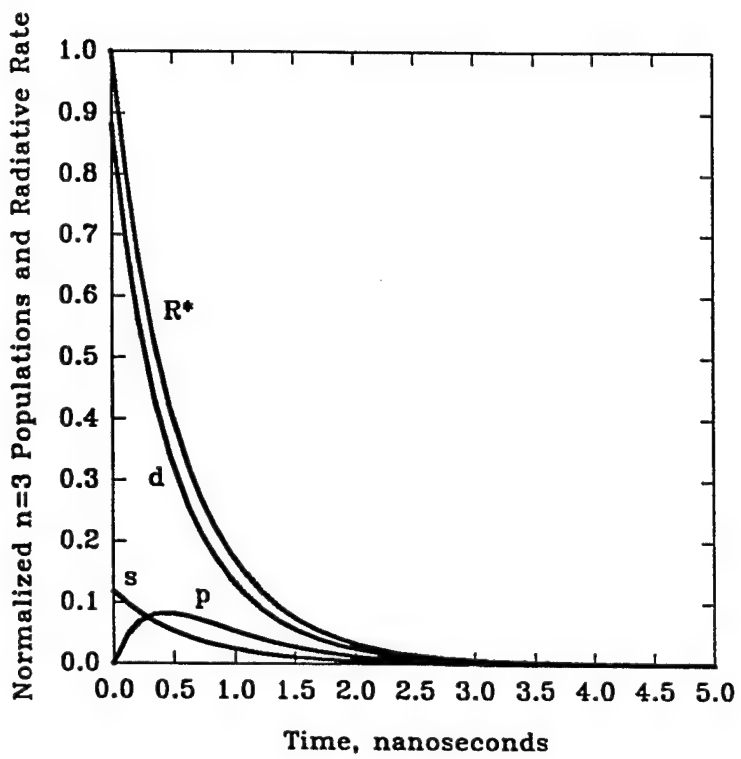


Figure 30. Radiative Decay of  $n=3$  Component Levels for 10 Torr Quenching by  $H_2$ . Also shown is the Normalized Radiative Rate,  $R^*$ .

$$R_o = \frac{N_s(0)}{\tau_s} + \frac{N_d(0)}{\tau_d} = \frac{0.118}{1.59 \times 10^{-7} s} + \frac{0.882}{1.56 \times 10^{-8} s} = 5.73 \times 10^7 s^{-1} \quad (28)$$

The inverse of  $R_o$  gives a natural radiative lifetime of 17.4 ns which approximates our measured lifetime value extrapolated to zero pressure of quenching gas.

Thus, the normalized radiative rate,  $R^*$ , can be given by

$$\begin{aligned} R^*(t) &= \frac{R(t)}{R_o} \\ &= (1.75 \times 10^{-8} s) \left( \frac{N_s(t)}{1.59 \times 10^{-7} s} + \frac{0.1183 N_p(t)}{5.4 \times 10^{-9} s} + \frac{N_d(t)}{1.56 \times 10^{-8} s} \right) \end{aligned} \quad (29)$$

where  $N_s(t)$ ,  $N_p(t)$ , and  $N_d(t)$  are the solutions to Eq. (26).

The results shown in Fig. 30 reveals that at 10 Torr, the p-state is actively contributing to the radiative decay and the overall decay rate is much faster than for zero pressure of quenching gas. The exchange of L-state populations can be checked in the numerical calculation output by artificially increasing the natural radiative lifetime for all three states to very large values (effectively turning off fluorescence) and by setting the rate constant  $k_Q$  for nonradiative deexcitation to zero. Calculated numbers for pressures above a few hundred millitorr show the populations of the L-states have equilibrated in the percentages: 11.11% in the s-state, 33.33% in the p-state, and 55.55% in the d-state, just as expected by the statistical weighting given by the  $m_i$

degeneracy's of each L-state. Since the contribution from the s-state population goes only from 11.8% to 11.11%, one can again see that the principal exchange of L-state populations occurs between the p and d states.

Trapezoidal integration of the normalized radiative rate (Eq. 29) with respect to time gives the quantum yield of the Balmer- $\alpha$  fluorescence. The integration time is 100 ns which reflects the temporal gate width used in the experiment. To analyze the data the computational model is included as a subroutine in a nonlinear-least-squares fitting program. Experimental quenching data are used as input to the program which then fits the corresponding mixing and deexcitation rate constants. Figure 31 shows a comparison of the fitting program results and experimental data for the "self-quenching" effect by  $C_2H_2$  itself on the H atom TALIF quantum yield. The deexcitation rate constant,  $k_Q$ , was calculated to be  $5.93 \pm 0.51 \times 10^{-9} \text{ cm}^3/\text{sec}$ . The mixing rate constant,  $k_{\text{mix}}$ , could not be adequately determined. For gases which are good quenchers (acetylene having the largest deexcitation rate constant measured), a determination of the mixing rate is less significant because of the dominance of the nonradiative mechanism.

Using the model, a TALIF signal response can be predicted as a function of acetylene pressure. Figure 28 also shows a comparison between the original data and the predicted signal. Over a large range of pressure the agreement between the calculated signal and the data are excellent. Only above  $\sim 3$  Torr does the calculated curve predict a slightly larger signal than are observed. This is expected since the model does not take into account the onset of optical opaqueness near 5 Torr of acetylene as was previously mentioned and some other high pressure effects which will be discussed subsequently. As our use of acetylene as a photodissociated source of H atoms is accomplished near 100 mTorr, this discrepancy is unimportant.

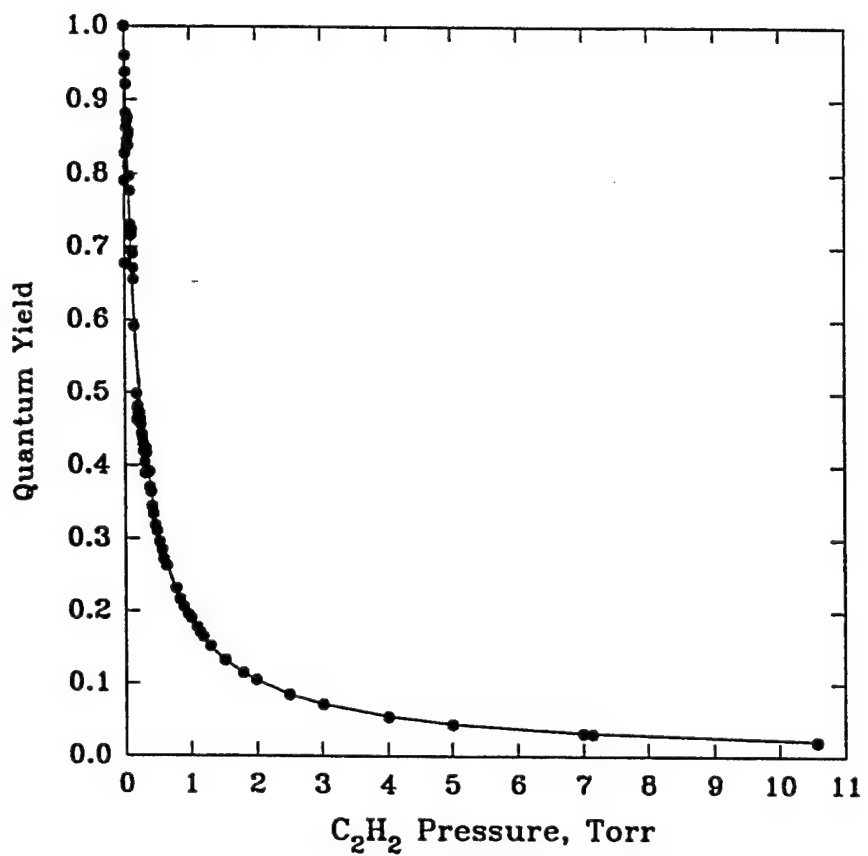


Figure 31. Comparison of Calculated and Experimental H-Atom TALIF Quenching by Acetylene.

Lifetimes calculated by the model can be compared to the measured n=3 lifetime data as shown in Fig. 29. The calculated lifetimes are shown as a curve having been derived by fitting a single exponential decay to the normalized radiative rate,  $R^*$ , (in the same manner as the actual lifetime measurements). The predicted lifetimes from the quenching data lie well within the error bars of the direct lifetime measurements. The extrapolated lifetime at zero pressure is 15.7 ns in good agreement with the decay being dominated by the n=3 D-state.

Quenching data can be taken using other gases and the computer program used to calculate quenching curves and rate constants. However, given the partial pressure of acetylene present, Eq. 26 must be modified to account for the "self-quenching" by acetylene. Addition of a constant term ( $2.35 \times 10^7 \text{ s}^{-1}$ ) to Eq. 26 is a straightforward way to account for quenching from  $\approx 100$  mTorr partial pressure of acetylene, with the known quenching rate constant.

Figure 32 shows a comparison of experimental quenching data for quenching by molecular hydrogen with the nonlinear regression calculation (shown as  $\log(1/Q)$  versus  $\log(P)$ ) fitted both with and without the contributions due to mixing. Note the good agreement of our predicted quenching curve with the data up to 10 Torr pressure.

While the agreement between the model involving collisional quenching and mixing and the data in Fig. 32 is satisfactory, there appears to be a small, but real, systematic discrepancy between the two above approximately 10 Torr. To eliminate this discrepancy, we introduce a new effect, which we call collisional cooling. Let us define an initial temperature,  $T_o$ , which characterizes the nascent H atoms formed upon photodissociation of  $\text{C}_2\text{H}_2$ , as well as the ambient temperature,  $T_A$ . The temperature,  $T_D$ , describing the Doppler profile of the two-photon absorption line is then given by:

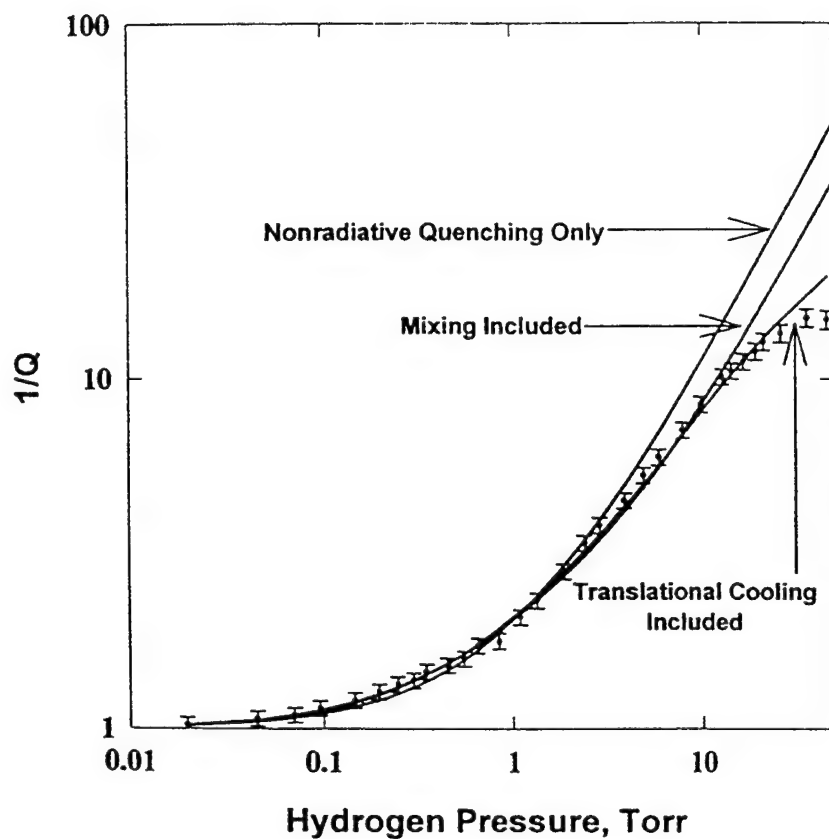


Figure 32. Comparison of Data with Calculated Quenching Curves fitted both with and without L-State Mixing and Translational Cooling for Quenching of H-Atom TALIF by H<sub>2</sub> Gas.

$$T_D = T_A + (T_D - T_A) e^{-\alpha P} \quad (30)$$

where P is the quenching gas pressure and  $\alpha$  is a molecular constant determined by the quenching gas and with dimensions of inverse pressure.

A fractional absorption for the inhomogeneously broadened atoms can then be computed by ratioing the convoluted laser spectral profile and the 2-photon Doppler limited absorption at  $T_D$  with the corresponding quantity computed at  $T_A$ . The quantum yield is then computed by multiplying the initial populations of  $N_s(0)$ ,  $N_p(0)$ , and  $N_d(0)$  by this fractional absorption and normalizing to unity quantum yield at zero pressure. This correction factor is relatively small ranging from unity at zero pressure to 2.4 at 50 torr for H<sub>2</sub>. However, as Fig. 32 shows, it substantially improves the agreement between the model and the observed Q values at the highest pressures in the figures.

We have followed this approach with the other gases and Fig. 33 shows the results for quenching of H atom TALIF by helium. Shown are averaged experimental data and corresponding calculated quenching curves. The upper curve is calculated including only quenching and the rate constant reported by Bittner *et al.* for helium.<sup>51</sup> The experimental data differs significantly from this calculated curve above 10 Torr suggesting their lower pressure ( $\leq 7$  Torr) data are insufficient to fully determine the rate constants. Bittner *et al.* in their lifetime measurements used the same model photomultiplier tube as for the present measurements. Their measured quenching rate constant is a factor of five smaller than our determination (see Table 2) and their results do not allow for the significance of the L-state mixing process.

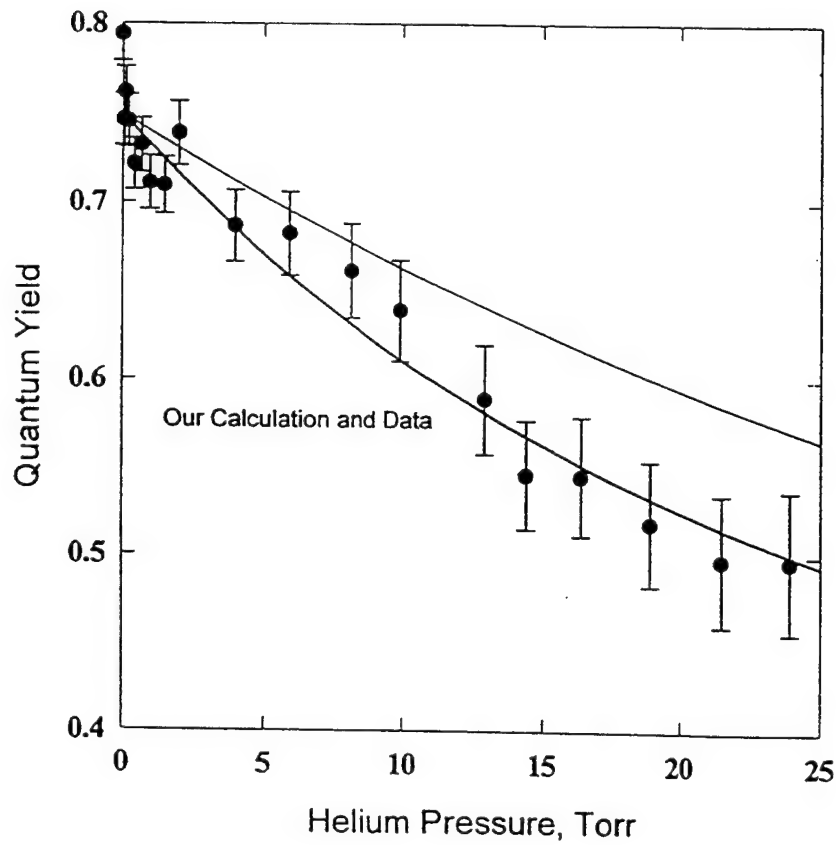


Figure 33. Quenching of H-Atom TALIF by Helium. Solid curve is calculated from represented model. The upper curve is calculated based on data from Reference 51.

**Table 2. Rate Constants for Quenching of Hydrogen Atoms (n=3).**

Quenching Gas	Present Measurements ( $10^{-9}$ cm $^3$ /sec)	Bittner <i>et al.</i> Measurements ( $\times 10^{-9}$ cm $^3$ /sec)
He	$k_Q = 0.053 \pm 0.0005$ $k_{\text{mix}} = 0.007 \pm 0.004$ $\alpha = \text{Not Determined}$	$k_Q = 0.0099 \pm 0.005$
Ar	$k_Q = 0.38 \pm 0.03$ $k_{\text{mix}} = 0.11 \pm 0.03$ $\alpha = \text{Not Determined}$	$k_Q = 0.46 \pm 0.05$
H <sub>2</sub>	$k_Q = 1.78 \pm 0.14$ $k_{\text{mix}} = 0.80 \pm 0.11$ $\alpha = 0.049 \pm 0.015$	$k_Q = 1.99 \pm 0.3$
N <sub>2</sub>	$k_Q = 2.54 \pm 1.73$ $k_{\text{mix}} = 0.23 \pm 0.86$ $\alpha = 0.13 \pm 0.12$	$k_Q = 2.77 \pm 0.11$
O <sub>2</sub>	$k_Q = 3.65 \pm 0.42$ $k_{\text{mix}} = 0.44 \pm 0.26$ $\alpha = 0.040 \pm 0.019$	$k_Q = 2.60 \pm 0.1$
C <sub>2</sub> H <sub>2</sub> <sup>a</sup>	$k_Q = 5.93 \pm 0.51$	$k_Q = 5.60 \pm 0.4$

<sup>a</sup>  $k_{\text{mix}}$  and  $\alpha$  not determined, see text.

By selecting another rare gas like argon, which is larger and heavier than helium, there should be an increase in the quenching effects. Figure 34 shows quenching data and the calculated quenching curves for argon and oxygen, and again we have good agreement between the calculated versus measured curves. It is also apparent for gases such as argon and other molecular gases that the radiative lifetime of the n=3 level would rapidly drop to levels where variations in the lifetime would be unresolvable from instrumental contributions.

Table 2 summarizes all the calculated quenching and mixing rate constants and compares them with rate constants from earlier work.<sup>51</sup> Generally, there is reasonable agreement between the measured nonradiative collisional deexcitation rate constant,  $k_Q$ . However, as shown in the Table and in Fig. 32, the inclusion of L-state mixing is clearly of statistical significance and obviously necessary to reproduce our higher pressure experimental data.

### C. Discussion

The most important results summarized in Table 2 are the quenching,  $k_Q$ , and mixing,  $k_M$ , rate constants. Together these allow an accurate computation of the fluorescence quantum yields at a given pressure of foreign gas, thereby permitting the determination of absolute H atom densities from TALIF diagnostics. In the last column of Table 2 are also given the  $k_Q$  measurements of Bittner et al., determined by the independent technique of lifetime measurement. It is very clear that there is good qualitative agreement between their and our results. Indeed most of the  $k_Q$  values overlap within two standard deviations of the independent measurements. Considering, in addition, that in the present case a more complex model has been used to analyze the data, the results are surprisingly consistent.

Somewhat less satisfying is the comparison with the quenching of H by H<sub>2</sub> reported by

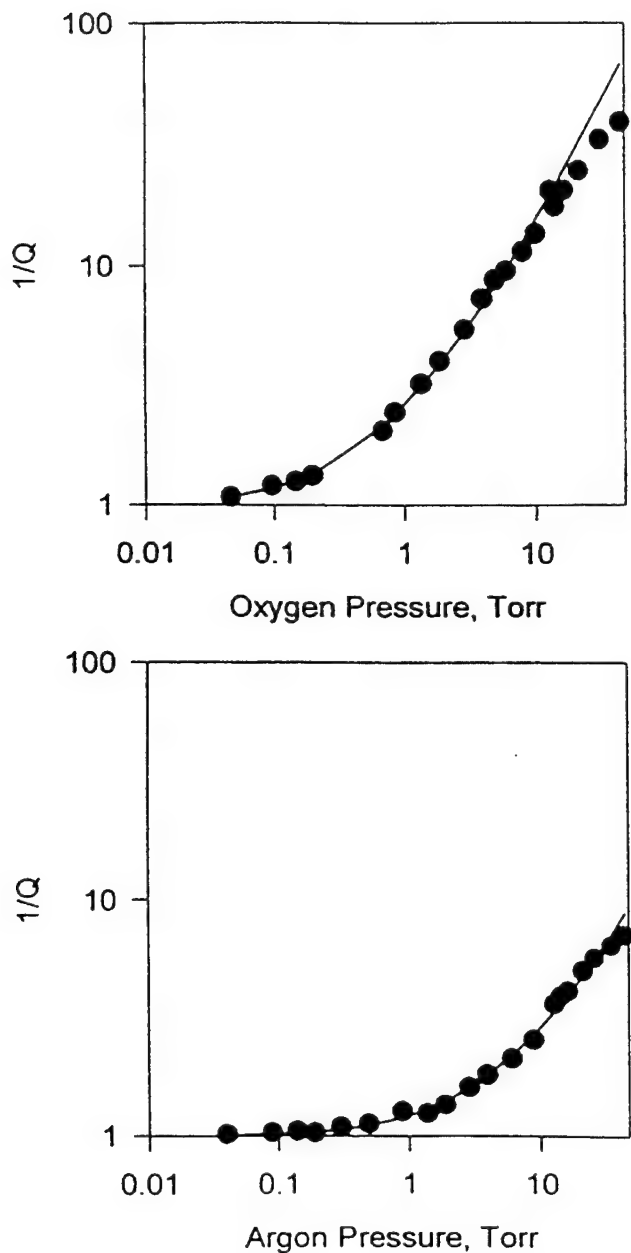


Figure 34. H-Atom TALIF Quenching by  $\text{O}_2$  (top) and Argon (bottom).

Hatano's group.<sup>74,75</sup> While their results are expressed in terms of cross-sections, these can be converted to rate constants since the collision velocity is known and indeed the cross-section is reported to be approximately independent of energy. Performing this conversion we obtain from their results,<sup>74</sup>  $k_Q = 6 \times 10^{-9} \text{ cm}^3/\text{s}$  for the 2s H state with a slightly higher value for the 3s and 3d states.<sup>75</sup> This value is about a factor of four larger than we (or Bittner, et al.) report. However, their analysis is again different and indeed in their case rejects detailed balance, which is implicit in our model.

We would like to comment briefly about the collisional cooling effect. First, we would note that the values of a given in Table 2 are physically quite plausible given reasonable cross-sections for momentum changing collisions.<sup>76</sup> However, the phenomenon of collisional cooling raises the issue of the temperature to which the rate constants in Table 2 refer. Over the pressure range measured  $T_D$  appears to decline from about 3000K to less than 1000K. This could be a serious problem were it not for two facts. The data of Hatano and co-workers imply that there is very little temperature dependence to the cross-sections. While we do disagree somewhat with the absolute magnitude of their cross sections, it is always more likely that the relative cross section measurements (as a function of velocity) are less subject to error than the absolute values. Furthermore, this point seems confirmed by the very good agreement between ourselves and the measurements of Bittner, et al which correspond to approximately room temperature. We conclude that our reported rate constants are valid over most, if not all, the temperature range between ambient and 3000K.

Finally, we would like to comment upon some preliminary quantum yield measurements made at yet higher pressures (up to nearly atmospheric). The analysis of these are ongoing, but it

should be mentioned that the present model while, giving good results, does show some discrepancies with the data, particularly at the highest pressures. Interestingly the experimental values of Q appear to be somewhat greater than expected. We are presently trying to refine the model to account for these very high pressure effects.

#### D. Conclusion

An extensive set of data has been taken for the fluorescence of n=3 H atoms in the presence of several foreign gases (He, Ar, H<sub>2</sub>, N<sub>2</sub>, O<sub>2</sub>, C<sub>2</sub>H<sub>2</sub>). To adequately describe the experimental data, three separate collisional effects have been incorporated in our model. Included are collisions which (i) change L-states within the n=3 manifold of H, (ii) deactivate the n=3 manifold, and (iii) translationally cool the H atoms. This model provides an excellent fit to the data and determines accurately parameters describing the collisional phenomena. Our model allows for quantitative analysis of the quenching of the TALIF diagnostic up to 50 Torr.

Because of the relative complexity of our model (three separate mechanisms - quenching, mixing, and cooling, as well as numerical integration of coupled differential equations), even given the rate constants of Table 2, prediction of the quantum yield for fluorescence at a given pressure of quenching gases is nontrivial. For that reason we have constructed Table 3 which gives the expected quantum yield as a function of pressure for each quenching gas investigated. Table 3 was generated for the pure gases, i.e., excluding the effects of self-quenching by the acetylene present in our experiments. Note also that Table 3 gives the true quantum yield for fluorescence, while the figures give our "observed" yield which is artificially increased at the higher pressures by the translational cooling effect which increases the number of atoms excited by the laser. Table 3 should therefore provide a convenient "look-up" table from which LIF

diagnostic experiments in a variety of environments such as low and moderate pressure plasma reactors or low pressure flames, can be “corrected” for less than unity quantum yield of emission.

**Table 3. Quantum Yield for n=3 H-Atoms in the Presence of Various Foreign Gases as a Function of Pressure at Room Temperature**

Pressure (Torr)	Helium	Argon	Hydrogen	Nitrogen	Oxygen	Acetylene
0	1.0000	1.0000	1.0000	1.0000	1.0000	1.0000
0.01	.9997	.9970	.9837	.9842	.9764	.9676
0.02	.9994	.9940	.9674	.9686	.9537	.9374
0.03	.9990	.9910	.9511	.9535	.9317	.9090
0.04	.9986	.9880	.9352	.9388	.9107	.8823
0.05	.9983	.9850	.9196	.9245	.8904	.8572
0.06	.9979	.9821	.9045	.9106	.8710	.8336
0.07	.9976	.9791	.8896	.8971	.8524	.8112
0.08	.9972	.9761	.8753	.8840	.8345	.7901
0.09	.9969	.9733	.8613	.8711	.8173	.7700
0.1	.9965	.9703	.8479	.8587	.8008	.7510
0.2	.9929	.9412	.7351	.7510	.6666	.6034
0.3	.9895	.9135	.6529	.6675	.5722	.5050
0.4	.9860	.8869	.5903	.6011	.5022	.4346
0.5	.9826	.8617	.5407	.5472	.4481	.3815
0.6	.9791	.8378	.5001	.5025	.4049	.3400
0.7	.9757	.8152	.4662	.4647	.3696	.3067
0.8	.9723	.7939	.4373	.4324	.3401	.2794
0.9	.9689	.7737	.4122	.4044	.3151	.2565
1	.9655	.7546	.3902	.3799	.2936	.2371
2	.9323	.6091	.2593	.2379	.1756	.1350
3	.9019	.5152	.1964	.1738	.1256	.0944
4	.8729	.4488	.1586	.1370	.0979	.0726
5	.8455	.3988	.1332	.1132	.0802	.0589
6	.8196	.3597	.1149	.0964	.0680	.0496
7	.7953	.3280	.1011	.0840	.0590	.0429
8	.7724	.3017	.0902	.0744	.0521	.0377
9	.7508	.2796	.0815	.0668	.0467	.0337
10	.7304	.2606	.0743	.0606	.0422	.0304
20	.5760	.1567	.0395	.0314	.0217	.0155
30	.4776	.1126	.0269	.0212	.0146	.0104
40	.4091	.0880	.0204	.0160	.0110	.0078
50	.3583	.0722	.0165	.0129	.0088	.0063

## 6. Application of TALIF Diagnostics to GEC Reference Reactor

In an effort to provide a secure experimental foundation and theoretical basis for understanding plasma processing techniques and systems, the plasma processing research community has in recent years advocated the development of standard reference plasma processing systems. Measurements in a reference plasma reactor would allow multiple plasma diagnostic techniques to characterize as completely as possible the internal operating environment of the reactor. By correlating measurements in several identical reference reactors at different institutions, a standardized concept of plasma reactor design and operation is more achievable. In turn, the standardization of diagnostic measurement techniques offers the opportunity to provide reproducible and transferable input data and thereby improve the ability of theory and computational programs to predict reactor operating parameters and to extrapolate the behavior of the standard reactor to either actual plasma processing production systems or to more innovative and developmental reactors. In the late 1980s, at a workshop sponsored by the Gaseous Electronics Conference (GEC), scientists and production engineers discussed the initial conceptual design of a standard reference cell reactor. The reactor came to be known as the GEC Reference Cell.

This section describes the results of spatially-resolved absolute concentration measurements for atomic hydrogen in a GEC reference cell. This reactor is installed at Wright-Patterson Air Force Base, Ohio, and these experiments illustrate our ability to transfer technical expertise developed at The Ohio State University to make measurements at an Air Force installation.

#### A. Review of the GEC Reference Cell

The Gaseous Electronics Conference Reference Cell (known as the GECRC) concept was initially conceived in 1988. A workshop dealing with preliminary design proposals for a standard reference cell plasma processing reactor was held during the 41st Annual Gaseous Electronics Conference (GEC) at the University of Minnesota in Minneapolis in October 1988.<sup>77</sup> The workshop attendees were asked to review several preliminary design proposals for the reference plasma system. Upon extended discussions a consensus was reached on developing a radio frequency (RF) excited parallel plate electrode plasma reference cell operating at 13.56 MHz. The following March of 1989, another workshop sponsored by SEMATECH was held in Austin, Texas.<sup>78</sup> At this workshop a committee of representatives from the plasma processing community reviewed comments from forty other plasma processing researchers regarding the initial design proposal formulated at the previous conference. Upon review of these comments the committee then finalized the GECRC design and determined the need to have four of the reactor systems built by industrial suppliers to test the GECRC design.

The basic configuration of the GECRC as mentioned is shown in Fig. 35. The cell is a UHV stainless steel chamber with a volume of approximately 12.9 liters, comparable in size to standard production plasma processing reactors. The 4-inch-diameter water-cooled electrodes used are made of aluminum with an adjustable (optional) interelectrode spacing nominally set at 1 inch. Provisions were made in the design to allow for other electrode materials such as stainless steel. The electrodes are insulated from the rest of the assembly by either alumina or teflon insulators. Surrounding the electrode insulators are grounded guard rings or shields which serve to help confine the plasma discharge to a cylindrical region between the electrodes of diameter

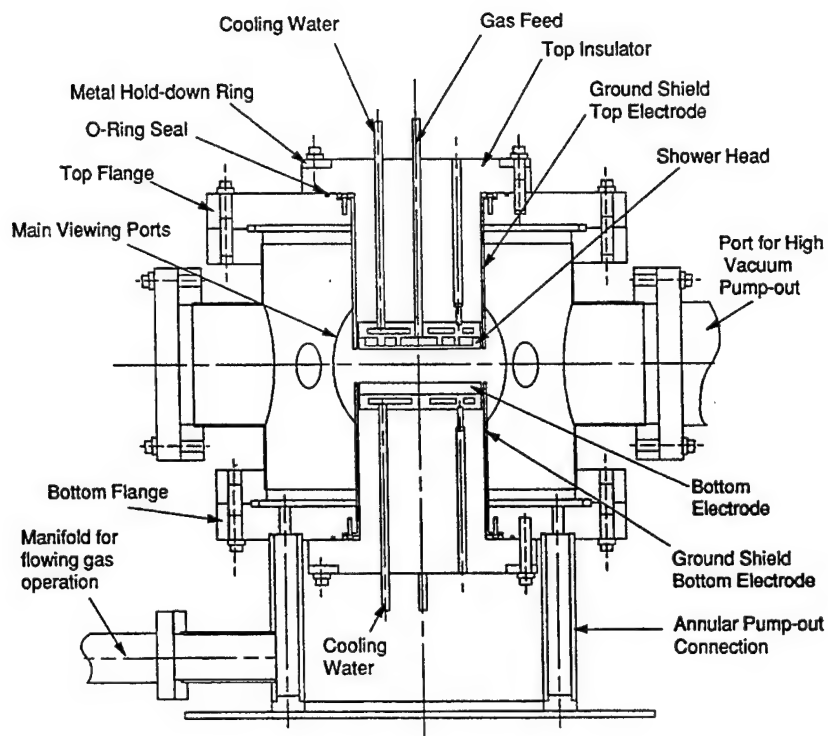


Figure 35. The GEC Reference Cell

approximately equal to the electrode diameter as well as to reduce sputter etching of the insulator material.

Vacuum pumping is accomplished through connection of the main chamber to a lower pump-out chamber. Slots in the flange interface between the two chambers serve to minimize angular variations in gas pumping speed around the main chamber volume. The chamber is typically pumped with a 300-liter-per-second turbomolecular pump backed on the foreline by a diaphragm roughing pump. The GECRC is designed to have a pump down base pressure of  $10^{-7}$  Torr and has low conductance because the pump-out manifold does restrict pumping speed. Typical gas flow rates are 10-100 standard cubic centimeters per minute (sccm) and operating pressures range from 50 millitorr to several Torr.

Access to the main chamber is provided by eight in-plane viewports: two 8-inch ports, two 6-inch ports orthogonal to the 8-inch ports, and four 2.75-inch ports intermediate between the larger ports. Longitudinal optical access to the inter-electrode volume can be achieved through any of these ports while complete radial or lateral access can only be accomplished through the largest ports. The window material is nominally high-grade vacuum port glass or for the measurements discussed in this thesis two of the 2.75-inch viewports were made of Supersil-1 fused silica.

The reactor chamber is typically filled with ultra-high purity research grade gases such as argon, helium, or hydrogen adjusted to specified flow rates by electronically controlled mass flow controllers. An electronically actuated throttle valve at the inlet to the turbomolecular pump provides pressure selection and stabilization. Either electrode of the GECRC can be grounded and the opposite excited by frequency/pulse generator and RF power amplifier configuration

either with or without the use of an in-line matching network.

Upon assembly and initial operation of five of the GECRC's, a program of electrical characterization was initiated. The electrical characterization diagnostics were discussed at a conference session during the 42nd Annual GEC held at Palo Alto, California in October 1989.<sup>79</sup> By the time of a separate workshop meeting hosted by SEMATECH of the GECRC design committee held in July 1990 at Dallas, Texas it had become apparent that electrical characterization and comparison between the few then operating GECRC's was not straightforward. This meeting established stringent procedures to make the required current and voltage measurements. The first public comparison of electrical data from six reference cells from five installations were presented at the 43rd Annual GEC held at the University of Illinois at Champaign-Urbana in October 1990.<sup>80</sup>

These electrical measurements showed a surprisingly large variation between installations. However, subsequent careful measurements have greatly aided our understanding of these variations and an improved equivalent circuit model. In addition, a low-pass filter circuit was developed for the input power feed to the cell, which eliminated the sensitivity of plasma operating conditions to the external circuitry. Nonetheless, these measurements demonstrated that for commercial plasma etching systems, the choice of power supply equipment and networks, grounding, cabling, would strongly influence the reproducibility of system-to-system design and operation, impacting on the actual plasma voltage, current, and DC bias and hence in etching performance and the degree of anisotropy of etched profiles as well as potentially the etching chemistry at the plasma-surface interface.

Soon after the initial development of the idea for a standard reference plasma system,

researchers working in plasma modeling began to develop computer codes to simulate the GECRC. Coupled advances in diagnostic measurements and refinement in computational models for the GECRC are important. In particular, those developing computer models are now being asked to incorporate excitation and production cross-sections and mechanisms for plasma species in addition to electrons such as ions and neutral species and to include the interactions of all plasma species with the electrode surfaces. The aim of computer modeling is to predict absolute concentration profiles of the most important plasma-generated species. With the problems regarding electrical characterization and correlation having been clarified, experimentalists began striving to develop diagnostic techniques to measure ion and neutral populations and distributions produced in the GECRC and to place these measurements on a absolutely calibrated scale rather than just a relative basis, for comparisons with the computer models.

There is certainly some continued scientific interest in measurements in a RF parallel plate electrode system such as the GECRC, even though the industrial uses of plasma processing are now focusing on the use of other plasma reactions, e.g., the microwave-based electron cyclotron resonance (ECR) or Helicon<sup>81</sup> source plasmas. The advantages of using a system such as the GECRC are the generally simple design and the ability of researchers using the GECRC to correlate their measurements with the large amount of experience and literature that has been accumulated over the past several decades regarding the diagnostics and operation of parallel plate plasma processing reactors. A solid understanding and ability to predict, design, and control precisely a parallel plate reactor's environment as in the GECRC should provide a firm basis for extending the scientific (versus empirical) design of more innovative plasma processing systems.

## B. Experiment

A schematic of the general experimental scheme used for the TALIF H atom detection is shown in Fig. 36. The schematic layout shows a RF reactor cell, power supply system, the 205-nm generating laser system, and the associated acquisition and control electronics.

The TALIF transition for atomic hydrogen is from the  $1s^2S_{1/2}$  ground state to the  $3d^2D_{5,3,2}$  and  $3s^2S_{1/2}$  excited states at  $97492\text{ cm}^{-1}$ . Both excited state levels are populated due to the energy level degeneracy in hydrogen for different angular momentum states and due to the two-photon absorption selection rule of  $\Delta l = 0, \pm 2$ . The transition requires two 205.14 nm photons to excite the atomic ground state. The TALIF transition has also been observed in deuterium at  $97519\text{ cm}^{-1}$  in the course of this work.

The excited state is weakly populated by the discharge impact kinetics due to a rapid ( $\sim 15$  nsec) radiative lifetime. Thus, the TALIF excitation can be expected to populate effectively the upper state provided sufficient photon density is available given the small two-photon absorption cross-section. As previously, TALIF measurements for H atoms are performed by sum-frequency mixing (SFM) in a beta-barium borate (BBO) crystal. The probe laser is generated by pumping a Quanta-Ray PDL-2 dye laser with the second-harmonic 532 nm output of a Quanta-Ray DCR-2A Nd:YAG laser operating at 20 Hz. The dye laser operates with Exciton Sulfurrhodamine 640 dye at 615 nm. The dye laser output is frequency doubled using a Quanta-Ray WEX KDP crystal providing an output of 7 mJ/pulse at 307 nm and a residual 14 mJ/pulse at 615 nm, which are mixed in the BBO crystal to achieve 205-nm radiation. The output from the BBO crystal can be as high as 800 microJoules/pulse with careful alignment and overlap of the two input beams. The conversion efficiency of BBO of our system was measured at 11% which is predominantly

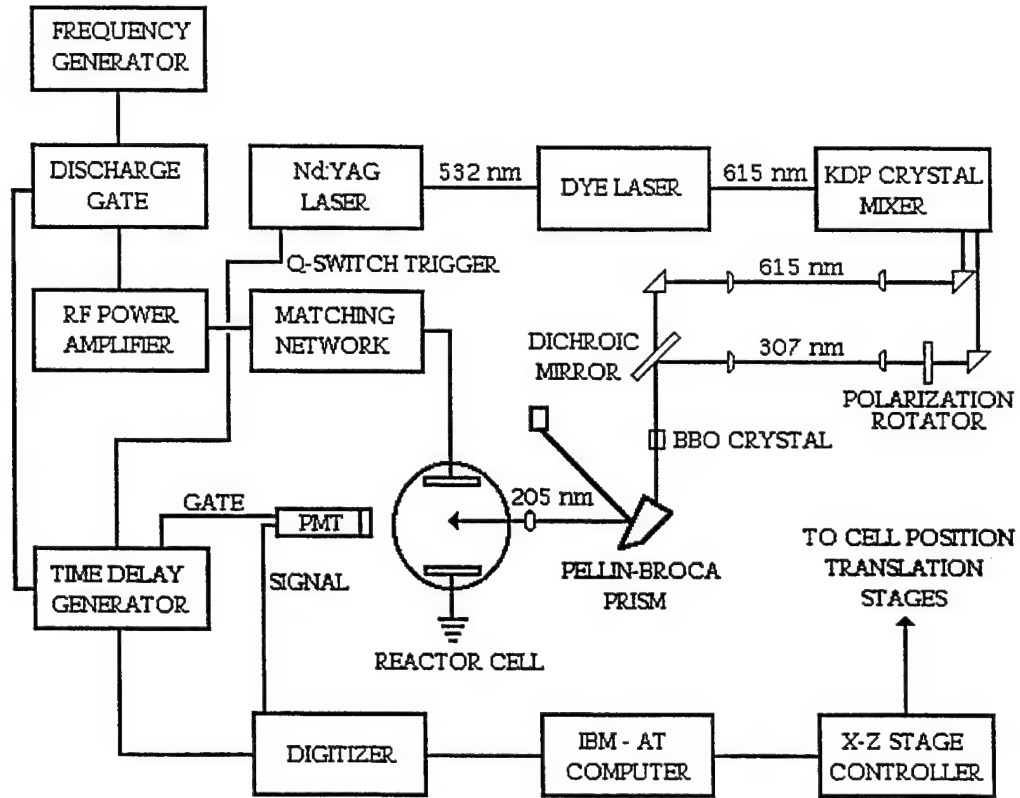


Figure 36. Experiment Layout Schematic for H-Atom TALIF

dictated by the input beam's profile quality and alignment. Upon leaving the BBO crystal the residual input pump beams are dispersed by a Pellin-Broca prism and beam dumped. The TALIF probe beam is tightly focused by a quartz lens through a Supersil 1 quartz window into the discharge reactor of interest.

#### C. H-Atom Concentration Calibration Procedure.

Calibration of the fluorescence signal collected by the PMT-Filter combination was performed using in situ titration of either the H atoms by chemical reaction with NO<sub>2</sub>.<sup>82</sup> For H atoms the titration reaction proceeds as



with a reaction rate constant of  $k_{298} = 1.3 \times 10^{-10} \text{ cm}^3 \text{ s}^{-1}$  where the rate constant is given for room temperature (T=298K). There is also a secondary reaction of OH with H<sub>2</sub> given by



with a reaction rate constant  $k_{298} = 1.6 \times 10^{-15} \text{ cm}^3 \text{ s}^{-1}$ . However, provided the ambient H<sub>2</sub> concentration remains below 1 Torr ( $3.3 \times 10^{16} \text{ cm}^{-3}$ ) this reaction will not appreciably perturb the main reaction. For H-atom reactions, sufficient mixing time must be allowed to ensure that the reactions go to completion. To have a reaction go to 99% completion implies that the mixing time,  $t_{\text{mix}}$ , must be greater than 5 characteristic reaction times,  $\tau$ . In other words, we have that the percentage of complete reaction is

$$1 - e^{-\frac{t}{\tau}} = 1 - e^{-\frac{5\tau}{\tau}} = 1 - e^{-5} = 0.9932 \approx 99\% \quad (33)$$

The characteristic reaction time is the inverse of the reaction rate constant times the concentration of titrant. For example, in the case of the reaction in Eq. 31, at the point of complete reaction (here called endpoint) a measured concentration of  $\text{NO}_2$  is used to react completely with an equal concentration of H atoms. If the concentration of  $[\text{NO}_2]$  used is  $1 \times 10^{15} \text{ cm}^{-3}$  then the required mixing time must be at least

$$t_{mix} \geq 5\tau = 5(k_{298}[\text{NO}_2])^{-1} = 7.7 \mu\text{s} \quad (34)$$

In the titration assembly described below, the main gas flow rates are adjusted to reduce the slug flow gas velocity in the mixing zone and raise the mixing time to approximately 4 milliseconds satisfying the condition in Eq. 34.

For a titration calibration measurement, a steady-state concentration of H is produced by the microwave cavity discharge source and  $\text{NO}_2$  is introduced at known mass flow rates. The TALIF fluorescence is monitored and recorded manually as a function of addition of  $\text{NO}_2$ . At the endpoint (minimum observable TALIF signal), the total pressure in the reactor is recorded. A straight line is least-squares fit to the first several titration data points and the exact  $\text{NO}_2$  endpoint mass flow rate is extrapolated numerically. Combining this information, we can use the following equation, where at the endpoint

$$[A]_o = [NO_2]_o = (3.3 \times 10^{16} \text{ cm}^{-3} \text{ Torr}^{-1}) \cdot \left( \frac{F(NO_2)}{\Sigma F} \right) \cdot P \quad (35)$$

where  $[A]_o$  is the concentration of H atoms titrated,  $[NO_2]_o$  is the concentration of  $NO_2$  used,  $F(NO_2)$  is the mass flow rate of  $NO_2$  measured in standard cubic centimeters per minute (sccm),  $\Sigma F$  is the total mass flow rates of all the gases used summed together, and  $P$  is the total pressure measured in Torr. The numerical coefficient is used to convert Torr into number density, per  $\text{cm}^3$ . Titration curves can be taken for different initial atomic concentrations, PMT gain settings, and probe laser energy. The calibrations curves correlate an experimental TALIF signal with a known concentration. Typical uncertainties in the calibrations are 15% and the minimum detectable concentration is extrapolated to be  $10^{12} \text{ cm}^{-3}$ .

To correction for variations in solid angle collection efficiency as a function of laser probe beam position between the electrodes, the reactor cell is filled with acetylene to 1 Torr and the photodissociated TALIF signal is recorded with the discharge off as a function of laser probe beam position.

#### D. Results and Discussion

H atom TALIF concentration profiles were collected for variety of discharge conditions corresponding to different RF power and reactor pressure. Over the range of parameters investigated, the most dramatic changes were seen as a function of discharge pressure. Figure 37 shows TALIF profile data collected for pressures ranging from 0.3 to 5 Torr for a total deposited discharge power of 30 watts. The driven electrode is at the origin. The data were acquired every 200 microns and averaged for 50 laser shots at 10 Hertz. The data have also been corrected for

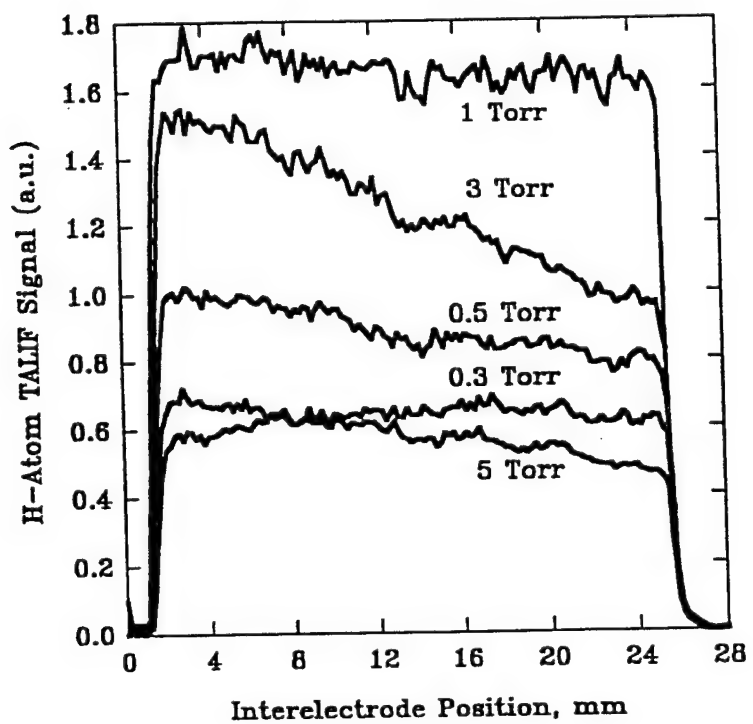


Figure 37. TALIF H-Atom Signal Profiles in GEC Reference Cell for Different  $H_2$  Pressures.  
Power deposited in plasma is 30 watts.

the geometric view factor. The median values for the profiles start at low values for low pressures and then reach an apparent maximum at approximately 1 Torr and then declining again at higher pressures. The slope of the data would appear to be roughly flat except at the higher pressures where a distinct slope is observable.

These H-atom concentration profiles were corrected for the influence of quenching on the TALIF quantum yield by dividing the profile at a given pressure by the associated quantum yield calculated from the model presented in the previous section. The quenching corrected profiles are shown in Fig. 38. Now it becomes apparent that the slope of the data is much more dramatic at higher pressures as well as there is a shift in the maximum concentration to 3 Torr instead of 1 Torr. These observations can be correlated with emission measurements as described below.

An alternative way of presenting the data in Figs. 37 and 38 is to plot the TALIF signal at two points -- one near the driven electrode and the other near the grounded electrode -- against pressure. These plots are shown in Figs. 39 and 40. As Fig. 40 clearly shows, initially the H concentration is comparable near each electrode and increases nearly linearly with increasing H<sub>2</sub> pressure. However in the 1-2 Torr range saturation in H-atom density begins and little increase in H-atom density is noted thereafter; however, in this higher pressure region a clear difference in H-atom concentration is denoted between the two electrodes.

It is clearly of interest to place the H-atom densities on an absolute scale. Based on in situ titration calibration of the TALIF signal, the observed TALIF signals can be converted to absolute hydrogen atom concentrations generated in the Reference Cell plasma. Table 4 shows the maximum H-atom densities as a function of pressure both before and after correction for the influence of fluorescence quenching. Also shown is the percentage H<sub>2</sub> dissociation fraction

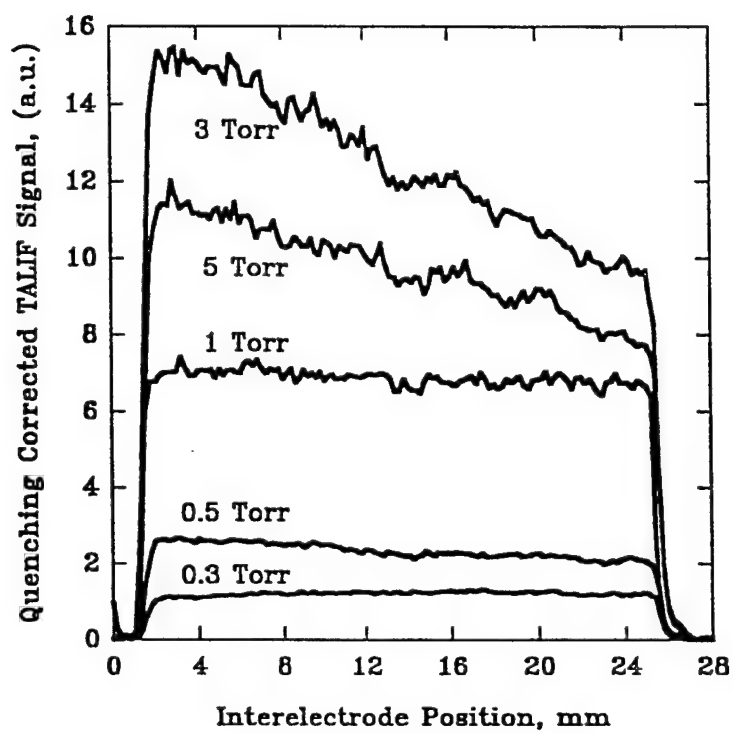


Figure 38. Quenching Corrected TALIF Signal Profiles from Fig. 37

Talif Signal at Electrodes vs. Pressure  
Quenching not considered

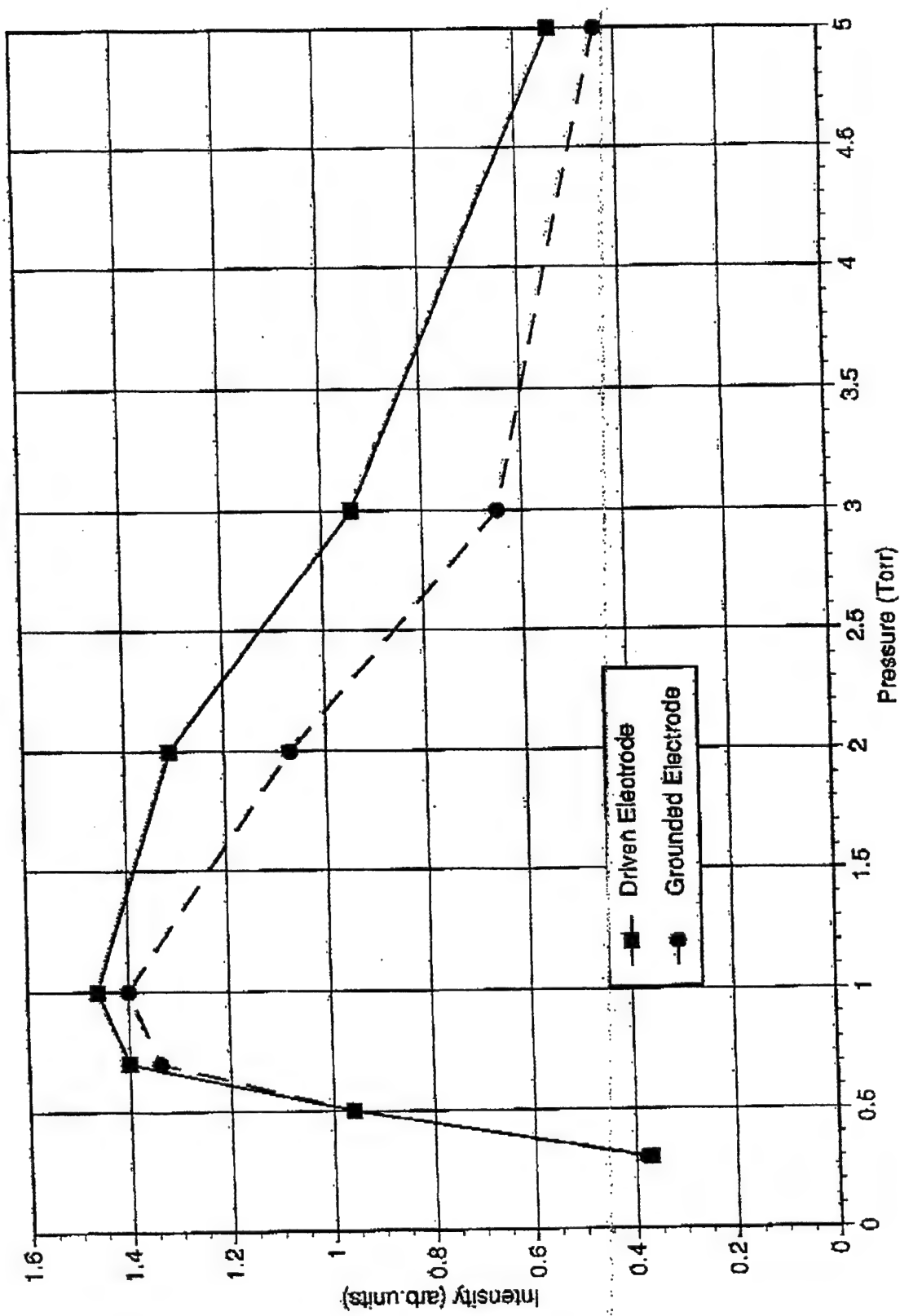


Figure 39. TALIF Signals Observed at Points Near the Driven and Grounded Electrodes

**TALIF Signal at Electrodes vs. Pressure  
Quenching of H atoms by H<sub>2</sub> considered**

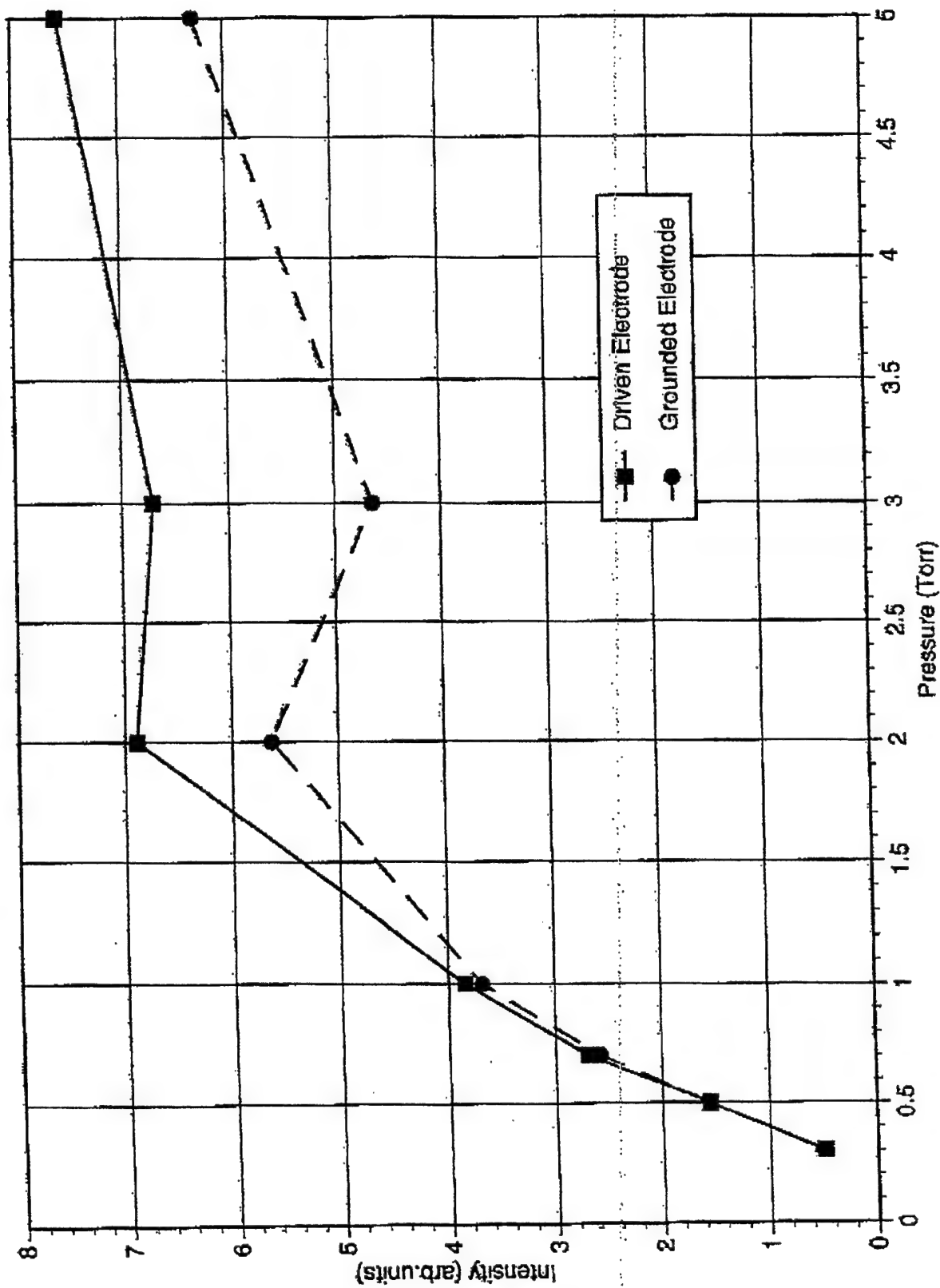


Figure 40. TALIF Signals, Corrected for Quenching, Near the Driven and Grounded Electrodes

calculated as the ratio of one-half (since each H<sub>2</sub> accounts for two H) the corrected maximum H-atom density over the total pressure of H<sub>2</sub> in the reactor. The maximum between 1-3 Torr in the concentration profiles corresponds to slightly less than three percent dissociation of the H<sub>2</sub> gas.

Table 4. H-atom densities as a function of pressure

Pressure (Torr)	Signal (V)	H-atom Density (*10 <sup>15</sup> cm <sup>-3</sup> )	Fluorescence Yield	Corrected H-atom Density (*10 <sup>15</sup> cm <sup>-3</sup> )	Dissociation (%)
0.3	0.7	0.016	0.65	0.02	2.3
0.5	1	0.02	0.54	0.03	2.1
1	1.75	0.039	0.39	0.10	2.8
3	1.6	0.036	0.19	0.18	1.7
5	0.75	0.017	0.13	0.13	0.7

To the eye, the visible emission from the H<sub>2</sub> plasma in the GECRC is asymmetric with a much stronger visible negative glow region after the cathode sheath near the driven electrode. This asymmetry correlates with the variation in TALIF concentration profiles as a function of pressure (Fig. 40). Balmer- $\alpha$  emission from the n=3 level was profiled as a function of H<sub>2</sub> pressure in the reactor at the same RF power level. A 100-micron slit was placed in front of the combination of interference filter and photomultiplier used for the TALIF measurements and the assembly mounted on a computer-controlled stepper motor translation stage. The emission

profiles as a function of position and reactor pressure are shown in Fig. 41.

Figure 41 shows a general asymmetric behavior, sloping down from the driven electrode. The slopes of the profiles are more pronounced in the emission profiles as compared to the TALIF concentration profiles shown earlier. This can be expected since electron-impact dissociative excitation of H<sub>2</sub> which generates excited state H atoms mainly occurs in or near the electrode sheaths where the electrons can gain sufficient energy by acceleration through the sheath potential drop. Given the short radiative lifetime of the n=3 state the electron impact-produced atoms do not diffuse uniformly through the interelectrode gap before they radiate. Ground-state H atoms, on the other hand, do not readily recombine in the gas phase and they diffuse throughout the bulk plasma; generally recombining only on the walls or electrodes. This makes for a more uniform profile of ground-state H atoms as detected by the TALIF diagnostic.

At lower pressures two peaks are seen in the emission profiles near the driven electrode. The one further out into the plasma is due to the contribution from electron impact dissociation discussed above. The peak which is more proximal to the electrode surface is thought to be caused by H<sup>+</sup> and H<sub>2</sub><sup>+</sup> ions colliding with the electrode surface and generating fast H atoms. The fast H atoms are then backscattered and collide with H<sub>2</sub> in the cathode sheath. The collisions have sufficient translational energy to dissociatively excite the H<sub>2</sub> molecules leaving excited state H atoms which emit. Similar observations have been made in the case of low pressure direct current (DC) hydrogen discharges.<sup>83</sup> Electrons should not play a role since electrons leaving the cathode have to cross the cathode sheath region before they generally have sufficient energy to cause this type of process.

As the pressure increases the sheath regions contract and the two peaks observed at lower

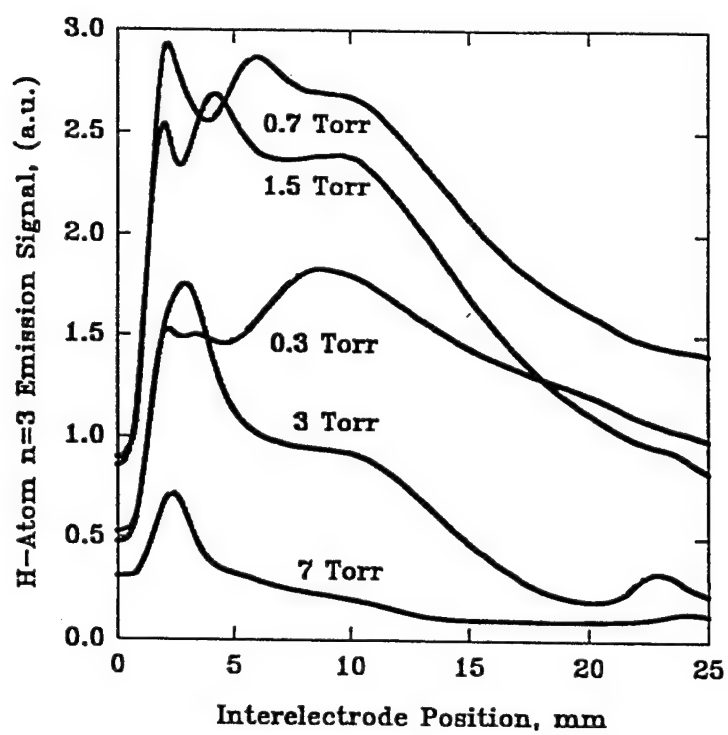


Figure 41. H-Atom Balmer- $\alpha$  Emission Profiles in GEC Reference Cell as a Function of  $H_2$  Pressure

pressures coalesce into one and there appears to be a maximum in the emission profiles near 1 Torr. Again, as in the case of the TALIF concentration profiles, these emission profiles can be corrected for the influence of collisional quenching on the fluorescence quantum yield. Figure 42 is the emission profile from Fig. 41 corrected as a function of pressure for variations in quantum yield.

The asymmetry in emission profiles is very pronounced at the higher pressures. This behavior correlates well with the behavior of the TALIF profiles shown in Figs. 38 and 40. Overall there is increased production of ground-state and excited-state atomic hydrogen nearer the driven electrode for the higher pressure discharges.

Another set of observations which are consistent with both the TALIF and emission profile data are electrical characterization measurements for plasma current and voltage. Figure 43 shows the measured total current through the plasma as a function of pressure. The effects of external impedance were carefully evaluated using an equivalent circuit model of the GEC Reference Cell and deconvoluted from the plasma current data. A maximum in the plasma current is observed at approximately 3 Torr pressure of H<sub>2</sub>. This maximum coincides with the observed maximum in plasma emission and ground-state H-atom concentration as measured by the TALIF diagnostic. This shows a reproducible local maximum in the plasma current about 0.75 Torr which may correlate with a maximum production of fast H atoms near the driven electrode as observed from the plasma emission measurements. However, the mechanism for enhancing electron production and hence the current by electron avalanche multiplication in this region is not readily apparent.

Measurements of the total plasma voltage and plasma DC voltage bias are shown in Fig.

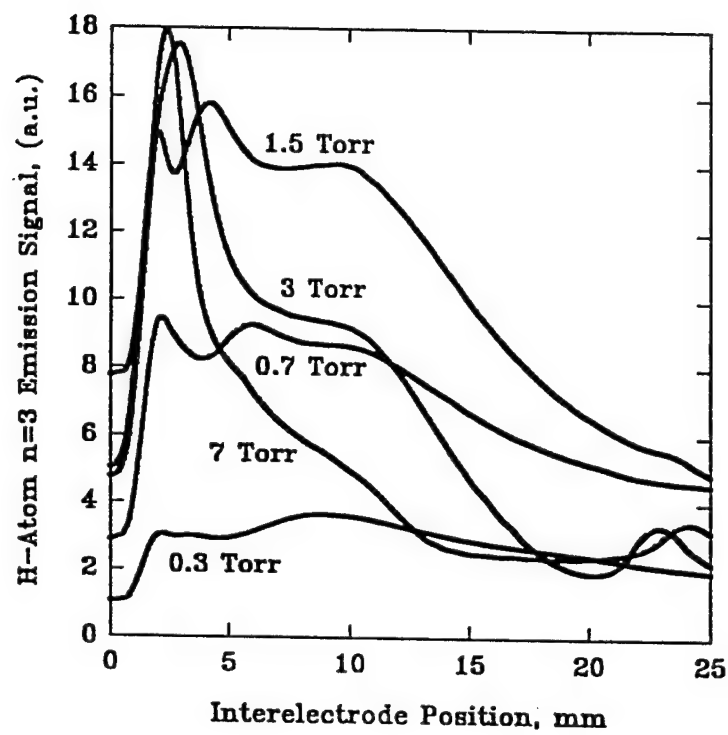


Figure 42. Quenching Corrected H-Atom Balmer- $\alpha$  Emission Profiles

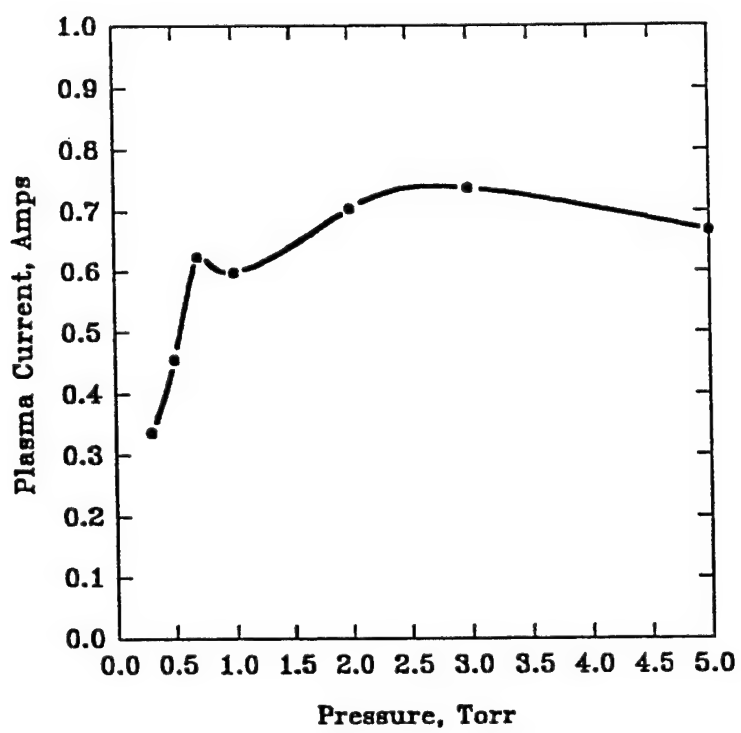


Figure 43. Plasma Current as a Function of H<sub>2</sub> Pressure in GEC Reference Cell.

44. Over a range of several Torr the total voltage drop across the plasma is roughly constant near 600 volts. The plasma DC bias exhibits more variation; ranging from 50 to 200 volts. The large plasma DC bias again demonstrates that the hydrogen plasma is very asymmetric since such a large bias of approximately 20 percent on average would induce the plasma to behave partially in a DC discharge-like manner.<sup>84</sup> The source of the bias and overall asymmetry of the discharge in the GECRC is due to the effect of unequal electrode areas between the top driven electrode and the bottom electrode.<sup>19</sup> The bottom electrode effectively has a larger surface area due to the presence of the grounded guard ring and other reactor surfaces.

An interesting comparison may be made between the pressure dependence of the maximum H-atom density as measured by TALIF and the pressure dependence of the product,  $I \times P$ , plasma current times pressure. The comparison is shown graphically in Fig. 45. For pressures below 1-2 Torr the H-atom density follows the increase of the  $I \times P$  parameter, indicating the production of H atoms is roughly linearly proportional to the product of current and pressure in the lower pressure regime. Above 2 Torr, the H-atom density reaches a maximum and then decreases; diverging from the product of  $I \times P$ . As seen from Fig. 43 the current has also saturated in this pressure region suggesting the source of H atoms due to electron impact dissociation has diminished; possibly due to electron cooling by collision.

#### E. Conclusions

The plasma current and voltage measurements reported here are the first observed for the GEC Reference Cell and an  $H_2$  plasma and in a system which is of industrial scale. At this point the  $H_2$  plasma is in principle the most understandable system that currently exists, measurement of ground state atomic concentrations along with dissociation fraction has determined the

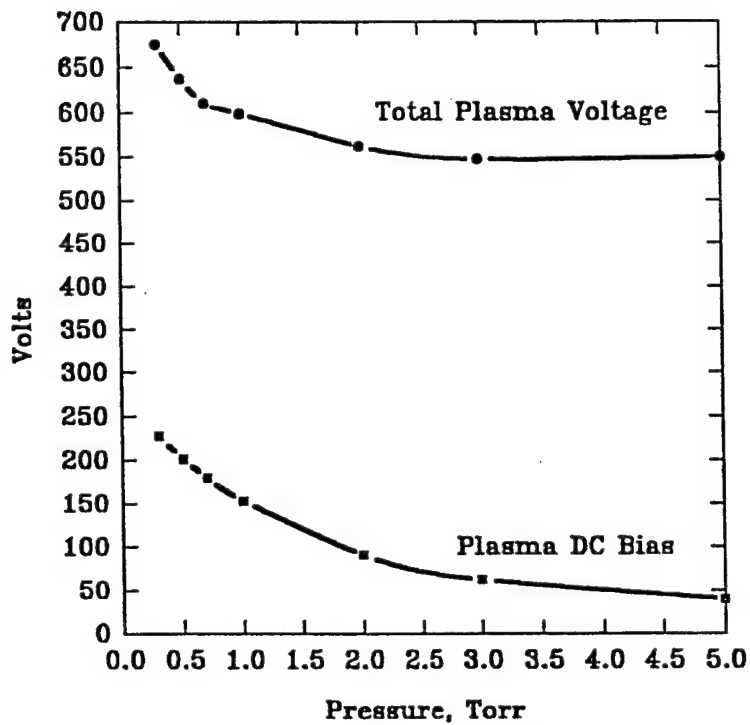


Figure 44. Total Plasma Voltage and DC Bias as a Function of H<sub>2</sub> Pressure in GEC Reference Cell.

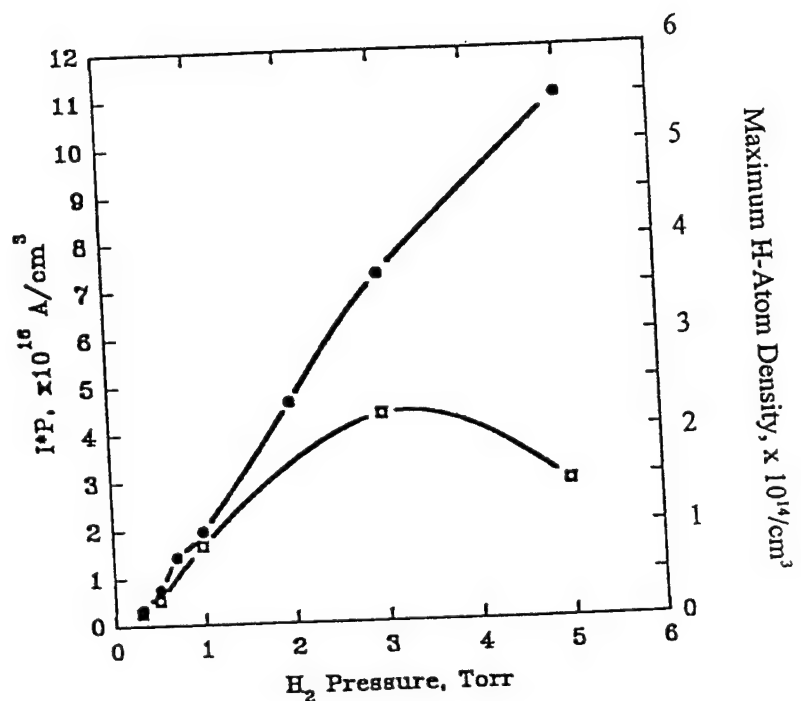


Figure 45. Comparison of Maximum H-Atom Density and the Product of Current and Pressure as a Function of Pressure

majority of the neutral species within the discharge. Practically all important plasma species densities can now be measured or inferred from developed experimental techniques; including electron densities by microwave interferometry, H and H<sub>2</sub> concentrations by TALIF, and detection of H<sup>+</sup> ions by laser photodetachment measurements. The H<sub>2</sub><sup>+</sup> and H<sub>3</sub><sup>+</sup> ion densities and production regimes remain to be investigated. However, given the nearly complete list of measured plasma species as well as other plasma parameters such as current and voltage characteristics it may now be possible to develop a complete and self-consistent model of the simple hydrogen glow discharge.

## 7. TALIF Diagnostics of Nitrogen Atoms

A staple of plasma processing reactors in current use by the semiconductor device community is the RF parallel plate reactor employing N<sub>2</sub> as a feed gas. This reactor has found routine use as a source of nitrogen atoms which actively participate in the plasma-enhanced chemical vapor deposition (PECVD) of silicon nitride (Si<sub>3</sub>N<sub>4</sub>)<sup>85,86</sup>. Its major application is the final encapsulation and passivation layer for the integrated circuit<sup>87,88</sup>. The RF nitrogen source has also been of service in the development of advanced nitride materials<sup>89</sup>. In crystalline form, gallium nitride, boron nitride, aluminum nitride, and indium nitride are all III-V semiconductors with relatively wide band gaps. These materials have been grown epitaxially by plasma methods and, in the future, are expected to fill gaps in electronic device technology with physical and electrical properties not obtainable from silicon based materials.

In order to better the design and operation of the RF parallel plate nitrogen source, a more thorough understanding of the production and behavior of the N-atoms within the reactor needs to be established. In this study we have taken the approach of monitoring the spatially resolved concentration of atomic nitrogen by laser induced fluorescence. As with many light atomic species, including hydrogen and oxygen, the energies of the lowest lying electronic states of atomic nitrogen are too high to be excited by absorption of a single photon from a common laser source. The solution employed in this experiment is the two-photon absorption laser induced fluorescence (TALIF) technique for atomic nitrogen, which results in fluorescence observable in the near infrared.

For this study, the N-atom behavior within a small parallel plate reactor was analyzed. Several milestones were attained toward a complete analysis of the nitrogen plasma system

which are discussed in the following sections. The data depicting the spatial distribution of atomic nitrogen presented an anomaly which was not readily explained with the set of plasma parameters and reactions which were initially applied to the problem. Several theories on the cause of this anomaly have been formulated and, at present, further experiments are being conducted to confirm or disprove these theories.

#### A. Experiment

##### 1. N atom TALIF Schemes

An extremely successful aspect of this study has been the development of the technique for the spatially resolved measurement of ground state atomic nitrogen concentration within the glow discharge region of the RF parallel plate reactor. As seen in the energy level diagram for atomic nitrogen in Fig. 46, the lowest lying state in which two-photon laser absorption is allowed is the  $(3p)^4D^o$  state at  $94882\text{ cm}^{-1}$  above the ground state. When excited to the  $J = 7/2$  level, this corresponds to the absorption of two laser photons with wavelengths of 211 nm. The observed fluorescence results from the radiative transition  $(3p)^4D^o_{7/2} \rightarrow (3s)^4P_{5/2}$  with a wavelength of 868 nm. This is the TALIF scheme that is prevalent in the literature and has been used widely in the analysis of flame combustion<sup>90,91</sup>. The scheme has also been employed to detect atomic nitrogen in the post discharge region of a flowing plasma system<sup>92,93</sup>. In the post discharge region, the TALIF results may then be compared to the traditional N-atom detection method of monitoring the afterglow emission caused by three body N-atom recombination. An atomic nitrogen concentration measurement within the glow discharge region using the TALIF technique, though, has never been reported. The complication that arises in the glow discharge region is that the 868-nm fluorescence is located within a sea of emission lines from the first positive system of

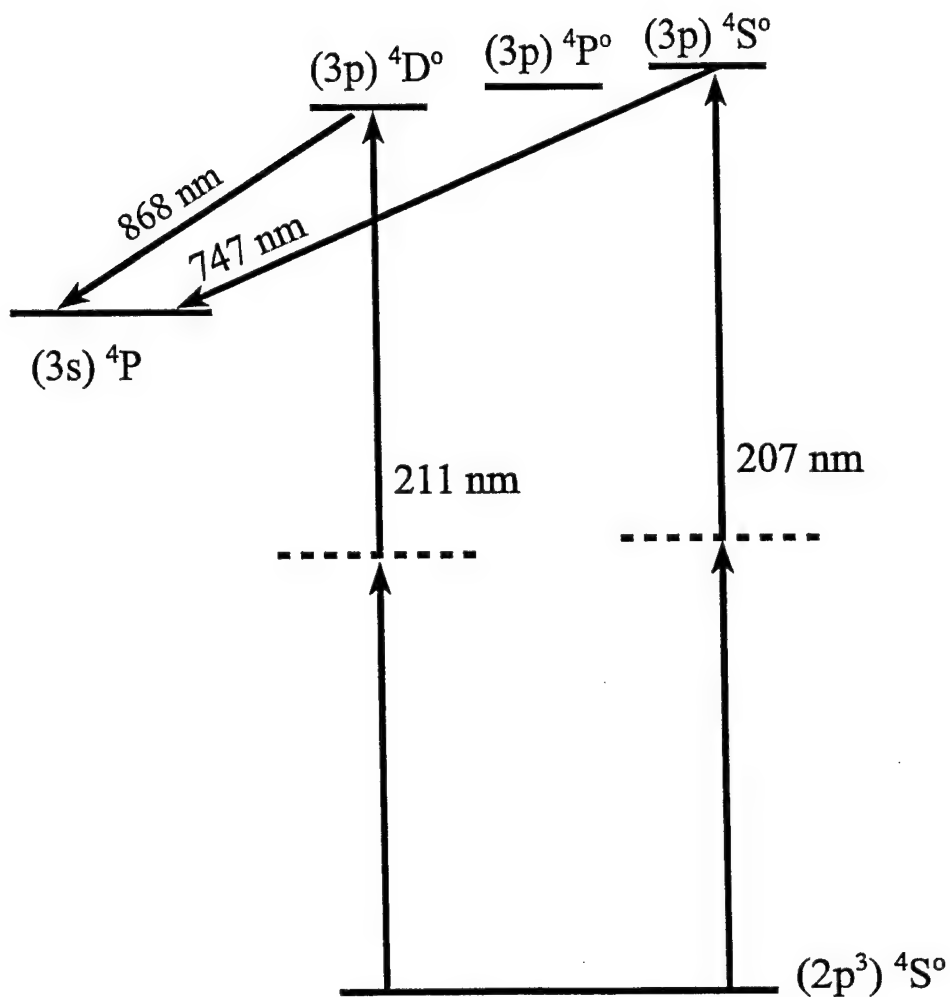


Figure 46. Energy level diagram illustrating TALIF schemes for ground state atomic nitrogen

molecular nitrogen. Specifically, the desired fluorescence directly coincides with emission from the  $B^3\Pi_g$  ( $v'=2$ )  $\rightarrow A^3\Sigma_u^+$  ( $v''=1$ ) bandhead of N<sub>2</sub>. It is a fact that the “narrowband” interference filters, which have been used in most other TALIF experiments, transmit a significant amount of the plasma induced emission leaving the detector saturated in any effort to resolve the weaker fluorescence. In this study, the solution to this problem was to optically image the fluorescence region in the discharge onto the slits of a monochrometer in order to narrow both the bandwidth and the spatial region being collected. A substantial radiance from the plasma induced emission was still reaching the detector, but the TALIF signal from the pulsed laser was comparable in intensity during its fluorescence lifetime. This allowed a time resolved analysis of the TALIF signal to measure the signal strength and subtract any contribution from the continuous plasma induced emission.

Although the TALIF detection through the monochrometer allowed N-atom monitoring directly within the RF discharge, there was still a significant loss of signal-to-noise ratio when compared to detection through a filter with no plasma background. Also the experimental setup was greatly complicated by the additional alignment requirements of the collection optics. This prompted a search for an even higher atomic nitrogen energy level that would allow a two-photon excitation with the resulting fluorescence falling somewhere in a less intense spectral region of the plasma induced emission. Previous TALIF work with atomic hydrogen and oxygen in the RF discharge region found the wavelengths of each fluorescence in a very quiet region of their respective emission spectrum which resulted in simple filter/PMT collection assemblies. As seen in the N-atom energy level diagram, a (3p)<sup>4</sup>P° and a (3p)<sup>4</sup>S° state exist at 95532 cm<sup>-1</sup> and 96750 cm<sup>-1</sup> respectively. These energies correspond to two photon absorption at wavelengths of 209 nm

and 207 nm which represent laser wavelengths that are no more difficult to generate than the 211-nm laser. Fluorescence wavelengths from these TALIF schemes would be ~820 nm for the  $(3p)^4P^o \rightarrow (3s)^4P$  transition and 747 nm for the  $(3p)^4S^o_{3/2} \rightarrow (3s)^4P_{5/2}$  transition. The 820-nm fluorescence falls in an extremely quiet plasma emission region while the 747-nm signal is again in the proximity of an N<sub>2</sub> emission bandhead.

The TALIF scheme involving the  $(3p)^4P^o$  state was therefore approached with great anticipation. A theoretical analysis, though, showed that the two-photon excitation from the  $(2p^3)^4S^o_{3/2}$  ground state to the  $(3p)^4P^o_{5/2,3/2,1/2}$  state is in fact forbidden as our experimental attempt confirmed. A virtual  ${}^4P$  state, at first glance, appeared to be an adequate intermediate state since allowed one photon transitions may occur between this intermediate and both the ground and excited state at hand. Upon further analysis, though, it is clear that an allowed intermediate to excited state transition ( ${}^4P \rightarrow {}^4P^o$ ) only conforms to the  $\Delta L = 0$  single photon selection rule when  $m_l \neq 0$ . When this result is coupled with the fact that the  $(2p^3)^4S^o_{3/2}$  ground state only possesses a  $m_l = 0$  state, a selection rule violation arises. Two-photon transition selection rules dictate that the  $m_l$  values of the ground, excited, and virtual intermediate states must all be equal when absorbing two linearly polarized laser photons. It is clear that all three  $m_l$  values cannot be equal and therefore a virtual state does not exist that will allow a two-photon absorption to the  $(3p)^4P^o_{5/2,3/2,1/2}$  state.

The TALIF scheme involving the upper  $(3p)^4S^o_{3/2}$  state, on the other hand, conforms to all selection rules and has been verified experimentally as a viable detection technique<sup>94</sup>. As with the original TALIF scheme, the fluorescence from this upper state is spectrally coincident with a molecular nitrogen emission bandhead of the first positive system [ $B^3\Pi_g^- (v'=4) \rightarrow A^3\Sigma_u^+ (v''=2)$ ]. Although the goal of finding an N-atom detection scheme with fluorescence in a dark spectral

region of plasma emission was not achieved, the TALIF scheme to the new upper state has several advantages over the original scheme. First, the quantum efficiency of detecting the signal with a near visible wavelength of 747 nm was much improved over the original 868-nm fluorescence. This was a welcome enhancement since the 868-nm fluorescence, when collected through the monochromator, was plagued with a low photon count and it was necessary to average the signal over many laser pulses. Second, the intensity ratio of the 747-nm signal to the background plasma emission reaching the detector through the monochromator was slightly better than for the original TALIF scheme. These two improvements allowed for a significant enhancement in the signal-to-noise ratio in the concentration measurements. Finally, the upper  $(3p)^4S^o_{3/2}$  state of this TALIF scheme was quenched by  $N_2$  to such a small degree over the 0.5 to 3 Torr pressure range of interest, that the effect was barely discernible in a Stern-Volmer type analyses. These advantages made the  $(2p^3)^4S^o_{3/2} \rightarrow (3p)^4S^o_{3/2}$  transition our choice for the TALIF scheme to study the RF parallel plate atomic nitrogen source.

## 2. Absolute Concentration Measurement of Atomic Nitrogen

The intensity of the fluorescence signal from the TALIF technique described above is proportional to density of ground state atomic nitrogen in the laser focus region. An empirical method to determine the absolute concentration associated with the signal intensities is by a controlled introduction of a titrant gas with a known fast reaction with atomic nitrogen. Nitric oxide is the gas of choice to titrate the N-atom signal<sup>95</sup>. The ensuing reaction is



which occurs at a high rate. The calibrated flow of NO needed to titrate away the signal indicates the concentration of N-atoms by a one to one relationship in the above reaction. The titration process is

accomplished with a microwave flowing post discharge attachment to the RF plasma cell as has been previously described for H and O atoms. Although the atomic nitrogen source has changed, the consistent laser source and signal collection geometry allow for an accurate calibration of the TALIF signal to N-atom concentration relationship for the RF plasma cell.

### 3. RF Plasma Source

The RF parallel plate plasma cell used in this study has been described before in this report. It is a scaled down version of a production reactor with top/bottom stainless steel electrodes 5 cm in diameter and an interelectrode gap of 1.9 cm. The bottom electrode is grounded while the top is driven by a power supply at 10 MHz with a power range of 10-50 W. An adjustable matching network is also in-line with the power supply. The plasma cell is mounted on an X-Z translation stage which allows probing of the axial and radial regions of the interelectrode gap to a resolution limited by the laser spot size. The plasma cell is fed with a flow mixture of molecular nitrogen and argon and maintained at a pressure range of 0.5 - 3 Torr.

For temporal analysis of the evolution and decay of the atomic nitrogen concentration, the RF discharge is pulsed at 20 Hz for a duration of 10 - 40 ms. The laser pulse can then be triggered via a delay generator to measure the N-atom density at any time during the pulse discharge cycle.

### 4. TALIF Laser Source and Detection

A block diagram of the experimental apparatus is shown in Fig. 47. The required 207-nm laser radiation to induce the atomic nitrogen TALIF is created with a pulsed laser system which includes a Nd-YAG laser with its second harmonic output pumping DCM dye to produce a 620-nm dye laser output. The 620-nm light is frequency doubled in a KDP crystal to produce 310-nm laser radiation. This 310-nm beam is separated from the 620-nm beam and its polarization

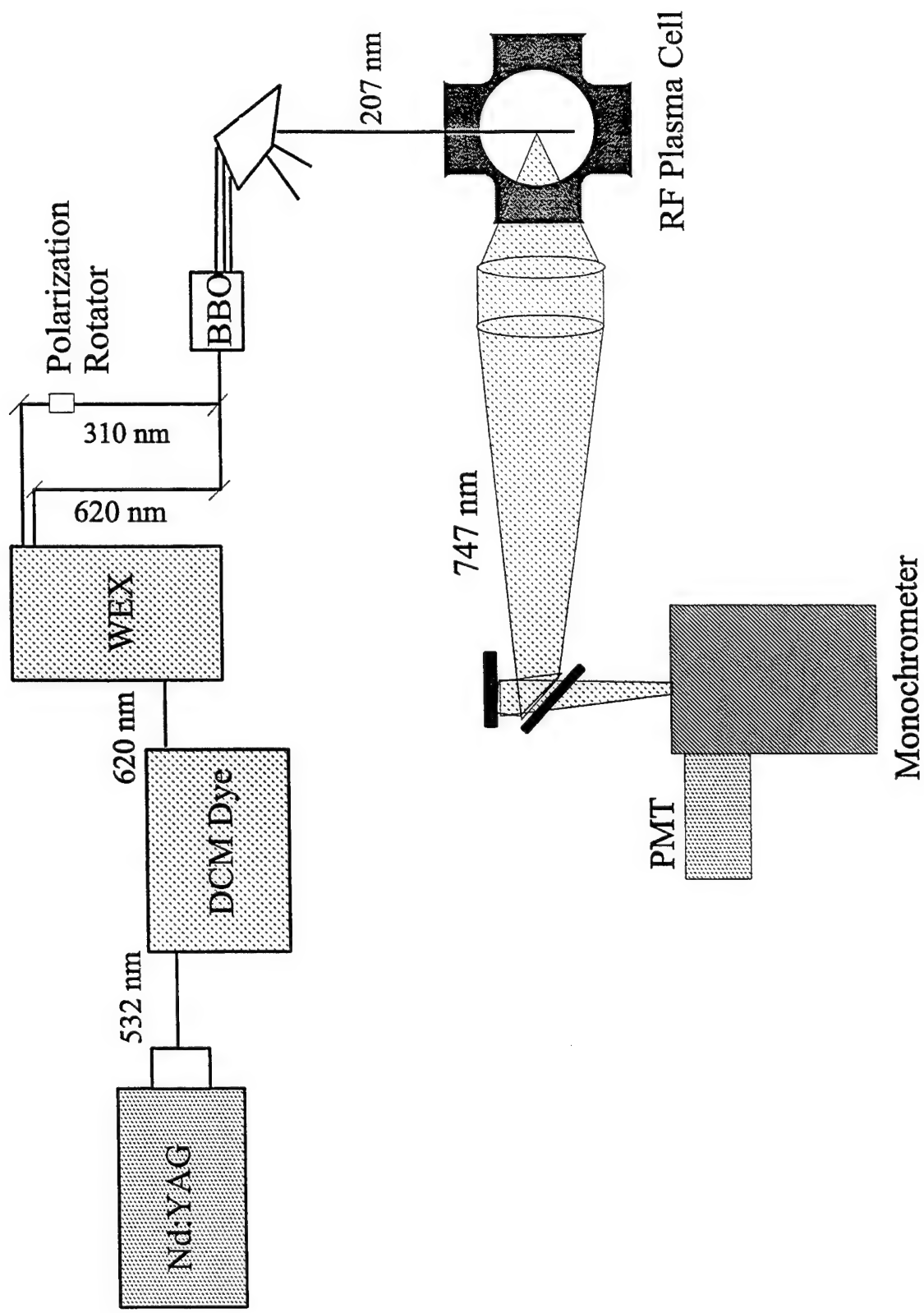


Figure 47. Diagram of N atom TALIF experimental apparatus

rotated to match that of the 620-nm beam. The two beams are then merged again and mixed in a BBO crystal to create the desired beam of wavelength 207 nm. The 207-nm beam is focused into the RF plasma cell with a beam waist of  $\sim$ 100  $\mu$ m. Since the TALIF process only occurs in the high energy density region of the laser focus, spatial discrimination of the measurement is enhanced.

The fluorescence from the cell is collected with a dual 3-inch lens configuration that collimates then focuses the fluorescence onto the slits of a 1-meter monochromometer. The second lens focuses the fluorescence with an f7 cone which passes through a telescoping mirror system. The dual mirrors adjust the height of the image and rotate it by 90° to align with the slits of the monochromometer. An RCA C31034 PMT is at the exit slits of the monochromometer. The signal from the PMT is fed into a 1-GHz Tektronics Digitizing Oscilloscope where it can be averaged over several laser pulses and the integrated signal area corresponding to the intensity can be determined.

## B. Results and Discussion

Atomic nitrogen concentration measurements have been made as a function of position within the interelectrode space. The absolute atomic concentrations, measured to be in the range of  $10^{13}$  to  $10^{14}$  cm<sup>-3</sup>, were consistent with what was expected in this RF power and pressure range. The data presented an anomaly, though, in the spatial distribution of N-atom density that was not anticipated. It seems that along the interelectrode axis of the cell, the atomic density is consistently low in the center of the cell (a dip) and peaked in the sheath regions a few millimeters from the electrodes. The effect, shown in Fig. 48, is most prevalent at pressures above 1 Torr. The dip is seen for most N<sub>2</sub>/Ar gas mixtures except when a very small ratio of

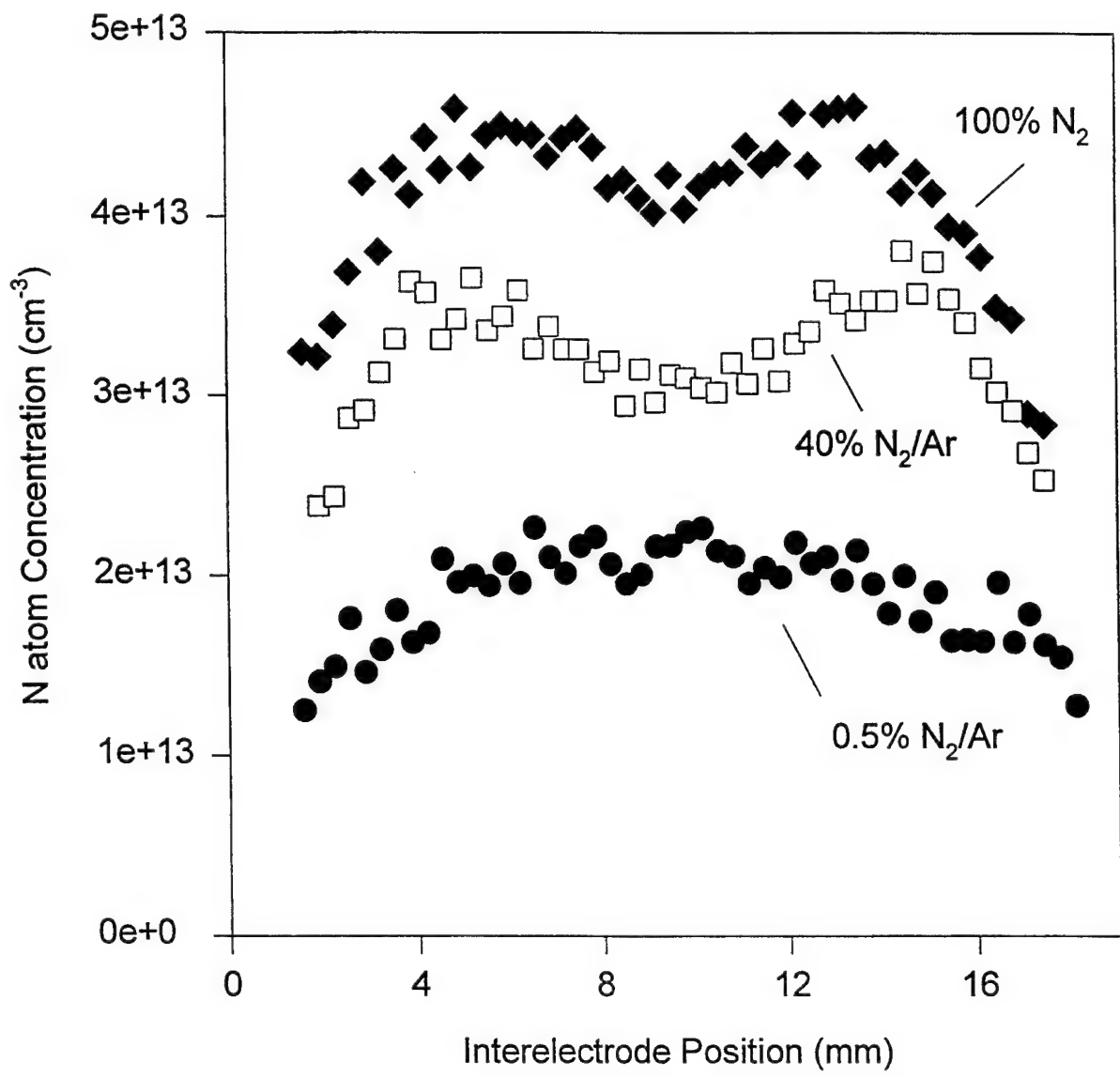


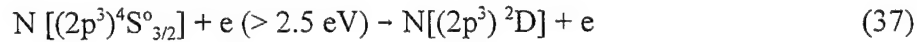
Figure 48. Spatial profile of N atom concentration in 3 Torr RF discharge

nitrogen is diluted in argon. This dip phenomenon was not seen in the atomic density spatial scans of hydrogen and oxygen RF plasmas in previous work. This dip was unexpected since it was thought that the high diffusion rate of N-atoms through N<sub>2</sub> and argon in our low pressure discharge should essentially eliminate any steady-state atomic density gradients, even with localized atomic production in the sheath regions.

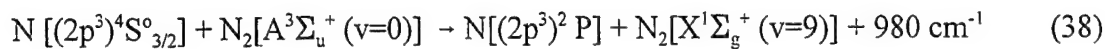
Several experiments were conducted to ensure that this anomaly was not errant data caused by an experimental artifact. An atomic hydrogen spatial scan was repeated with the new collection optics and monochrometer. The data agreed with the previous work and showed no signs of the dip phenomenon. To check whether localized stimulated emission was enhancing the signal in the sheath regions, a spatial scan was executed that monitored the radiative lifetime of the upper state. The lifetime was consistent through the interelectrode space which rejected that possibility. The effects of increased background plasma emission was ruled out as a cause by slightly detuning the laser away from the TALIF resonance and producing a “flat” spatial profile. After careful examination, the dip was accepted as a real N-atom concentration gradient in the RF plasma cell and an effort began to attempt to explain the phenomenon.

For this dip to be present, it must be assumed that the N-atoms are being depleted at a significant rate by some loss mechanism. The magnitude of the effect due to any loss could also be enhanced if the diffusion of atomic nitrogen through the system was not as rapid as predicted. Three theories have been postulated as potential loss mechanisms and each are now being tested. Two of the theories involve the ground state atomic nitrogen being collisionally excited to a metastable state ((2p<sup>3</sup> <sup>2</sup>D or 2p<sup>3</sup> <sup>2</sup>P) and therefore being undetectable with the TALIF probe. If the loss rate by excitation is fast enough compared to diffusion, this would produce the dip

between the sheath production regions. The proposed mechanism for excitation to the  $(2p^3)^2D$  state is by slow electron collision



For the excitation to the  $(2p^3)^2P$  state a collision with a molecular nitrogen metastable is required



The final proposed loss mechanism is that the exhaust flow may be depleting the N-atoms if their diffusion is slower than predicted. For some data the flow rates were at several hundred sccm, but it was calculated that this should not have strongly reduced the residence time of the atomic nitrogen in the plasma cell. An extension to this theory would be if the flow near the electrodes was not laminar and the center region of the cell was much less stagnant than the sheath regions.

All of these theories are being experimentally tested at the present. The excitation loss by the molecular nitrogen metastable has a significant reaction rate<sup>96</sup> and seems to be a promising theory. LIF measurements have also been made on the spatial distribution of the  $N_2[A^3\Sigma_u^+ (v=0,1)]$  state density in the plasma cell to assist in analyzing this mechanism.

The dip anomaly found in the data has induced a considerable effort toward explaining this phenomenon. It has also produced excitement that the TALIF technique may have uncovered a deviation from the expected plasma chemistry of this important plasma processing tool.

## References

1. R. A. Gottscho and T. A. Miller, *Pure and Appl. Chem.* **56**, 189 (1984).
2. G. S. Selwyn, *J. Appl. Phys.* **60**, 2771 (1986).
3. E. H. Collart, J. A. G. Baggerman, R. J. Visser, *J. Appl. Phys.* **70**, 5278 (1991).
4. B. L. Preppernau, D. A. Dolson, R. A. Gottscho, and T. A. Miller, *Plasma Chem. Plasma Process.* **9**, 157 (1989).
5. S. G. Hansen, G. Luckman, G. C. Nieman, and S. D. Colson, *J. Vac. Sci. Technol. B* **8**, 128 (1990).
6. J. W. Thoman, Jr., K. Suzuki, S. H. Kable, and J. I. Steinfeld, *J. Appl. Phys.* **60**, 2775 (1986).
7. G. Hancock, J. P. Sucksmith, and M. J. Toogood, *J. Phys. Chem.* **94**, 3269 (1990).
8. S. G. Hansen, G. Luckman, G. C. Nieman, and S. D. Colson, *J. Appl. Phys.* **68**, 2013 (1990).
9. J. P. Booth, G. Hancock, N. D. Perry, and M. J. Toogood, *J. Appl. Phys.* **66**, 5251 (1989).
10. Y. Hikosaka, H. Toyoda, and H. Sugai, *Jpn. J. Appl. Phys.* **32**, L353 (1993).
11. G. Hancock and M. J. Toogood, *Appl. Phys. Lett.* **60**, 35 (1992).
12. A. D. Tserepi, J. R. Dunlop, B. L. Preppernau, and T. A. Miller, *J. Appl. Phys.* **72**, 2638 (1992).
13. A. D. Tserepi, J. R. Dunlop, B. L. Preppernau, and T. A. Miller, *J. Vac. Sci. Technol. A* **10**, 1188 (1992).
14. J. Bittner, K. Kohse-Hoinghaus, U. Meier, and Th. Just, *Chem. Phys. Lett.* **143**, 571 (1988).
15. B. L. Preppernau, M. Pearce, A. D. Tserepi, E. Wurzberg, and T. A. Miller, *Chem. Phys.*, **196**, 371 (1995).
16. S.G. Hansen, G. Luckman, G.C. Nieman, and S.D. Colson, *Appl. Phys. Lett.* **56** (8), 719 (1990).
17. G. S. Selwyn, *J. Appl. Phys.* **60**(8), 2771 (1986).

18. R.A. Gottscho and M.L. Mandich, *J. Vac. Sci. Technol. A* **3**, 617 (1985).
19. B. N. Chapman, *Glow Discharge Processes*, John Wiley & Sons (1980).
20. A. Hines and R. Maddox, *Mass Transfer, Fundamentals and Applications*, Prentice Hall. NJ, (1985).
21. S. Veprek and V. Marecek, *Solid State Electron* **11**, 683 (1968).
22. R. P. H. Chang and S. Darack, *Appl. Phys. Lett.* **38**, 898 (1981).
23. J. P. Landesman, R. Mabon, G. Allan, M. Lannoo, C. Priester, and J. E. Bonnet, *J. Vac. Sci. Technol. B* **7**, 882 (1989).
24. A. Callegari, P. D. Hoh, D. A. Buchanan, and D. Lacey, *Appl. Phys. Lett.* **54**, 332 (1989).
25. A. Paccagnella, A. Callegari, E. Latta, and M. Gasser, *Appl. Phys. Lett.* **55**, 259 (1989).
26. R. A. Gottscho, B. L. Preppernau, S. J. Pearton, A. B. Emerson, and K. P. Giapis, *J. Appl. Phys.* **68**, 440 (1990).
27. R.A. Gottscho and M.L. Mandich, *J. Vac. Sci. Technol. A* **3**, 617 (1985).
28. S.G. Hansen, G. Luckman, and S.D. Colson, *Appl. Phys. Lett.* **53**, 1588 (1988).
29. V. M. Donnelly, D. L. Flamm, and G. Collins, *J. Vac. Sci. Technol.* **21**, 817 (1982).
30. A. Bouchoule, C. Laure, P. Ranson, Dj Salah, and D. Henry, Proc. 5th Symp. Plasma Processing, (1984).
31. A. Bouchoule and P. Ranson, *J. Vac. Sci. Technol. A* **9**(2), 317 (1991).
32. D. E. Ibbotson, D. L. Flamm, and V. M. Donnelly, *J. Appl. Phys.* **54**, 5974 (1983).
33. H. Wise and B. J. Wood, *Adv. At. Mol. Phys.* **3**, 291 (1967).
34. J. Abrefah and D. R. Olander, *Surf. Sci.* **209**, 291 (1989).
35. B. Ganguly and P. Bletzinger, HA-2, 1993 GEC Conference Abstracts.
36. E. S. Aydil, Z. H. Zhou, K. P. Giapis, Y. J. Chabal, J. A. Gregus, and R. A. Gottscho, (submitted).
37. Z. H. Zhou, E. S. Aydil, R. A. Gottscho, Y. J. Chabal, and R. Reif, (submitted).
38. J. W. Coburn and H. F. Winters, *J. Appl. Phys.* **50**(5), 3169 (1979).

39. J. R. Dunlop, A. D. Tserepi, B. L. Preppernau, T. M. Cerny, and T. A. Miller, *Plasma Chem. Plasma Proc.* **12**, 1 (1992).

40. R. L. Bersin, *Solid State Technol.* **13**, 39 (1970).

41. C. J. Mogab, A. C. Adams, and D. L. Flamm, *J. Appl. Phys.* **49**, 3796 (1978).

42. R. d'Agostino, F. Cramarossa, S. de Benedictis, and G. Ferraro, *J. Appl. Phys.* **52**, 1259 (1981).

43. W. R. Harshbarger, T. A. Miller, P. Norton, and R. A. Porter, *Appl. Spectrosc.* **31**, 201 (1977).

44. J. P. Booth, O. Joubert, J. Pelletier, and N. Sadeghi, *J. Appl. Phys.* **69**, 618 (1991).

45. J. P. Booth and N. Sadeghi, *J. Appl. Phys.* **70**, 611 (1991).

46. G. Selwyn, *J. Appl. Phys.* **60**, 2771 (1986).

47. R. E. Wallcup, K. L. Senger, and G. S. Selwyn, *J. Chem. Phys.* **84**, 2688 (1986).

48. E. J. H. Collart, J. A. G. Baggerman, and R. J. Visser, *J. Appl. Phys.* **70**, 5278 (1991).

49. G. Hancock and M. Toogood, *Appl. Phys. Lett.* **60**, 35 (1992).

50. A. D. Tserepi, J. R. Dunlop, B. L. Preppernau, and T. A. Miller, *J. Appl. Phys.* **72**, 2638 (1992).

51. J. Bittner, K. Kohse-Hoinghaus, U. Meijer, and Th. Just, *Chem. Phys. Lett.* **143**, 571 (1988).

52. A. D. Tserepi and T. A. Miller, *J. Appl. Phys.* **75**, 7231 (1994).

53. J. E. Morgan and H. I. Schiff, *Canadian Journal of Chem.* **42**, 2300 (1964).

54. A. Mathias and H. I. Schiff, *Faraday Discuss. Chem. Soc.* **37**, 39 (1964).

55. K. Smith, R. J. Henry, and P. G. Burke, *Phys. Rev.* **157**(1), 51 (1967).

56. M. Alden, U. Westblom, and J.E.M. Goldsmith, *Opt. Lett.* **14**, 305 (1989).

57. M. Alden, P.E. Bengtsson, and U. Westblom, *Opt. Commun.* **71**, 263 (1989).

58. J. E. M. Goldsmith, *J. Opt. Soc. Am. B* **6**, 1979 (1989).

59. R. P. Saxon and J. Eichler, *Phys. Rev. A* **34**, 199 (1986).
60. J. E. M. Goldsmith, *J. Chem. Phys.* **78**, 1610 (1983).
61. Y. -L. Huang and R. J. Gordon, *J. Chem. Phys.* **97**, 6363 (1992).
62. M. A. A. Clyne and W. S. Nip, *Reactive Intermediates in the Gas Phase* (Academic, New York, 1979).
63. G. I. Peters and L. Allen, *J. Phys. A* **4**, 238 (1971).
64. A.E. Siegman, *Lasers* (University Books, Mill Valley, California).
65. E. Wurzberg, A.D. Tserepi, and T.A. Miller (in preparation).
66. J. Amorim, G. Bavarian, J. Jolly, M. Touzeau, *J. Appl. Phys.* **76**, 1487 (1994).
67. B. Ganguly, J. Shoemaker, B. Preppernau, and A. Garscadden, *J. Appl. Phys.* **61**, 2778, (1987).
68. B. Smith, J. Womack, N. Omenetto, and J. Winefordner, *Appl. Spect.* **43**, 873, (1989).
69. A. Mitchell and M. Zemansky, *Resonance Radiation and Excited Atoms*, Cambridge University Press, New York, (1961).
70. A. Catherinot, B. Dubreuil, and M. Gand, *Phys. Rev. A* **18**, 1097, (1978).
71. D. Baldwin, M. Buntine, and D. Chandler, *J. Chem. Phys.* **93**, 6578, (1990).
72. J. Tung, A. Tang, G. Salamo, and F. Chan, *J. Opt. Soc. Amer. B* **3**, 837, (1986).
73. W. Press, B. Flannery, S. Teukolsky, and W. Vetterling, *Numerical Recipes: The Art of Scientific Computing*, Cambridge University Press, New York (1986).
74. N. Terazana, M. Ukai, N. Kouchi, K. Kameta, Y. Hatano, and K. Tanuka, *J. Chem. Phys.* **99**, 1637 (1993).
75. Y. Hatano, private communication.
76. M.E. Riley and M. K. Matzen, *J. Chem. Phys.* **83**, 4787 (1975).
77. Program and Abstracts. 41st Annual Gaseous Electronics Conference, 18-21 October, 1988, Minneapolis, Minnesota.
78. G.E.C. RF Reference Cell Newsletter, ed. J.R. Roberts, **3** (1) April 1991.

79. Program and Abstracts, 42st Annual Gaseous Electronics Conference, 17-20 October, 1989, Palo Alto, California.

80. Abstracts E-25 and E-26, Program and Abstracts, 43st Annual Gaseous Electronics Conference, 16-19 October, 1990, Champaign-Urbana, Illinois.

81. P. Loewenhardt, B. Blackwell, R. Boswell, G. Conway, and S. Hamberger, *Phy. Rev. Lett.* **67** (20), 2792, 1991.

82. Reactive Gas Phase Intermediates: Generation and Monitoring, Ed. D. Setser, (Academic Press, New York, 1979).

83. P. Petrovic, B. Jelenkovic, and A. Phelps, *Phys. Rev. Lett.* **68** (3), 325, 1992.

84. A. Von Engel, Electric Plasmas: Their Nature and Uses, (Taylor and Francis Limited, New York, 1983).

85. S. M. Rossnagel, J. J. Cuomo, and W. D. Westwood, *Handbook of Plasma Processing Technology* (Noyes, Park Ridge N.J., 1990).

86. R. S. Rosler, W. C. Benzing, and J. Baldo, *Solid State Technol.* **19**, 45 (1976).

87. National Research Council, Plasma Science Committee, *Plasma Processing of Materials: Scientific Opportunities and Technical Challenges* (National Academy Press, Washington, D.C., 1991).

88. A. Sherman, *Chemical Vapor Deposition for Microelectronics* (Noyes, Park Ridge N.J., 1987).

89. S. Dzioba, *Mat. Res. Soc. Symp. Proc.* **165**, 91 (1990).

90. U. Westblom, S. Agrup, M. Alden, and P. Cederbalk, *Appl. Opt.* **30**, 2990 (1991).

91. S. Agrup, U. Westblom, and M. Alden, *Chem Phys. Lett.* **170**, 406 (1990).

92. W. K. Bischel, B. E. Perry, and D. R. Crosley, *Appl. Opt.*, **21**, 1419 (1982).

93. W. K. Bischel, B. E. Perry, and D. R. Crosley, *Chem. Phys. Lett.*, **82**, 85 (1981).

94. G. J. Bengtsson, J. Larsson, S. Svanberg, and D. D. Wang, *Phys. Rev. A* **45**, 2712 (1992).

95. G. B. Kistiakowsky, and G. G. Volpi, *J. Chem. Phys.* **27**, 1141 (1957).

96. L. G. Piper, *J. Chem. Phys.* **90**, 7087 (1989).

## Bibliography

### Publications

1. "Two-photon Absorption Laser-induced Fluorescence of H Atoms: A Probe for Heterogeneous Processes in Hydrogen Plasmas," A.D. Tserepi, and T.A. Miller, *J. App. Phys.*, **75**, 7231 (1994).
2. "Spatially and Temporally Resolved Absolute O-atom Concentrations in Etching Plasmas," A.D. Tserepi and T.A. Miller, *J. App. Phys.*, **77**, 505 (1995).
3. "Angular Momentum State Mixing and Quenching of n=3 Atomic Hydrogen Fluorescence," B.L. Preppernau, K. Pearce, A. Tserepi, E. Wurzberg, and T.A. Miller, *Chem. Phys.*, **196**, 371 (1995).
4. "Two-photon-excited Stimulated Emission from Atomic Oxygen in RF Plasmas: Detection and Estimation of its Threshold," A. D. Tserepi, E. Wurzberg, and T. A. Miller, *Chem Phys. Lett.*, submitted.

### Presentations

1. "Measurement of Atomic Hydrogen Concentration Profile in GEC Reference Cell," B.L. Preppernau, and T.A. Miller, 45th Annual Gaseous Electronics Conference, Boston, MA, October 27-30, 1992.
2. "Spatially and Temporally Resolved Detection of H Atoms in RF Plasmas," A.D. Tserepi, and T.A. Miller, 45th Annual Gaseous Electronics Conference, Boston, MA, October 27-30, 1992.
3. "Spatially and Temporally Resolved Profiles of O Atoms in Etching Plasmas," A.D. Tserepi, and T.A. Miller, 45th Annual Gaseous Electronics Conference, Boston, MA, October 27-30, 1992.
4. "Two-Photon Laser Induced Fluorescence Diagnostics of Plasma," T. A. Miller, 6th International Symposium on Laser-Aided Plasma Diagnostics, Bar Harbor, Maine, October 25-29, 1993.
5. "Laser Diagnostics of Materials Processing Plasmas," T. A. Miller, Sandia Laboratories, Albuquerque NM, January 20, 1994.
6. "Diagnostics of Diamond Deposition Environments," T. A. Miller, CVD Diamond Synthesis, Gordon Conference, Plymouth NH, June 19-24, 1994.

7. "Optical Diagnostics for Plasma Processors," T. A. Miller, Optical Society of America, Portland OR, September 11-15, 1995.

Theses

1. "Laser Diagnostics for Bulk and Near-surface Detection of Atomic Hydrogen and Oxygen in Plasma Environments," A. Tserepi, The Ohio State University, 1994.
2. "Laser Diagnostics of Atomic Hydrogen and Oxygen Production in RF and Microwave Plasma Discharges," Bryan Preppernau, The Ohio State University, 1993.